MODELING AND OPTIMIZATION OF CAPACITIVE MICROMACHINED ULTRASONIC TRANSDUCERS

A Dissertation
Presented to
The Academic Faculty

By

Sarp Satir

In Partial Fulfillment
of the Requirements for the Degree
Doctor of Philosophy
in
Electrical and Computer Engineering

School of Electrical and Computer Engineering
Georgia Institute of Technology
December 2014

MODELING AND OPTIMIZATION OF CAPACITIVE MICROMACHINED ULTRASONIC TRANSDUCERS

Approved by:

Dr. F. Levent Degertekin, Advisor
Professor, School of ECE
Georgia Institute of Technology

Dr. Maysam Ghovanloo
Associate Professor, School of ECE
Georgia Institute of Technology

Dr. Oliver Brand
Professor, School of ECE
Georgia Institute of Technology

Dr. Pamela T. Bhatti
Associate Professor, School of ECE
Georgia Institute of Technology

Dr. Karim Sabra
Associate Professor, School of Mechanical Engineering
Georgia Institute of Technology

Date Approved: November 12, 2014

Dedicated to my family, Hayriye, Irfan and Mert

ACKNOWLEDGMENTS

First and foremost, I would like to thank my advisor Dr. Levent Degertekin for his consistent support, guidance, and for giving me the freedom to explore different approaches to solving the problems under consideration. His positive attitude and open door policy made the research environment significantly pleasant and exciting.

I would also like to thank my committee members Dr. Karim Sabra, Dr. Oliver Brand, Dr. Maysam Ghovanloo and Dr. Pamela T. Bhatti for taking the time and effort to serve on my defense committee.

This work was made possible through the financial support of the National Institute of Biomedical Imaging and Bioengineering.

This dissertation is the result of collaborative team work of former and present members of Dr. Degertekin's group and would not have otherwise been possible. I am thankful to Dr. Jaime Zahorian, Toby Xu and Michael Hochman for the long hours they spent in the clean room to fabricate the devices used for the experimental results presented in this work, Dr. Coskun Tekes and Dr. Gokce Gurun for their valuable comments and the discussions we had and Evren Arkan for preparing samples for experiments.

I would like to thank Dr. Mustafa Unel, my senior year research advisor during my undergraduate studies for encouraging me to attend graduate school and pursue a career in research.

Last but not least, I would like to express my gratitude to Carmen Salazar for her support, help and understanding during the final writing phase of this dissertation.

TABLE OF CONTENTS

LIST OF TABLES

LIST OF FIGURES

SUMMARY

Capacitive Micromachined Ultrasonic Transducers (CMUTs) are membrane based transducers that utilize electrostatic actuation to transmit ultrasound signals and perform capacitive sensing for the reception of incident ultrasound waves. CMUTs offer distinct advantages over piezoelectric transducers that currently dominate the ultrasound market. Cost reduction from batch microfabrication, improved image resolution, and the ability to manufacture high frequency arrays with small footprint elements, and integration with CMOS electronics make CMUTs an attractive alternative to piezoelectric transducers. However, CMUTs are nonlinear devices because of their electrostatic actuation mechanism and suffer from low overall SNR when compared to their piezoelectric counterparts. Therefore, CMUT arrays must be optimized to operate close to physical limits requiring large signal operation to be competitive in terms of SNR and linearity. The nonlinear device behavior makes modeling, design, and optimization of the CMUT arrays challenging for large signal operation.

The objective of this research is to develop large signal modeling and optimization methods for CMUTs, especially when they are used in an array configuration. General modeling and optimization methods that cover a large domain of CMUT designs are crucial, as many membrane and array geometry combinations are possible using existing microfabrication technologies. Currently, large signal modeling methods for CMUTs are not well established and nonlinear imaging techniques utilizing linear piezoelectric transducers are not applicable to CMUTs because of their strong nonlinearity. In this work, the nonlinear CMUT behavior is studied, and a feedback linearization method is proposed to reduce the CMUT nonlinearity. This method is shown to improve the CMUT performance for continuous wave applications, such as high-intensity focused ultrasound or harmonic imaging, where transducer linearity is crucial. In the second part of this dissertation, a large signal model is developed that is capable of transient modeling of CMUT arrays with

arbitrary electrical terminations. The developed model is suitable for iterative design optimization of CMUTs and CMUT based imaging systems with arbitrary membrane and array geometries for a variety of applications. Finally, a novel phase-modulation method for nonlinear tissue and contrast agent imaging with CMUTs is presented. It is shown that the nonlinear content can be successfully extracted from echo signals in a CMUT based imaging system using a multiple phase modulated pulse scheme. The proposed method is independent of the CMUT geometry and valid for large signal operation. Experimental results verifying the developed large signal CMUT array model, proposed gap feedback and phase modulation techniques are also presented.

CHAPTER 1

INTRODUCTION AND BACKGROUND

As of today, ultrasonic transduction is an enabling technology for many fields, including navigation and ranging (sonar), medical imaging and therapy, acoustic microscopy, non-destructive evaluation of materials and structures, robotic sensing, ocean acoustics, and geophysics. Especially in medicine, ultrasonography offers a cheap, portable, non-ionizing and minimally invasive alternative to radiographic imaging (X-rays), magnetic resonance imaging (MRI) and nuclear medicine imaging systems. Diagnostic ultrasound imaging systems utilize ultrasound waves to visualize internal body structures and transducer technology is the foundation of such systems. An ultrasonic transducer, the electromechanical device that converts electrical energy to ultrasound waves or vice versa, is the heart of an ultrasound system. The developments in ultrasonic transduction technology have led to many novel ultrasound modalities and in return, these methods have challenged the limits of transducer technology, to drive the next generation of ultrasonic transducer research.

In this chapter, first a brief introduction to ultrasonic imaging is given with examples. Based on the principles of ultrasonic imaging, the performance requirements of the ideal transducer is discussed, to illustrate the demanding engineering challenges associated with ultrasonic imaging system design. Second, a brief overview of ultrasonic transducers based on piezoelectric phenomenon is given to highlight the shortcomings of the current state of the art transduction technology. Finally, an introduction to capacitive micromachined ultrasonic transducers (CMUTs) is presented to cover the background research, upon which the contributions in this dissertation is built upon.

1.1 Ultrasonic Imaging

The diagram given in Figure 1 summarizes an basic principles of ultrasound imaging, given in the context of medical ultrasonography. Figure 1(a) presents the imaging scenario where

a single ultrasonic transducer is imaging a patient immersed in water. The resulting amplitude mode (A-mode) image is given in Figure 1(b), where the envelope of the received echo signal is plotted versus time.

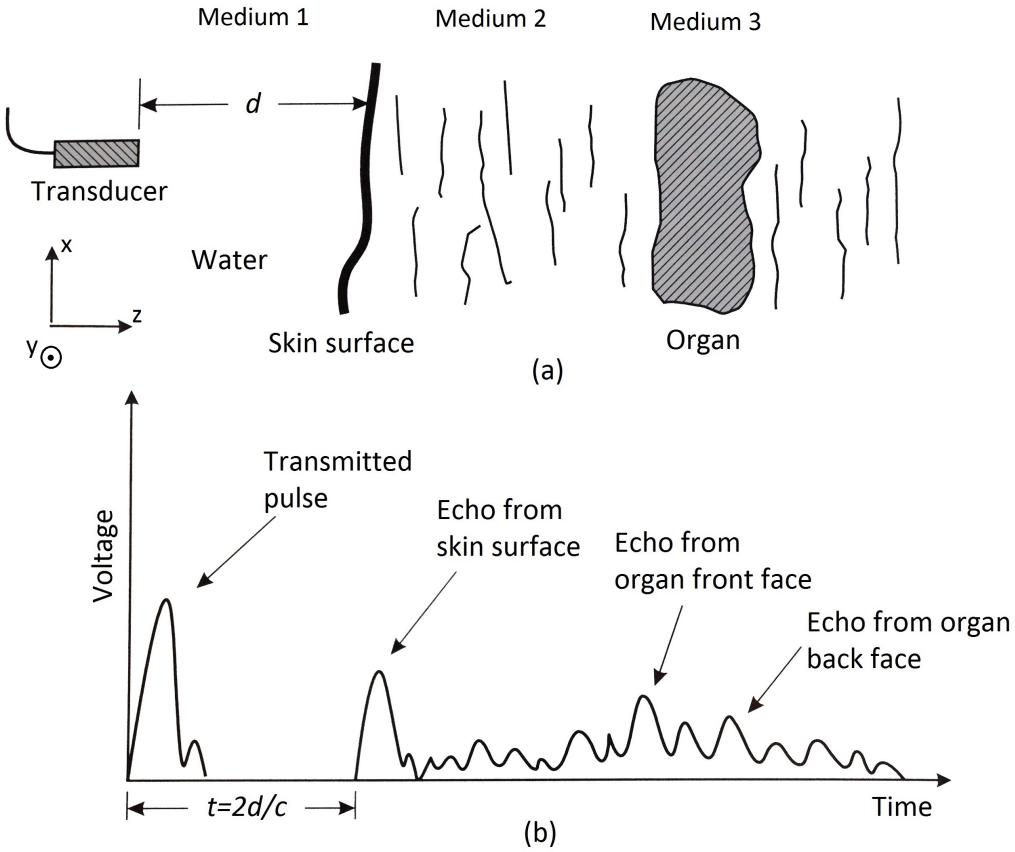

Figure 1: A-mode imaging [1]

In the diagram above, the distance between the patient's skin and the transducer is d and the speed of sound in water is c. At $t = 0$, an ultrasound pulse is transmitted by the transducer and the transmitted waveform arrives at the skin surface at $t = d/c$. Because of the discontinuity of material properties at the skin-water interface, some of the sound energy reflects back and the remaining energy gets transmitted into the body, neglecting thermal losses at the boundary. The reflected and transmitted wave amplitudes are functions of the density and sound speed of the media separated by the water-skin interface. For a

propagating plane wave the amplitude reflection and transmission coefficients are [17]

$$R = \frac{\rho_2 c_2 - \rho_1 c_1}{\rho_2 c_2 + \rho_1 c_1}, \; T = 1 + R. \tag{1}$$

where $\rho_n c_n$ is the acoustic impedance of medium n. The reflected signal arrives back at the transducer at $t = 2d/c$ and it is converted to electrical signal by the transducer and recorded by the imaging system. As time progresses, the ultrasound wave transmitted into the body propagates and reflects back towards the transducer where it hits a material boundary, such as the tissue-organ interface. By collecting all the echoes within a time frame, the A-mode image of the complete field-of-view is constructed as shown in 1(b).

In practice, the A-mode image is affected by noise in the imaging system. The signal-to-noise ratio (SNR) of the ultrasound image therefore is strictly dependent on the amplitude of the received echo signals. The speed of sound and reflection coefficients for various kinds of tissue relative to blood are shown in Figure 2. As seen in the figure, the reflected signal amplitudes can be 50 dB below the transmitted signal amplitude. In the presence of noise, efficient conversion of the reflected sound waves to electrical signals is therefore crucial. Also, since the reflected signal amplitudes are proportional to the transmitted signal amplitude, the transmit signal amplitude determines the SNR. Moreover, a practical imaging system has limited electrical output power to drive the transmit cycle. Therefore an ideal transducer must have optimal transmit sensitivity to be able to generate the maximum ultrasound signal amplitude with minimal electric drive signal power and optimal receive sensitivity to generate maximal electrical output signal power for the received ultrasound echo signals.

The quality of the images generated by an ultrasonic imaging system is strictly limited by the transducer performance. Axial resolution is one of the image quality parameters that determines the minimum distance between two features that can be distinguished in the image. For example in the A-mode imaging example given in Figure 1, the axial resolution of the imaging system is directly related to the length of the transmitted pulse. If the thickness of the organ in the example in Figure 1 is smaller than the pulse-length, then

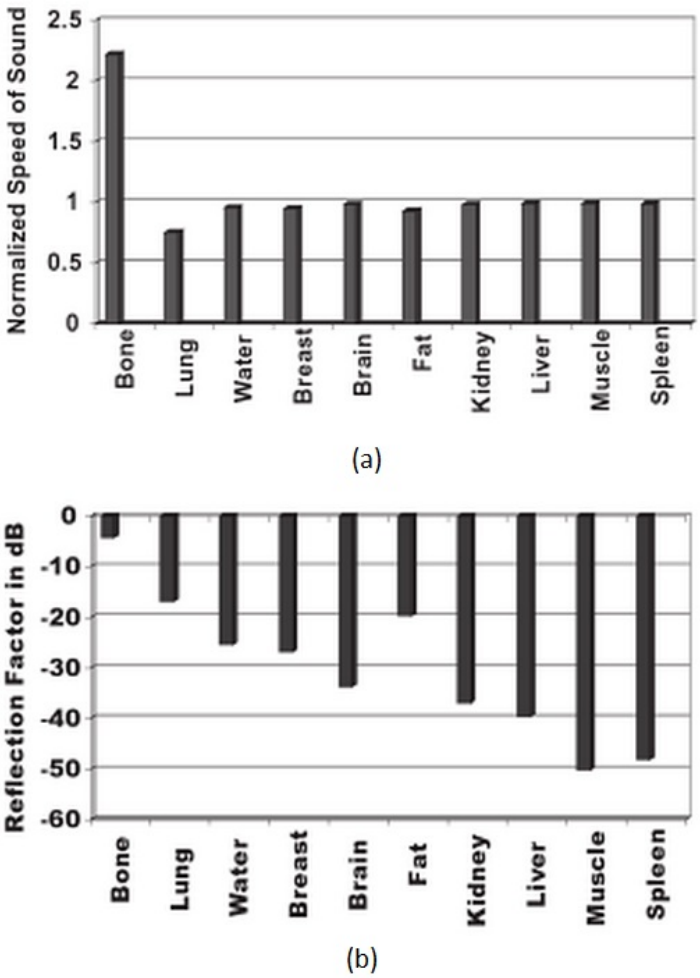

Figure 2: (a) The sound speed in various tissues normalized to the speed of sound in blood (b) The amplitude reflection coefficient for various tissues relative to blood [2]

the front and back faces of the organ cannot be distinguished in the constructed A-mode image. Therefore shorter transmitted pulse length results in better axial resolution for an imaging system. However the shortest pulse a transducer can transmit is limited by its impulse response, hence its operation bandwidth. An ideal transducer would have an infinite bandwidth so it can transmit ideal impulses, resulting in ideal axial resolution. However in practice, transducer bandwidth is limited and broadest bandwidth possible is desired for improved imaging performance. Usually the bandwidth of an ultrasonic transducer is normalized to its center frequency, f_0 and expressed in terms of its fractional bandwidth, FBW = f_0/bandwidth.

The A-mode imaging system presented in Figure 1 constructs an ultrasound image of the region where the transmitted beam illuminates. The width of the transmitted beam determines the lateral resolution of the imaging system. The lateral resolution is another image quality parameter which defines the minimum distance the imaging system can resolve between two features in the image which are separated perpendicularly to the imaging axis (x axis in Figure 1). The beam-width is determined by diffraction of the transmitted ultrasound wave, therefore is a function of the transducer geometry such as transducer size and curvature.

If the A-mode imaging procedure is repeated as the the transducer is translated in x axis, the resulting A-mode images can be concatenated to construct a two-dimensional brightness mode (B-mode) image. In this case the A-mode images are converted to gray scale images, where higher amplitude correspond to white, and lower amplitudes correspond to black in the two-dimensional B-mode image. By additional translation of the transducer in the y axis, a three-dimensional B-mode image can be constructed. As an alternative to the translating transducer system, an ultrasound imaging system utilizing an array of transducers that are fixed in space can be utilized to construct B-mode images. In this case, each transducer consecutively constructs an A-mode image of its own field-of-view and the A-mode images are concatenated to construct the final B-mode image. An example B-mode ultrasound imaging system for side-looking intravascular imaging is presented in the schematic in Figure 3.

The imaging system presented in Figure 3 is based on a circular transducer mechanically rotated inside the artery to construct cross-sectional images of the arterial wall. The transducer generates an A-mode image, rotates perpendicular to its imaging axis, generates another A-mode image and the process continues until 360° rotation is completed. Then the collected A-mode images are concatenated to generate the final B-mode image frame, representing the cross-sectional ultrasound image of the artery. Alternatively, a multi-transducer array can be utilized to construct the B-mode image. In this case, array

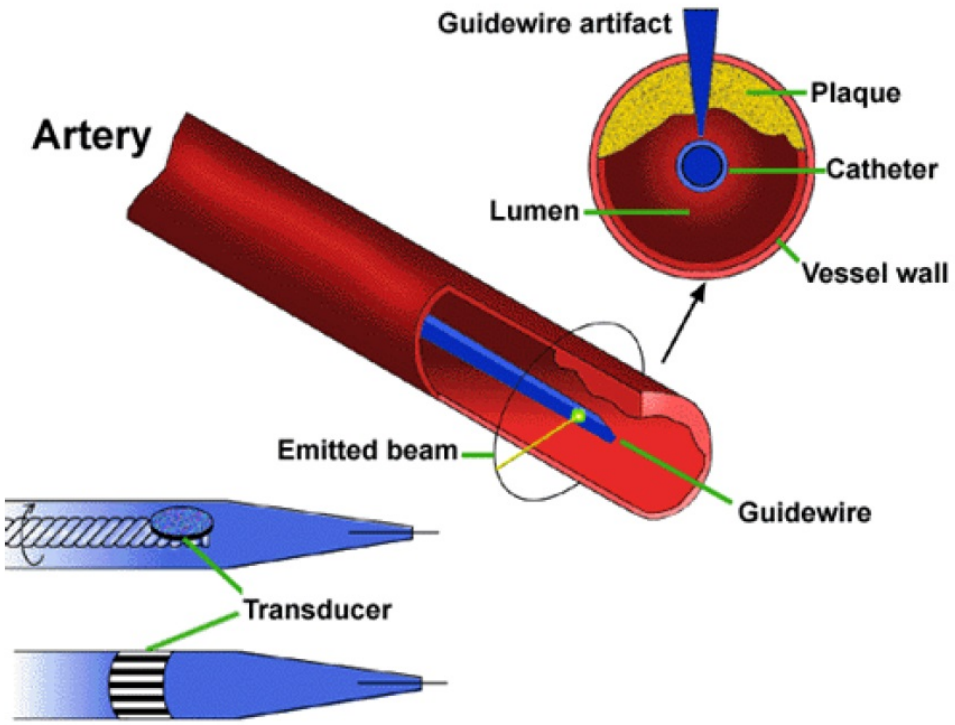

Figure 3: Example B-mode imaging system: Schematic of an IVUS catheter within an artery, and single- and multi-element transducer types [3]

elements collect their own respective A-mode images and the B-mode image is constructed by concatenation of the individual A-mode images. An example cross-sectional B-mode image of a coronary artery on the arterial wall is shown in Figure 4 [4].

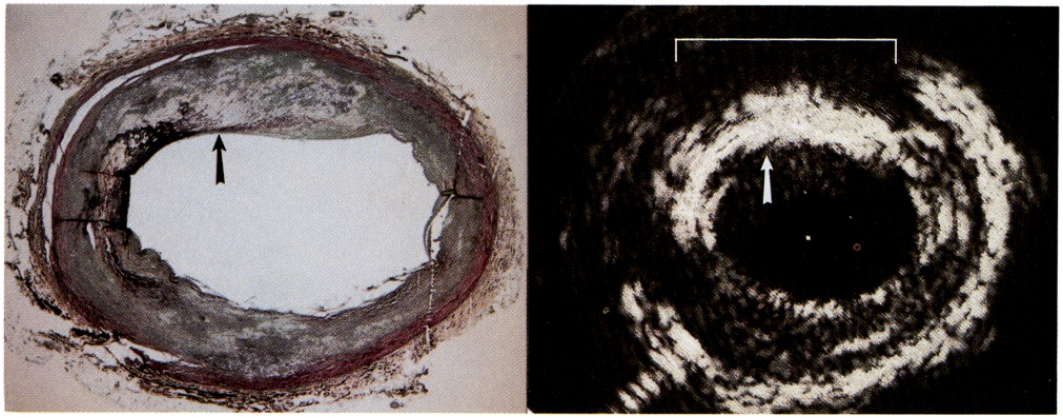

Figure 4: Photograph and B-mode ultrasound image from a coronary artery showing a calcified plaque, pointed by the arrow [4]

Higher difference in the acoustic impedances of the interfacing media results in reflection of most of the acoustic energy at the boundary according to Equation (1). Therefore ultrasonography, by principle, suffers from difficulties in imaging structures behind acoustically hard and soft structures such as bone and air as a drawback. This is indeed visible in the cross-sectional coronary artery image shown in Figure 4 where the region behind the calcified plaque is completely shadowed by the plague since the plague acts like a hard reflector due to its high acoustic impedance.

1.2 Nonlinear Imaging

In addition to conventional B-mode imaging, nonlinear imaging techniques have been introduced recently and investigated in active research as of today. In B-mode imaging, the received echo signal amplitude, therefore the constructed image itself, is a linear function of the transmitted ultrasound pulse. Therefore the echo signal amplitudes scale proportionally with transmit signal amplitudes and have the transmitted frequency content. Nonlinear ultrasonic imaging techniques use the harmonic distortion information extracted from the received echo signals in a pulse-echo imaging system. Two main nonlinear imaging techniques are tissue harmonic imaging (THI) and contrast agent imaging methods. In THI the source of harmonic distortion in the echo signals is nonlinear wave propagation in the tissue. In contrast agent imaging, the nonlinear mechanical behavior of gas microbubbles generate nonlinear echoes which are used to construct ultrasound images.

1.2.1 Tissue Harmonic Imaging

The speed of sound in tissue is a function of material density such that [18]

$$c = \sqrt{\frac{K}{\rho}} \tag{2}$$

where ρ is the density and K is the bulk modulus of the tissue. In the positive cycle of an ultrasonic sound wave, the propagation medium goes under compression because of the increasing pressure therefore its density increases and the speed of sound decreases.

Conversely in the negative cycle, the medium goes under rarefaction therefore its density decreases and the speed of sound increases. The local change in the sound propagation speed results in distortion of the propagating sound wave as the positive cycle of the wave travels slightly slower than the negative cycle [2]. This effect can be visualized in the pressure waveform shown in Figure 5 [5]. In the figure, the dashed line is the ultrasound wave that is transmitted into the tissue. As the wave propagates within the tissue it gets distorted because of the local changes in sound of speed. The distorted waveform is shown as the solid line. The distortion of the pressure wave results in generation of harmonic content as shown in the plot of spectra of the transmitted waveform and the distorted waveform.

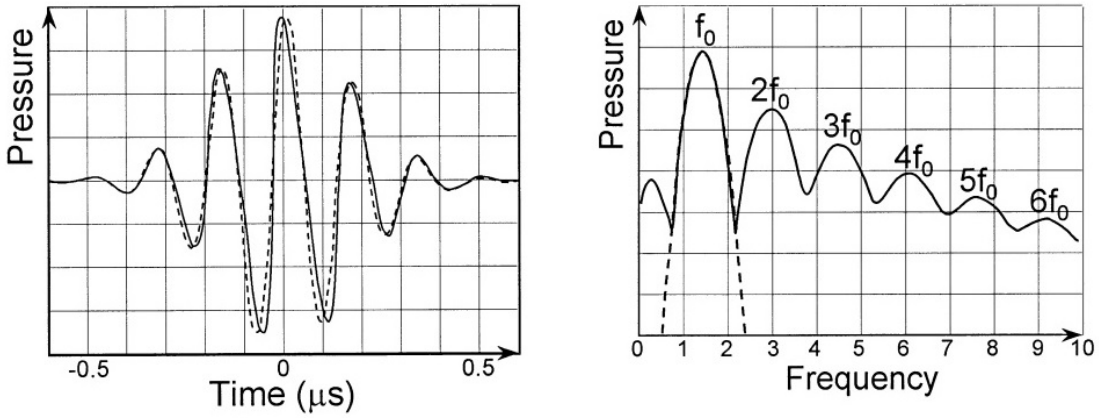

Figure 5: Distortion of the acoustic pulse during propagation within the tissue and its spectrum [5]

The nonlinear propagation in the tissue obeys a power series law as it has been reported that for tissue harmonic imaging [19, 20]. The returned echo can be described as a power series of the transmitted signal where the echo signal can be described as [21]

$$y(t) = a_1 x(t) + a_2 x^2(t) + a_3 x^3(t) + \ldots \tag{3}$$

where $y(t)$ is the echo signal, $x(t)$ is the transmitted waveform and a_n are the power series coefficients. For linear wave propagation, only the coefficient a_1 is nonzero. For harmonic

excitation $x(t) = \cos \omega t$ the first three higher order terms in Equation 3 are

$$\begin{aligned} x^2(t) &= \frac{1}{2}\left(1 + \cos 2\omega t\right), \\ x^3(t) &= \frac{1}{4}\left(\cos \omega t + \cos 3\omega t\right), \\ x^4(t) &= \frac{1}{8}\left(3 + 4\cos 2\omega t + \cos 4\omega t\right). \end{aligned} \tag{4}$$

Tissue harmonic imaging method utilizes the harmonic content caused by nonlinear distortion to construct ultrasound images. Using transmit pulses at the fundamental frequency and the harmonic content within the received echo signals, frequency selective nonlinear images of tissue are constructed. Tissue harmonic imaging techniques offer distinct advantages over linear methods in terms of image resolution, clutter, side and grating lobe levels [2,5]. Moreover, since the nonlinear waves originate within the field of view, aberration artifacts are reduced due to the one way propagation as compared to two way propagation in conventional imaging. Clinical studies also report that patients with features those are not visible in linear ultrasonic images can be examined via harmonic imaging with success [22]. Conventional and second harmonic images of the brain of a 32-week-old fetus are shown in Figure 6 as an example [5]. The harmonic image provides clearer and more detailed depiction of the corpus callosum and the cerebellum as shown by the arrows in the images.

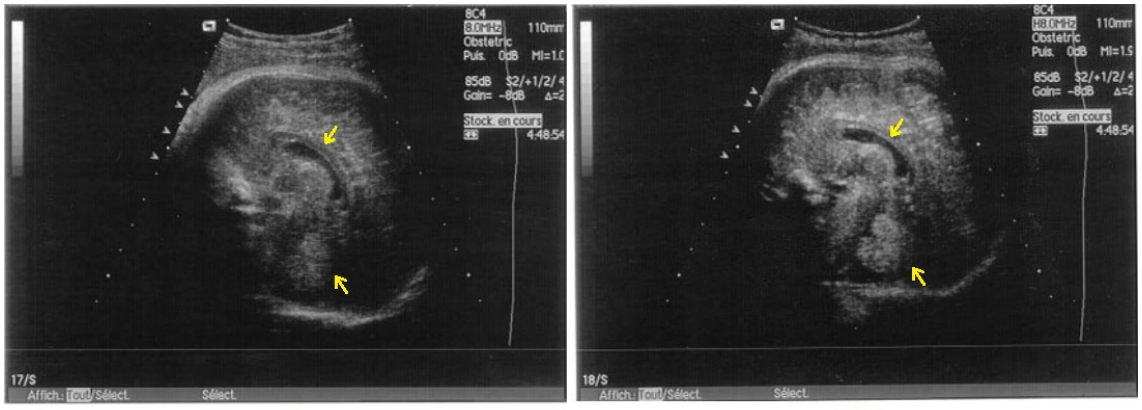

Figure 6: Fundamental (a) and harmonic (b) image of the brain of a 32-week-old fetus [5]

Successful extraction of the nonlinear content in the received echo signals is crucial for

nonlinear imaging performance. Illustrative spectra of a typical echo signal composed of the fundamental and the second harmonic content is given in Figure 7 for narrowband and broadband operation. In the narrrowband case, the second harmonic content in the echo signal can be extracted by band-pass filtering. Considering that the harmonic levels may be 30 dB below the fundamental level, [2], this approach requires high-order filtering to adequately attenuate the fundamental component. Moreover for band-pass filtering to work, the fundamental and the harmonic components must be well separated in the frequency domain, corresponding to longer pulse sequences in the time domain, hence poorer axial resolution in the image space.

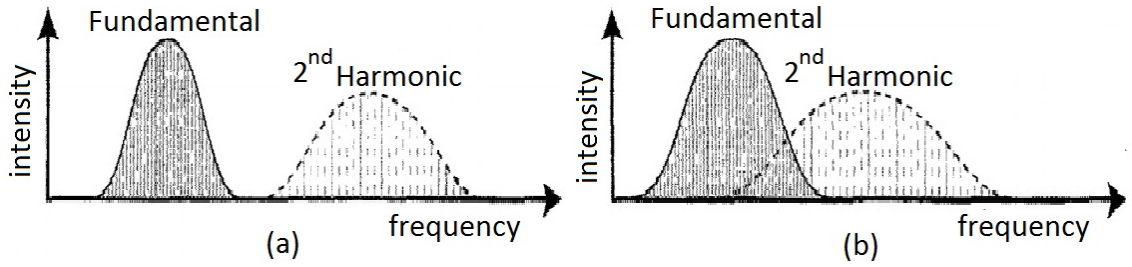

Figure 7: (a) Narrowband imaging: the harmonic and fundamental content in the received echo is seperated spectrally (b) Broadband imaging: the harmonic and fundamental content in the received echo overlap in frequency domain [6]

High quality images with high axial resolution require broadband transmit pulses. As seen in Figure 7(b), the fundamental and harmonic content in the received echo overlap in the frequency domain for a broadband transmit pulse. Because of the spectral overlap, the harmonic content cannot be seperated from the fundamental component via band-pass filtering. As an alternative to the filtering approach, pulse-inversion method has been used widely in practice and clinical studies utilizing broadband harmonic imaging to extract the harmonic content in the echo signals [23, 24]. In this method, first a broadband pulse $x_1(t)$ at the fundamental frequency f_0 is transmitted. The distorted received signal $y_1(t)$ has a fundamental component at f_0 and its harmonics, such that $y_1(t) = a_1x_1(t) + a_2x_1^2(t) + a_3x_1^3(t) + \ldots$. Next, an inverted version of the same transmit pulse, $x_2(t) = -x_1(t)$, is

transmitted, resulting in the echo signal $y_2(t) = -a_1x_1(t) + a_2x_1^2(t) - a_3x_1^3(t) + \ldots$. The addition of two echo signals yield in $y_1(t) + y_2(t) = 2a_2x_1^2(t) + 2a_4x_1^4(t) + \ldots$ where the fundamental and odd harmonics are cancelled out, and the amplitudes of the even order harmonics are doubled. As an additional benefit, the pulse-inversion method also improves the harmonic image SNR. As temporally uncorrelated signals are added up, the noise in the system gets averaged out and the SNR of the second harmonic content increases by 3 dB. However since two transmit events are utilized to construct an image, the frame rate of the imaging system is reduced and the image becomes more susceptible to motion artifacts as a disadvantage. The diagram in Figure 8 describes the pulse-inversion method graphically.

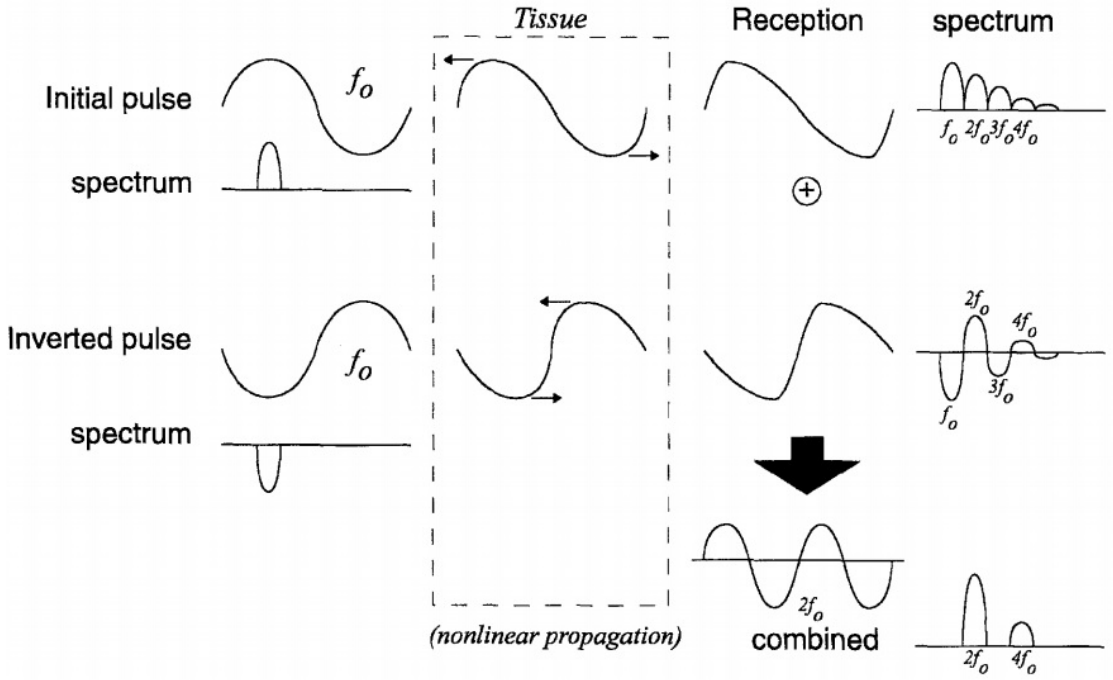

Figure 8: Pulse-inversion harmonic imaging [6]

Another approach employs multiple amplitude modulated pulses to extract the harmonic content in a broadband nonlinear imaging scenario [25]. In this case two pulses $x_1(t)$ and $x_2(t) = Ax_1(t)$ result in two echo signals $y_1(t) = a_1x_1(t) + a_2x_1^2(t) + a_3x_1^3(t) + \ldots$ and $y_2(t) = a_1Ax_1(t) + a_2A^2x_1^2(t) + a_3A^3x_1^3(t) + \ldots$. Scaled addition of the two echo signals allows

extraction of all harmonics such that $y_2(t) - Ay_1(t) = a_2A(A-1)x_1^2(t) + a_3A(A^2-1)x_1^3(t) + \ldots$. A combination of amplitude modulation and pulse-inversion can also be applied for more controlled harmonic content extraction, as presented in [26]. A comparison study of the aforementioned broadband harmonic imaging methods can be found in [21].

All of the aforementioned nonlinear tissue harmonic imaging methods assume that the transmitted pulse is consists of only the fundamental frequency component at f_0. If the transducer is nonlinear, there would be harmonic content in the transmitted ultrasound wave at frequencies $f_0, 2f_0, 3f_0, \ldots$. Linear reflections of the harmonic content in the transmitted signal would therefore contribute to the echo signal, degrading the harmonic image quality since the linear reflections and nonlinear reflections cannot be distinguished. Therefore the ideal transducer is linear as the transducer linearity crucial for harmonic imaging. Moreover, the transducer must be able to receive the higher order harmonics with good sensitivity. Hence, the ideal harmonic imaging transducer is also broadband.

1.2.2 Contrast Enhanced Imaging

Gas filled microbubbles with diameters smaller than 10 μm are utilized in contrast enhanced ultrasonography, as an alternative imaging modality. Utilization of microbubbles in an ultrasound imaging scenario enhances the backscatter signal power as the resonant bubbles behave like simple sources rather than simple reflectors where the microbubble resonance frequency is inversely proportional to its size [27]. The microbubble response to an incident sound wave is illustrated in Figure 9.

When the incident sound wave power is low, the microbubble size follows the incident pressure waveform linearly, enhancing the backscatter signal that can be used to construct conventional B-mode images. However when the incident sound power is increased, the microbubble exhibits strong nonlinear behavior since the bubble can not contract as it can expand, hence the contrast agent transmits a distorted version of the incident wave. The harmonic content caused by nonlinear microbubble response can be used to construct nonlinear ultrasound images utilizing either band-pass filtering the desired harmonic, or the

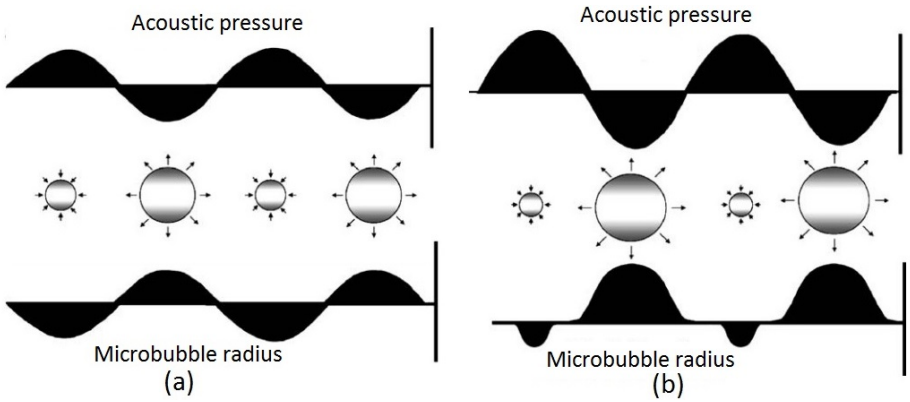

Figure 9: (a) Linear microbubble response to low acoustic power (b) Strong nonlinear microbubble response to high acoustic power [7]

aforementioned broadband imaging techniques such as pulse-inversion. An example nonlinear contrast enhanced image of a liver with hepatocellular carcinoma is shown in Figure 10, compared to the conventional B-mode image, where the defects related to cancer are clearer and more visible in the contrast enhanced image.

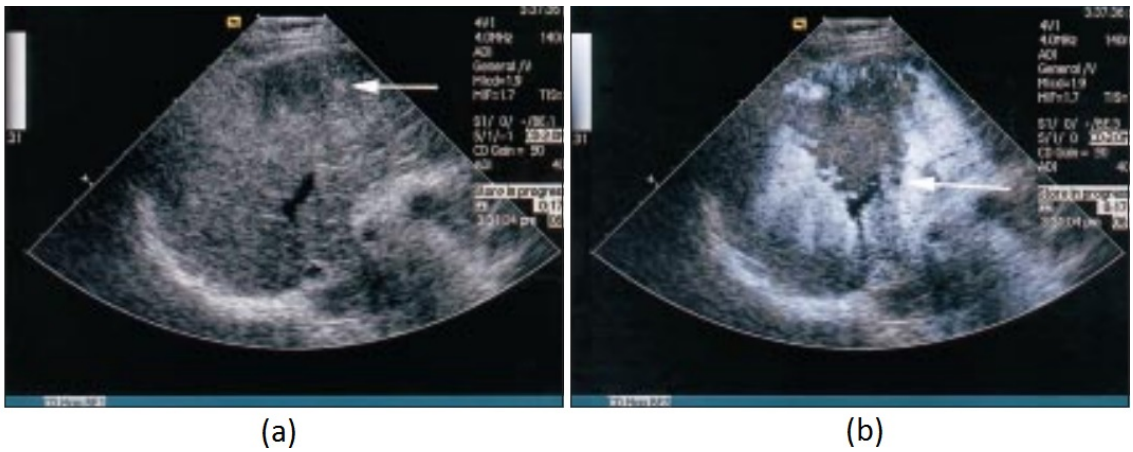

Figure 10: (a) Conventional image of a liver with an ill defined lesion shown by the arrow (b) Contrast enhanced ultrasound image of the liver, showing additional lesions related to cancer [8]

A major difference between the nonlinear microbubble behavior and nonlinear ultrasound wave propagation within a tissue is that the microbubble behavior is not adequately described by the power series relationship as the tissue does [28]. The spectra of the

backscattered signals from Optison microbubbles are given in Figure 11 when the microbubbles are excited with a 2 MHz and a 4 MHz signal [9]. The results show that the scattered signal amplitude is larger in the 2 MHz case, which is close to the resonance frequency of the microbubbles, 2.2 MHz. Also subharmonics and ultraharmonics are present in the microbubble response, which are the 2 MHz and 6 MHz components respectively for the 4 MHz excitation case. The existence of subharmonics and ultraharmonics confirm that the microbubble response indeed can not be described by the power series relationship given in Equation (3) for tissue nonlinearity.

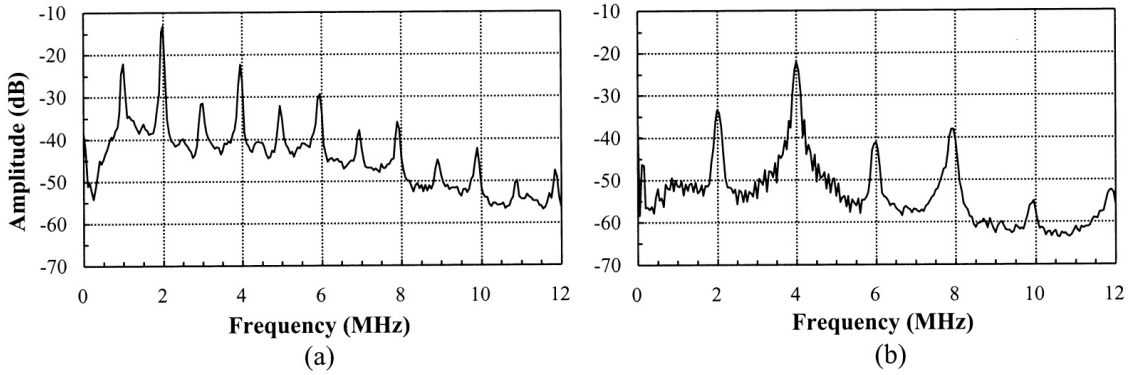

Figure 11: Scatter spectra of Optison microbubbles with 2.2 MHz resonance frequency for (a) 2 MHz excitation and (b) 4 MHz excitation [9]

An important image quality parameter for contrast enhanced imaging is the agent-to-tissue ratio, which measures how strong the echoes backscattered by the contrast agents compared to the echoes reflected by the tissue [29]. One approach to improve the agent-to-tissue ratio exploits the fact that the contrast agents generate subharmonics while the tissue does not, therefore subharmonic imaging naturally improves agent-to-tissue ratio [30]. The difference in the nonlinearity characteristics of tissue and contrast agents is also exploited in a recent second harmonic contrast imaging technique called second harmonic inversion [10]. In this approach, two phase modulated signals with $\pi/2$ rad phase difference are transmitted consecutively and the corresponding echo signals are added up to improve the agent-to-tissue ratio. As a result of the power series relation governing the tissue nonlinearity given in Equation (3), $\pi/2$ rad phase difference in the transmitted signals yield in π

rad phase difference in the second harmonic content in the tissue harmonic signal. Hence when the phase-modulated echo signals are added up, second harmonic content caused by nonlinear propagation within the tissue gets canceled out, while the harmonic content generated by contrast agents remains. The experiment conducted to demonstrate the second harmonic inversion in [10] is shown in Figure 12. In the experiment, a tissue mimicking phantom is immersed in water perfused by microbubble contrast agents. The second harmonic image of the phantom is reconstructed with and without second harmonic inversion. The agent-to-tissue ratio is 20 dB in the second harmonic inversion image while the tissue and the contrast agent perfused region is indistinguishable in the standard second harmonic image.

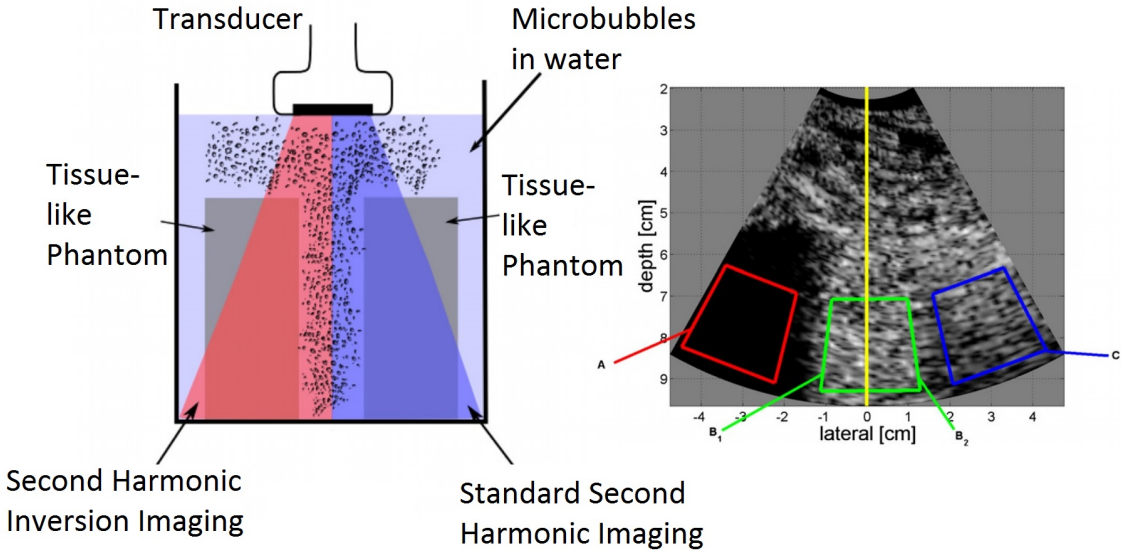

Figure 12: Imaging setup and the constructed second harmonic image where half of the image is constructed with second harmonic inversion [10]

1.3 The Ideal Transducer

The ultrasound image quality is strictly limited by the ultrasound source performance parameters. Desired characteristics of the ideal transducer imposed by the aforementioned ultrasonic imaging modalities can be summarized as follows:

- The ideal transducer is broadband for increased axial image resolution,

- The ideal transducer is broadband so the same transducer can be used to transmit at fundamental frequency f_0, and to receive at harmonics $2f_0, 3f_0, 4f_0, \ldots$ for harmonic imaging,
- The ideal transducer is linear for optimal harmonic imaging performance,
- The ideal transducer is an efficient transmitter with high Pa/V transmit sensitivity and an efficient receiver with high V/Pa receive sensitivity,
- The ideal transducer is capable of generating high output pressure for improved image SNR and penetration depth.

1.4 Piezoelectric Transducers

Since the introduction of the first generation ultrasonic transducers developed in early 20^{th} century for underwater detection and ranging, piezoelectricity have been predominantly used for ultrasound generation and detection. A detailed historical background on development of electroacoustic transducers can be found in [31]. A typical single element focused piezoelectric transducer is shown in Figure 13.

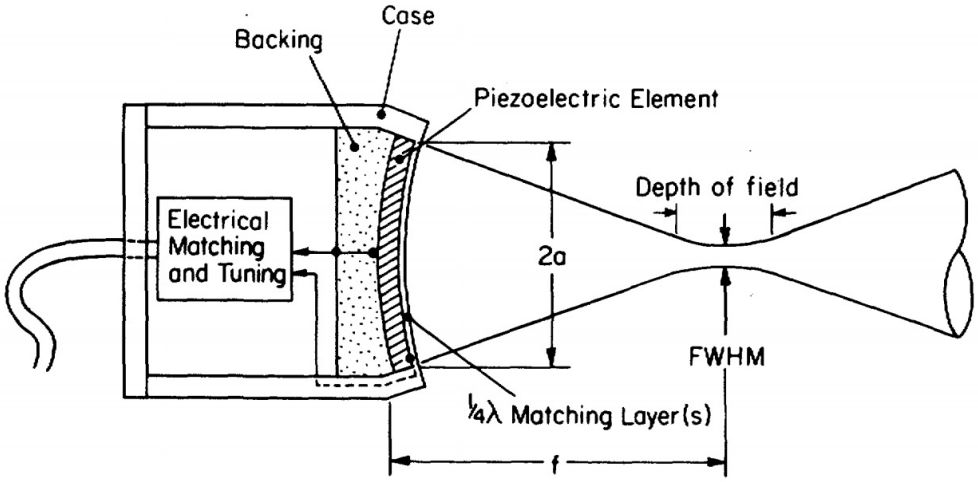

Figure 13: A single circular focused piezoelectric transducer and its beam properties [11]

As discussed in Section 1.1, the lateral resolution of an ultrasound image is set by the

beamwidth of the transducer. The beam characteristics of a transducer are governed by diffraction physics dependent on the transducer geometry. In Figure 13, it can be seen that the beamwidth first narrows down, then spreads again with increasing distance from the transducer. As a consequence the lateral resolution is poor close to and far away from the transducer, and optimal in between. The region where the beamwidth is minimum is called the depth of field and its location and length is determined by the focusing curvature or lens of the transducer. The -6 dB beamwidth or full width at half maximum (FWHM) of the beam within the depth of field is related to the relative size of the transducer to the wavelength and the focal length such that

$$\text{FWHM} = \sqrt{2} f \frac{\lambda}{2a} \tag{5}$$

where a is the transducer radius, f is the focal length and λ is the wavelength.

Ferroelectric lead zirconate titanate (PZT) ceramics have been used extensively as the piezoelectric material in medical imaging because of their strong piezoelectic properties, yielding in good transduction sensitivity. However PZT based transducers are narrowband because of the large acoustic impedance mismatch between the transducer (~35 MRayl) and tissue (~1.5MRayl), therefore PZT transducers suffer from low axial resolution and are not ideal for imaging modalities that require broadband operation such as harmonic imaging. Quarter-wave matching layers, lossy backing materials and electrical matching circuits are used to improve the bandwidth of PZT transducers with a trade-off of complicated construction process. Moreover, PZT ceramics are mechanically diced to construct imaging arrays and the resonance frequency of a piezoelectric transducer is determined by its thickness, hence handling and fabrication of small elements required for high frequency applications is challenging. A PZT based 48 MHz, 8 element annular array with 52% fractional bandwidth is shown in Figure 14(a) where the array diameter is 2 mm [12]. The annular array structure gives the capability to adjust the curvature of the transducer electronically by introduction of time-delays to the applied drive signals to the array elements. Therefore by simple adjusting of the time-delays, the focal point of the transducer

can be adjusted. As another fabricated PZT array example, a 4.3 mm diameter, 20% -6dB FBW, 55 element, 4.6 MHz ring array is shown in Figure 14(b) [13]. For the fabrication of this array, a rectangular PZT ceramic was diced and wrapped around a catheter tube manually. The two-dimensional ring structure gives the array three-dimensional volume imaging capability via synthetic aperture imaging [32].

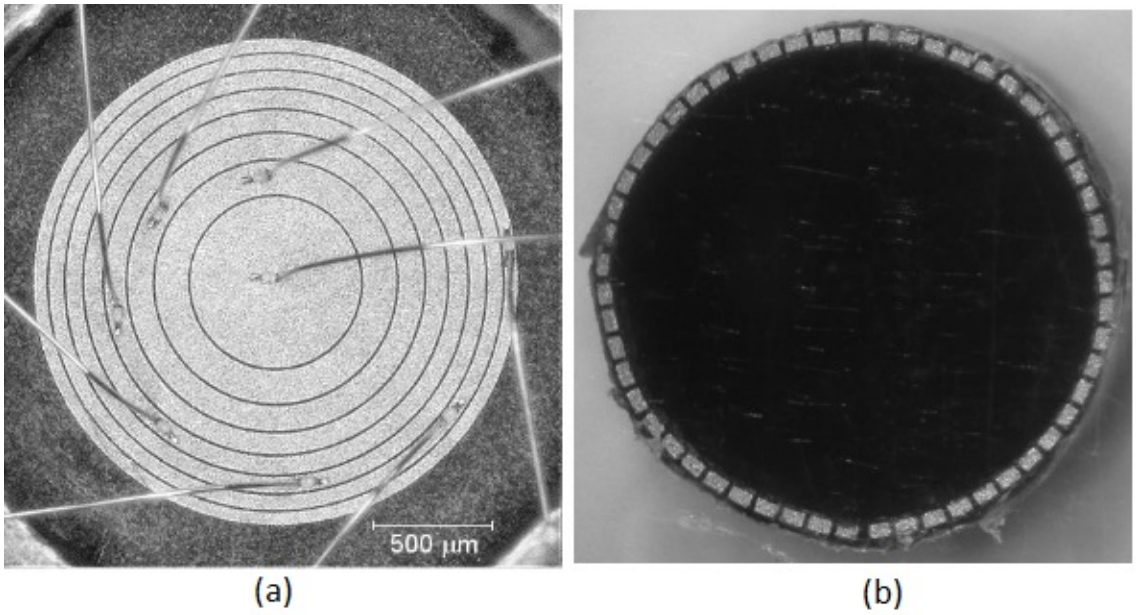

Figure 14: (a) PZT based annular array for side-looking intravascular ultrasound [12] (b) PZT based ring array for forward-looking intravascular ultrasound [13]

Polyvinylidene difluoride (PVDF) transducers have also been utilized in medical ultrasound as an alternative to overcome the bandwidth problems associated with the high acoustic impedance of PZT ceramics. The acoustical impedance of the piezoelectric plastic material PVDF is one order of magnitude smaller than PZT ceramics (~3.5 MRayl vs. ~35 MRayl), so they can be used to construct wide-band transducers. However PVDF based transducers suffer from low electroacoustic transduction efficiency because of their relatively weaker piezoelectric properties. A detailed review of PZT and PVDF based transducers can be found in [11].

1.5 Capacitive Micromachined Ultrasonic Transducers

Capacitive Micromachined Ultrasonic Transducers (CMUTs) are silicon based micro-electro-mechanical systems (MEMS) that operate in ultrasonic frequencies, typically in the MHz range. Following the adaptation of integrated circuit (IC) fabrication technology to micro-machining, first operational CMUTs were introduced in 1990s showing great promise for use in ultrasonic transduction because of their broad operation bandwidth with comparable sensitivity to PZT ceramics and complementary metal-oxide-semiconductor (CMOS) IC compatibility [33]. CMUTs utilize electrostatic actuation to transmit ultrasound signals and perform capacitive sensing for the reception of the incident ultrasound waves. The cross section of a typical CMUT membrane is shown in Figure 15.

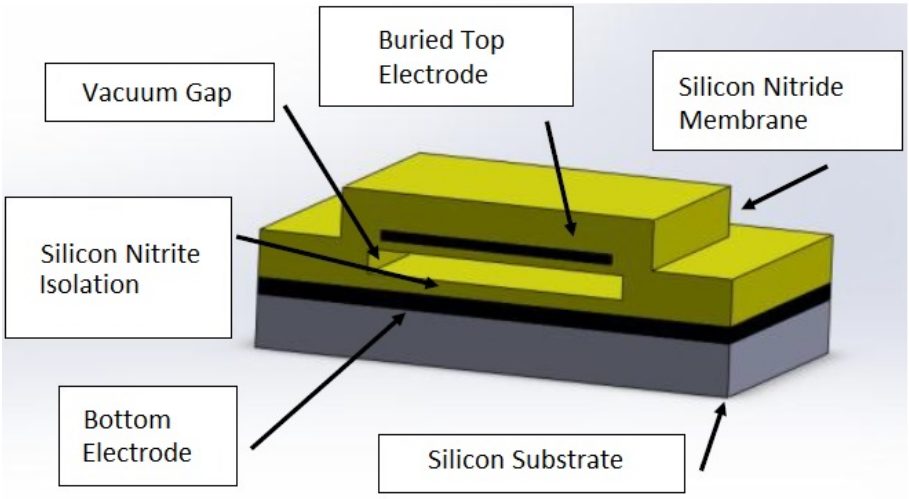

Figure 15: Cross section of a typical CMUT membrane

Although different experimental materials have been proposed for membrane fabrication such as single crystal silicon [34] or diamond, [35], a typical CMUT is comprised of Silicon Nitride (SiN_X) membranes with buried metal electrodes. When an electrical potential is applied to the electrodes, the electrostatic forces deform the membrane from the charge build up on the CMUT capacitance. Electrostatic actuation with an ac signal vibrates the membrane and results in ultrasound transmission into the immersion medium. In receive mode, the incident ultrasound field vibrates the CMUT membrane, resulting in a

change in the device capacitance. If a constant voltage is applied to the CMUT electrodes, the change in the capacitance results in an ac current output such that

$$i(t) = \frac{dQ(t)}{dt} = \frac{d\{VC(t)\}}{dt} = V\frac{dC(t)}{dt}, \tag{6}$$

where $i(t)$ is the current output, $Q(t)$ is the charge on the CMUT capacitance $C(t)$ and V is the voltage applied to the electrodes. The output current is then fed to the readout circuitry for processing of the signal received.

CMUTs offer distinct advantages over their piezoelectric counterparts in terms of cost reduction from batch microfabrication, improved bandwidth and ability to manufacture small elements capable of integration with CMOS electronics. When compared to piezoelectric transducers, a CMUT generally has a lower motional impedance, allowing for operation with a broader bandwidth. For imaging purposes, this leads to improved axial resolution as well as the ability to better utilize harmonic imaging techniques when the same element is used for both transmit and receive operation in a wide frequency range. CMUTs are also an attractive option for high frequency applications since the necessary small element sizes can be attained using established micromachining techniques derived from IC manufacturing technology. Additionally, CMUTs can be monolithically integrated with front end electronics through the use of low temperature fabrication processes resulting in compact arrays with low noise for ultrasound imaging systems [36, 37].

Exploiting the aforementioned advantages of CMUTs over piezoelectric transducers, a wide variety of CMUT arrays have been realized for demanding high frequency applications. A 1.15 mm diameter, 64 element 14 MHz CMUT ring array is shown as an example in Figure 16 [14]. The fractional bandwidth of the array is reported to be 70%. The array is applicable to forward-looking intravascular ultrasound imaging of arteries with diameters of ~1.5 mm, which is not feasible with ring arrays based on piezoelectric transducers. Another example is an 8 element annular side-looking intravascular ultrasonic imaging array, shown in 17 [15]. The array diameter is 840 μm and has 20 MHz center frequency with 100% fractional bandwidth.

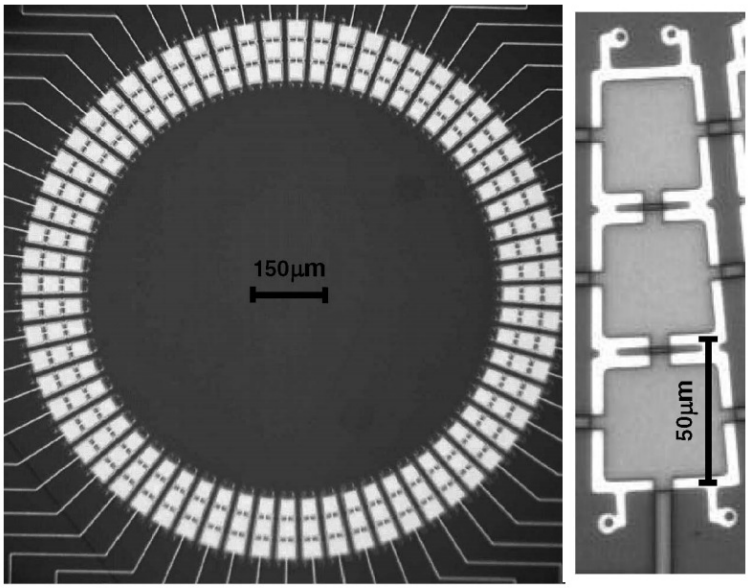

Figure 16: CMUT ring array fabricated on silicon substrate [14]

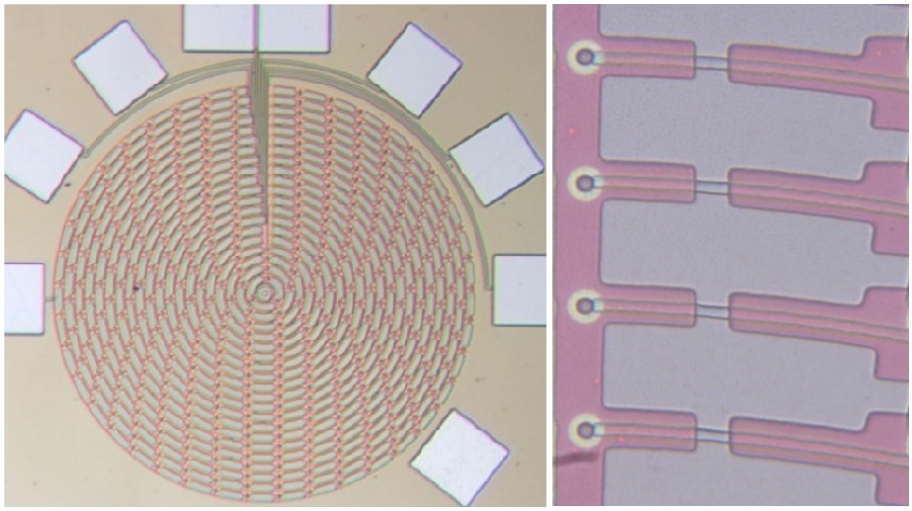

Figure 17: 8 element 840 μm diameter annular array composed of 18 μm $\times$ 60 μm membranes [15]

Although CMUTs provide an attractive alternative to piezoelectric transducers for ultrasonic imaging, they suffer from low output pressure and SNR. It has been shown that during in vivo comparison tests, the SNR of a standard CMUT array is 10 dB less than the piezoelectric counterpart [38]. Comperative B-mode images of a carotid artery imaged by a linear PZT array (GE 12L) and a CMUT array is shown in Figure 18. The PZT array used in the comparison experiment has center frequency of 9 MHz and 80% fractional bandwidth,

and the CMUT array has center frequency of 6 MHz with 110% fractional bandwidth. The CMUT image has better definition of the artery because of its superior bandwidth and axial resolution. On the other hand the CMUT image has less SNR, especially visible in the lower part of the image, which points the lower sensitivity of the CMUT array.

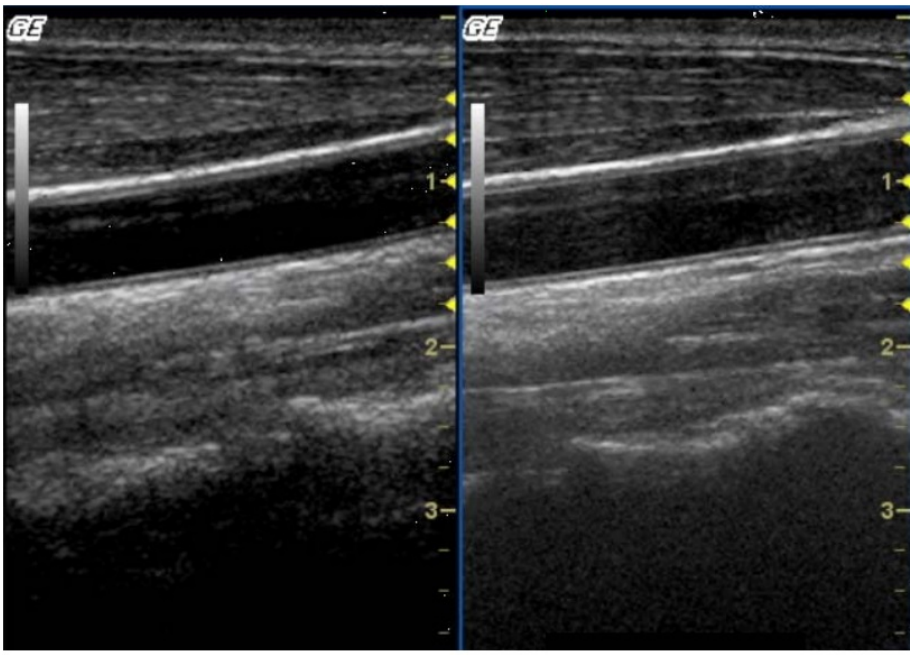

Figure 18: Carotid artery image from a PZT array (left) and a CMUT array (right) [16]

For ultrasound imaging applications, the operation of a piezoelectric transducer is considered to be linear in both transmit and receive modes of operation. For this linear device, the transducer is reciprocal, and the same optimized characteristics would apply to both transmit and receive mode. Unlike piezoelectric transducers, CMUTs exhibit highly nonlinear behavior because of their electrostatic actuation mechanism [39]. Nonlinear transducer dynamics render the aforementioned multiple pulse techniques in Section 1.2 inapplicable to CMUTs, as simply inverting the input pulse does not invert the output pressure or scaling the input voltage does not scale the output pressure linearly. Additionally, linear echoes and nonlinear echoes cannot be distinguished using existing methods due to harmonic distortion of the transmitted signal. To overcome these issues several methods based on pre-distortion of input signals have been proposed to suppress the harmonic content in

the transmitted waveforms [40–43]. Utilizing the wide-frequency band operation offered by CMUTs and pre-distorted waveforms, experimental imaging results have been reported, demonstrating the potential of CMUTs in tissue harmonic and contrast imaging [44, 45]. Recently, it has been demonstrated that 2nd harmonic component in the transmitted signal is eliminated in the far-field by transmitting two pulses with $\pi/2$ rad phase difference from two sub-array elements in a checker board array architecture [46]. It is reported that a general 2^{nd} order distortion model is applicable to CMUTs and the proposed approach suppresses the 2^{nd} harmonic in the expense of 3 dB intensity reduction. Also recently, it was suggested that the nonlinear echoes from microbubbles can be extracted using a bias modulation scheme in CMUT based imaging systems [47]. It is shown that the transmitted fundamental component amplitude is proportional to the dc bias if the ac signal amplitude is kept constant and gap dependence of the electrostatic force acting on CMUT membrane is neglected. By transmitting three pulses with different dc bias and constant ac signal amplitude values, the nonlinear echoes from bubbles can be extracted by simple addition of the received signals. This method is covered further in detail in Chapter 5.

1.6 CMUT Modeling

Availability of simple one-dimensional equivalent circuit models such as the KLM and Mason models and development of robust finite element analysis (FEA) tools has been crucial to the success and proliferation of ultrasound devices and systems based on piezoelectric transducers [18]. While important progress has been made in CMUT fabrication technology and system integration as many groups can build CMUT based experimental systems [48–53] and first commercial linear CMUT probes have emerged [54], CMUT design optimization for many important applications is still a big challenge, especially when interfaced with a system. In contrast with piezoelectric transducers, which behave linearly in wide dynamic range, CMUTs are highly nonlinear especially during transmission when

large membrane displacements are required to achieve the desired pressure levels. In addition, the CMUT membrane structures and array configurations can have large variety, from circular to rectangular membranes to ones with substrate embedded springs, from regular one-dimensional arrays to dual-ring or annular imaging arrays which can have complex acoustic interactions [55, 56]. Consequently, initial small signal equivalent circuits have been of very limited use however they are worth mentioning as they give insight to device behavior [39]. The one-dimensional nonlinear analysis methods have been been significant, and several large signal equivalent circuits have also been developed, but these are limited to infinite symmetrical arrays and uniform circular membranes [57,58]. This leaves computationally intensive three-dimensional transient FEA as the main tool to accurately model the nonlinear behavior of the CMUT arrays. Although it can be considered the gold standard, the large FEA simulation domains required to capture the complex acoustic interaction between the CMUT array elements severely limits these methods to small portions of imaging arrays with symmetry assumptions which are not realistic in many practical cases, even not considering the electrical circuit interface. Nonlinear simulations are especially needed for demanding applications such as tissue harmonic imaging where suppression of CMUT nonlinearity in an efficient manner requires an accurate model [44]. Coupling the CMUT array model with the electronics is also important not only because CMUTs are closely integrated with front end transmit and receive electronics most of the time, but also because the nonlinear dynamic behavior of the CMUTs and the cross coupling would have important consequences for the overall behavior of the integrated system.

1.6.1 Lumped Parallel-plate modeling of a single CMUT membrane

In the early modeling efforts for CMUTs, a single CMUT membrane was modeled as a lumped parallel plate actuator based on Mason's equivalent circuit for piezoelectric actuators [31, 39, 59]. First order parallel-plate CMUT model where the transducer is modeled as a spring-mass-dashpot system in vacuum is shown in Figure 19.

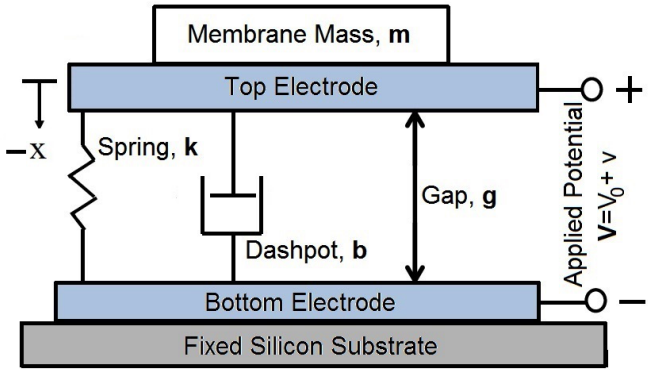

Figure 19: First order parallel plate CMUT model

The dynamic behavior of the parallel-plate CMUT is governed by a nonlinear second-order ordinary differential equation (ODE) where the driving force is the electrostatic force, such that [39]

$$m\ddot{x}(t) + b\dot{x}(t) + kx(t) = \frac{-\epsilon_0 A}{2}\left(\frac{V(t)}{g_0 + x(t)}\right)^2, \tag{7}$$

where m, k, b are the stiffness, mass and damping coefficients of the spring-mass-dashpot system respectively, g_0 is the initial parallel-plate gap, A is the parallel-plate area, $x(t)$ is the parallel-plate displacement and $V(t) = V_0 + v(t)$ is the applied voltage signal composed of a dc value V_0 and a time varying part $v(t)$. It should be noted that the dashpot models the mechanical losses within the CMUT membrane as the only loss term since there is no fluid loading in vacuum.

1.6.2 Static Analysis and Collapse

When a stationary voltage signal $V(t) = V_0$ is applied to the parallel-plate CMUT, the velocity and the acceleration of the parallel-plate vanishes at steady state and the governing differential equation becomes a third order nonlinear polynomial in terms of displacement for given voltage such that

$$kx = \frac{-\epsilon_0 A}{2}\left(\frac{V_0}{g_0 + x}\right)^2 \tag{8}$$

meaning that the spring force kx is balanced by the electrostatic force at equilibrium point x. The spring force on the left hand side of Equation (8) is a linear function of displacement while the electrostatic force on the right hand side is a nonlinear function of displacement. For $V_0 > V_{collapse}$ Equation (8) does not have a stable solution for x where [60]

$$V_{collapse} = \sqrt{\frac{8kg_0^3}{27\varepsilon_0 A}}. \tag{9}$$

The lack of a stable solution means that the parallel-plate becomes unstable for $V_0 > V_{collapse}$, where the electrostatic force can not be balanced by the spring force and the parallel-plate collapses to zero gap. Plugging $V_{collapse}$ in (8) yields in

$$x_{collapse} = \frac{-g_0}{3}, \tag{10}$$

meaning that stable static displacement of the parallel-plate CMUT is limited to 1/3 of its initial gap only.

1.6.3 Small-signal Analysis

The nonlinear differential equation governing the parallel-plate dynamics can be linearized around an operating point if $v(t) \ll V_0$ and $x(t) \ll x_0$ where x_0 is the operating point displacement corresponding to V_0 and it can be calculated by substituting V_0 in the static solution polynomial given in Equation (8) [39, 60]. The Taylor series expansion of (7) around $v(t) = V_0$ and $x(t) = x_0$ results in

$$m\ddot{x}(t) + b\dot{x}(t) + \left[k - \frac{\epsilon_0 A V_0^2}{(g_0 + x_0)^3}\right] x(t) = \frac{-\epsilon_0 A V_0}{(g_0 + x_0)^2} v(t). \tag{11}$$

neglecting higher-order terms in the expansion. Equation (11) describes the linear relationship between the small-signal input $v(t)$ and the small-signal parallel-plate displacement $x(t)$ with the effective spring constant

$$k_{eff} = k - \frac{\epsilon_0 A V_0^2}{(g_0 + x_0)^3}. \tag{12}$$

It can be observed that the effective spring constant governing the linear relationship decreases as the dc bias V_0 increases. This effect is called *spring softening* and results in

decrease in the resonance frequency of the transducer as the resonance frequency of the linearized second order governing ODE is $\omega_0 = k_{eff}/m$.

Equation (11) can be analogously described by the Mason equivalent circuit given in Figure 20 for harmonic excitaton and with addition of fluid loading [39]. In the figure, C_p is the parasitic capacitance, C_0 is the parallel-plate capacitance at the operating point for V_0 such that

$$C_0 = \frac{\varepsilon_0 A}{g_0 + x_0}, \tag{13}$$

n is the transformer ratio relating the applied small signal excitation voltage, and the resulting electrostatic force F_{ES}

$$n = \frac{\epsilon_0 A V_0}{(g_0 + x_0)^2}, \tag{14}$$

and Z_m is the mechanical impedance of the spring-mass-dashpot such that $Z_m = b + j\omega m + k/j\omega$. The radiation impedance Z_r is the relationship between the velocity of the parallel plate and the total fluid loading acting on the parallel plate resulting from it's own motion, F_L [17].

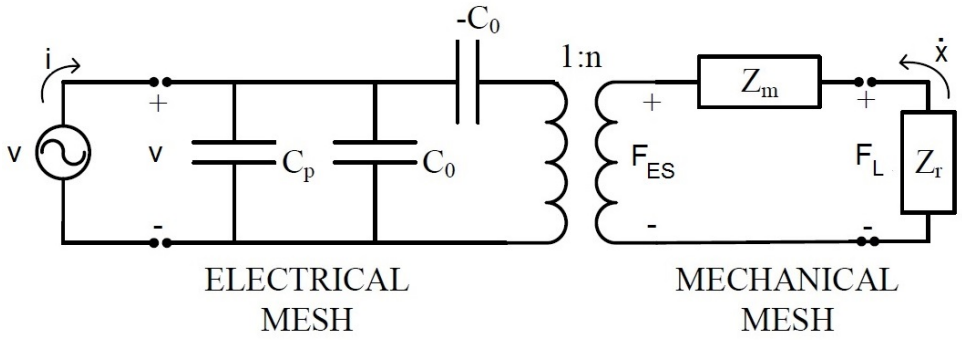

Figure 20: Mason equivalent circuit for the linearized parallel-plate CMUT

A direct conclusion from observation of the equivalent circuit given in Figure 20 is that higher turns ratio n results in better sensitivity both in transmit mode, from input voltage to parallel-plate velocity, or in receive mode, from parallel-plate velocity to output current. So as the CMUT is biased closer to the collapse voltage, transduction sensitivity improves.

1.6.4 Array Models

General modeling and optimization methods that cover a large domain of possible CMUT designs are crucial since any arbitrary membrane and array geometry is feasible within the limits of current microfabrication technology. This fabrication flexibility is a major advantage over the piezoelectric transducers. However, general large signal modeling and optimization methods for CMUTs are not well established, leaving a wide gap in CMUT research.

The equivalent circuits are simple to solve using circuit analysis techniques and provide insight into the CMUT behavior. However, these models neglect the nonlinearities inherent to the parallel plate actuator and do not consider the higher order membrane modes that influence CMUT element behavior [61]. Moreover, these techniques do not describe the large signal dynamics of CMUTs, which is desirable for operation in transmit mode and behavior in an array configuration.

To address the aforementioned limitations, a number of approaches have been proposed and implemented based on equivalent circuit modeling [57, 62–65]. These efforts significantly improve upon the ability to model nonlinear behavior in two dimensional arrays. In general, these models focus on CMUTs and arrays with uniform cross-sectional geometries and circular membrane shapes. However, the design space for CMUT optimization is extensive, including the ability to manufacture arbitrary membrane shapes (elliptical, rectangular, trapezoidal, etc.) with varied cross-sections, using substrate embedded springs, and incorporating multiple electrodes into a single membrane [53, 66, 67]. Another approach deviates from the equivalent circuit model using finite element analysis (FEA) to perform modal, harmonic, and transient simulations in a 3D fluidic environment [68, 69]. While FEA modeling is capable of dealing with the complex CMUT geometries, it becomes computationally expensive as the array size increases, predominantly associated with the modeling of the fluidic environment. For optimization of individual CMUT membrane geometries and array configurations, this approach is not ideal due to the significant

computational time necessary for each simulation.

An alternative approach for small signal modeling of CMUT arrays, formulated by Meynier et al., utilized finite difference approximations of Timoshenko's thin plate equations to model the CMUT membranes [70, 71]. The acoustic radiation modeling was accomplished using the boundary element method (BEM) which only meshes the vibrating surface area of the CMUT array and does not require 3D fluidic meshing [72]. Since this is a 2D surface mesh over the CMUT membranes, the computational load is significantly reduced as compared to 3D FEA. For small signal analysis of CMUT arrays, this model has been shown to be accurate, as in the case of thermal-mechanical noise modeling of CMUT arrays as presented in [56]. However, this method is limited to the small signal analyses around the bias point of CMUTs with thin membranes, and is not valid for nonlinear transmit modeling. In [73], this method was extended to transient analysis of the displacement of a single CMUT membrane.

1.7 Optimization of CMUTs

In the receive mode, the CMUT can be modeled as a linear device and the behavior can be described through small signal analysis at the operating point for a given dc bias. However, in the transmit mode CMUT arrays must be optimized to operate close to their physical limits, requiring large signal operation where the electrostatic nonlinearities dominate the CMUT dynamics and cannot be neglected [74]. Hence, an optimal CMUT for receiving is not necessarily the optimal device for the transmission of ultrasound waves.

To improve the overall SNR for a CMUT imaging array, there has been extensive research for increasing the receive sensitivity as well as increasing the transmit pressure. Masons equivalent circuit has been used to evaluate the performance of a CMUT in the receive mode [39, 59]. In this equivalent circuit, the transformer ratio defines the relationship between the membrane velocity and the current generated. Research efforts to improve the linear receive performance of CMUTs are predominantly based on increasing

the transformer ratio. It has been shown that electrode coverage in a CMUT membrane can be designed for an increased transformer ratio, which results in optimized CMUT receive performance [75]. Additionally, it has been shown that for a given CMUT device, the transformer ratio when biased close to the collapse, is maximized and is inversely proportional to the initial vacuum gap [76]. Therefore, for optimal receive sensitivity, the desired CMUT design should have as small a vacuum gap as possible limited by fabrication capabilities. With a dual electrode design, side electrodes are used to adjust the initial gap under the center receive electrode through leveraged bending which has been shown to increase the transformer ratio.

Assuming a simple acoustic source, the transmitted pressure from a CMUT is proportional to the total volume acceleration. Therefore, at a given frequency, vertical membrane displacement needs to be maximized. Then, minimizing the CMUT gap for optimized received performance is counter productive for transmit operation and different optimization strategies have been pursued. Research efforts to increase the CMUT transmit performance have resulted in a wide variety of CMUT element, array, and drive configurations where the CMUT transmit element is the same as the receive element and for the case with separate transmit and receive elements. A dual-ring CMUT array structure was presented where the transmit and receive elements are separated, so the optimization can be done separately in terms of biasing [77, 78]. CMUTs designed with side electrodes for leveraged bending were utilized for the transmit mode to increase the volumetric fluid displacement [79]. Huang et al. showed that the output pressure can be increased by designing CMUT arrays with rectangular membrane shapes as compared to square membranes [80]. Non-uniform membrane CMUTs were introduced and analyzed which result in more parallel-plate like membrane motion and improved pressure output and bandwidth [67, 81, 82]. Also, parallel-plate CMUTs with embedded springs were introduced for increased transducer performance [53].

In addition to the transmit improvements based on optimization of CMUT geometry for higher power output in conventional mode, different driving configurations were also proposed, including deep collapse and collapse-snap-back modes of operation, which increases the pressure output of the CMUT [83]. The proposed collapsed mode operation of CMUTs were further investigated and compared to conventional CMUT operation in [84, 85]. For continuous wave applications such as high intensity focused ultrasound (HIFU), it has been demonstrated that CMUT nonlinearity and output pressure can be improved by designing CMUT arrays to operate at the frequency where the radiation impedance is maximum [86]. The CMUT design space involving all of the transducer design strategies mentioned above give the transducer designer a large set of options for transmit CMUT optimization.

CHAPTER 2

FIRST ORDER ANALYSIS AND COMPENSATION OF CMUT NONLINEARITY

2.1 Motivation and Background

The wider bandwidth of CMUTs allows for the use the same element as a transmitter at fundamental frequency f_0 and as a receiver for higher harmonics. However, CMUTs are nonlinear transducers since the electrostatic force applied to the transducer membrane is a nonlinear function of the input voltage and the instantaneous gap between the electrodes driving the transducer. This nonlinear dependence of the electrostatic force results in collapse phenomenon [39] and distortion of the transmitted ultrasound wave. This CMUT nonlinearity is disadvantageous for harmonic imaging, since the harmonic content of the transmitted signal contributes to the harmonic content in the received signal.

Several input shaping methods for CMUTs have been proposed to suppress the harmonic distortion [40–42]. These methods address the voltage square dependence of the electrostatic force acting on transducer membrane as the source of nonlinearity and rely on distorting the input signal in an open loop fashion to suppress unwanted harmonics. Additionally, in order to extend the stable range of parallel-plate actuators, feedback control [87] and charge control [88] methods were presented for static operation. In an effort to stabilize parallel-plate actuators for larger static displacements, it was also shown that adding a series capacitor [89] implements the feedback control of the actuator with a trade-off of increased excitation voltage. In [90], it was also shown that using the RMS value of the AC excitation signal and a tuning inductor can extend the stable quasi-static operating range.

In this chapter, the relationship between the drive signal amplitudes and CMUT nonlinearity is investigated using a first order nonlinear parallel-plate model. Based on the initial

investigation, a feedback linearization method is proposed to reduce the CMUT nonlinearity. Presented simulation and experimental results demonstrate that the CMUT performance is improved for applications where transducer linearity is crucial such as harmonic imaging or high-intensity focused ultrasound (HIFU).

2.2 Nonlinear Parallel-plate Model

CMUT dynamics can be described by a lumped parallel-plate capacitor and piston radiator model to the first order [57]. The multiphysics one-dimensional lumped model of a single circular CMUT membrane is presented in Figure 21, where it is modeled as a parallel-plate capacitor in the electrical domain, as a lossless spring-mass system in the mechanical domain, and a piston radiator in an infinite rigid baffle in the acoustic domain. This model assumes that only the first mode of the membrane is excited when an electrical input signal is applied, and the CMUT membrane is operated in the non-collapsed regime. Higher order modes and other sources of nonlinearities are neglected. Such nonlinearities include the excitation of higher order membrane modes for large deformations and change of charge distribution in the CMUT electrode when the CMUT membrane is deflected. Array operation with acoustic crosstalk and the neglected nonlinearities is studied and modeled in Chapter 3.

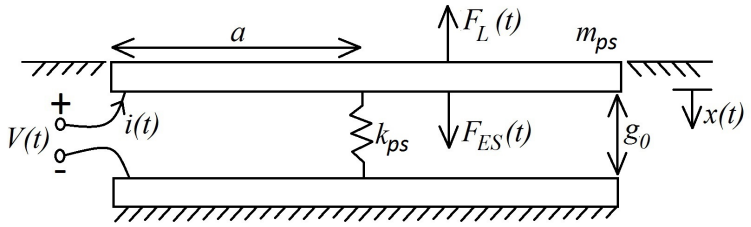

Figure 21: One-dimensional nonlinear CMUT model as a parallel-plate capacitor and a baffled piston.

In Figure 21, $V(t)$ is the excitation voltage, $i(t)$ is the input current, m_{ps} and k_{ps} are the mass and the stiffness of the piston respectively, and g_0 is the initial gap. $F_{ES}(t)$ and $F_L(t)$ are total electrostatic force and fluid loading on the piston, $x(t)$ is the displacement of the

piston, and a is the radius of the piston. The governing differential equations that couple the mechanical, electrical and acoustic domains are

$$\begin{aligned} m_{ps}\ddot{x}(t) + k_{ps}x(t) &= F_{ES}(t) - F_L(t), \\ i(t) &= \frac{d(C(t)V(t))}{dt}, \end{aligned} \tag{15}$$

where $C(t) = \dfrac{\varepsilon_0 \pi a^2}{g(t)}$ is the device capacitance, ε_0 is the permittivity of free space, and $g(t) = g_0 - x(t)$ is the instantaneous gap of the transducer [57]. Defining the Fourier transform of displacement as $\tilde{x}(\omega)$, the inverse Fourier transform operator as $\mathcal{F}^{-1}$ such that $x(t) = \mathcal{F}^{-1}\{\tilde{x}(\omega)\}$, and the radiation impedance as $\tilde{Z}_R(\omega)$, the electrostatic and fluid loading terms are expressed as [39]

$$F_{ES}(t) = \frac{\epsilon_0 \pi a^2}{2}\left(\frac{V(t)}{g(t)}\right)^2, \tag{16}$$

$$F_L(t) = \mathcal{F}^{-1}\left\{\tilde{Z}_R(\omega) j\omega \tilde{x}(\omega)\right\}. \tag{17}$$

The radiation impedance of a circular piston is given as

$$\tilde{Z}_R(\omega) = \rho_0 c \pi a^2 \left(1 - \frac{J_1(2ka)}{ka} + \frac{jH_1(2ka)}{ka}\right), \tag{18}$$

where J_1 is the first order Bessel function, H_1 is the Struve function, ρ_0 is the density of the immersion medium, c is speed of sound in the medium and $k = \omega/c$ is the wave number [17].

Piston stiffness, k_{ps}, is calculated via finite element analysis using COMSOL (Comsol Inc., Burlington, MA) by applying a static uniform pressure, P, over the circular membrane as

$$k_{ps} = \frac{P\pi a^2}{x_{mean}} \tag{19}$$

where x_{mean} is the average displacement of the CMUT membrane. Piston mass, m_{ps}, is then calculated as

$$m_{ps} = \frac{k_{ps}}{(2\pi f_0)^2}. \tag{20}$$

Here, f_0 is the first resonance frequency of the membrane in vacuum and is calculated via eigenfrequency analysis in COMSOL [60].

2.2.1 SIMULINK Model

Differential equations in (15) are solved using SIMULINK (The MathWorks Inc., Natick, MA) to simulate average generated surface pressure, $p(t)$, for an arbitrary input signal, $V(t)$, where

$$p(t) = \frac{-F_L(t)}{\pi a^2}. \tag{21}$$

The SIMULINK model that simulates the transient CMUT behavior for an arbitrary input signal is presented in Figure 22 where the output of the system is the generated average surface pressure, $p(t)$. In the model, the radiation impedance block, $\tilde{Z}_R(\omega)$, is implemented as a finite impulse response filter exhibiting the frequency response expressed in Equation (18).

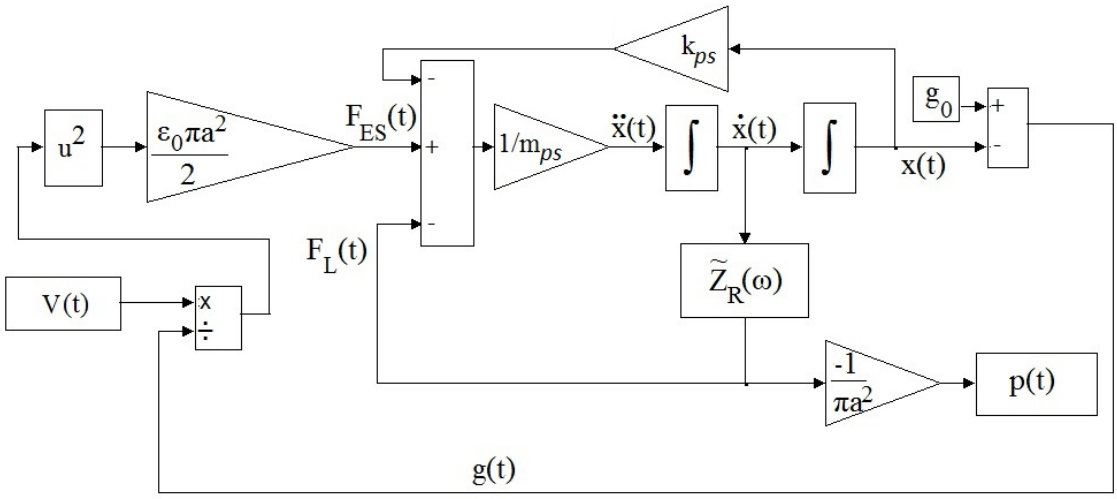

Figure 22: Nonlinear transient model implemented in SIMULINK for an arbitrary input signal and average transmitted pressure on the piston surface

2.3 Large-signal Behavior of the Parallel-plate CMUT

Equations (15) and (16) show that parallel-plate CMUT is a nonlinear dynamical system when the transducer is excited with voltage drive. The nonlinearity is due to the dependency

of the electrostatic force on the input voltage signal and instantaneous gap such that

$$\begin{aligned} F_{ES}(t) &\propto V^2(t), \\ F_{ES}(t) &\propto \frac{1}{g^2(t)}. \end{aligned} \tag{22}$$

given that $g(t)$ is also a nonlinear function of $V(t)$.

Conventionally CMUTs are driven with a voltage signal V(t) that includes dc and ac components, i.e. $V(t) = V_{DC} + V_{AC}\cos(\omega t)$. The square of $V(t)$ is

$$\begin{aligned} V^2(t) &= V_{DC}^2 + 2V_{DC}V_{AC}\cos(\omega t) + (V_{AC}\cos(\omega t))^2 \\ &= \frac{V_{AC}^2}{2} + V_{DC}^2 + 2V_{DC}V_{AC}\cos(\omega t) + \frac{V_{AC}^2}{2}\cos(2\omega t) \end{aligned} \tag{23}$$

using the trigonometric identities and has a dc term, a term at the excitation frequency ω_0 and a second harmonic term.

Harmonic analysis simulations were carried out using the SIMULINK model to investigate the relationship between the parallel-plate CMUT nonlinearity and different drive signal configurations. A transducer with 27 MHz center frequency and 55% 3 dB fractional bandwidth was modeled with dimensions and material properties listed in Table 1 as an example to be examined in the harmonic analysis simulations.

Table 1: Dimensions and Materal Properties Used in Simulations

Radius, a	20 μm
Membrane thickness	3 μm
Initial Gap, g_0	100 nm
Membrane Density	3270 kg/m^3
Membrane Poisson's ratio	0.263
Membrane Young's Modulus	320 GPa
Calculated piston stiffness, k_{ps}	$1.0285x10^6$ N/m
Calculated piston mass, m_{ps}	$22.2081x10^{-12}$ kg
Immersion fluid density, ρ_0	1000 kg/m^3
Sound speed in the immersion fluid, c	1500 m/s

The collapse voltage of the example CMUT is calculated as 165 V via Equation (9). The surface pressure on the transducer surface was simulated for a 3 ns wide 120 V unipolar

pulse with 120 V dc bias. The impulse response of the transducer is presented in time and frequency domains in Figure (23). This transducer is then used in simulations to investigate the nonlinearity in the case of harmonic imaging with f_0=20 MHz, fundamental transmit, and $2f_0$=40 MHz, harmonic receive operation.

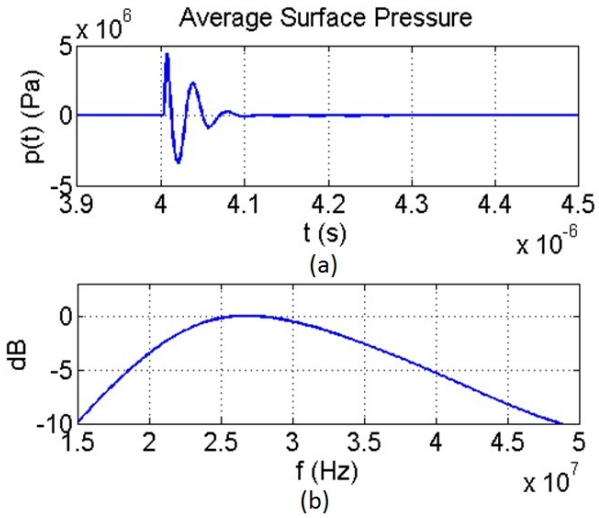

Figure 23: (a) Simulated impulse response of the CMUT where $V(t)$ is a pulse with 3 ns 120 V pulse and 120 V dc bias, (b) Normalized frequency spectrum of the average surface pressure

The model is simulated for different stable V_{DC} and V_{AC} combinations to calculate the harmonic distortion for different drive schemes. In the simulations, the CMUT is excited at the fundamental frequency, f_0 = 20 MHz, where the AC signal is enveloped with a Gaussian curve with a full-width at half-maximum (FWHM) of 1 μs. The amplitude of the f_0 component and the amplitude ratio of 20 MHz to 40 MHz components (harmonic ratio or HR) of the generated surface pressure for the given input signal are presented in Figure 24.

By evaluation of the simulation results shown in Figure 24, it is observed that same output pressure can be achieved at fundamental frequency with different V_{DC} - V_{AC} combinations, resulting in different harmonic component amplitudes. In [40], the harmonic ratio is defined as a function of V_{DC} and V_{AC} such that

$$HR \propto \frac{V_{DC}}{V_{AC}}. \tag{24}$$

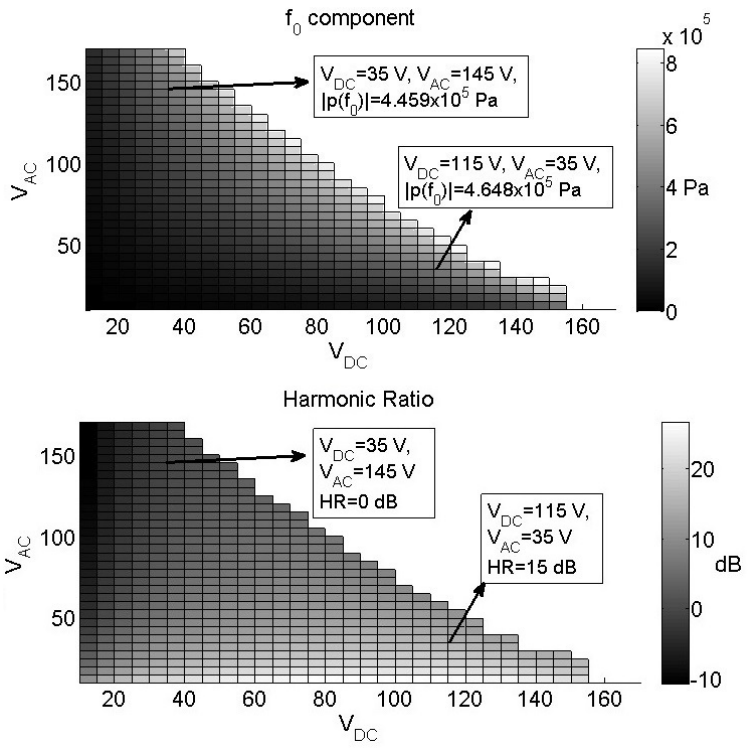

Figure 24: Magnitude of the f_0=20 MHz component and the ratio between 20 MHz and 40 MHz components as a function of V_{DC} and V_{AC}. The excitation frequency is 20 MHz.

The harmonic ratio relationship in Equation (24) is verified with the simulation results in Figure 24. For example, ~460 kPa pressure at 20 MHz is achieved with either V_{DC} =35 V, V_{AC}=145 V and V_{DC} =115V, V_{AC}=35V with harmonic ratios of 0 dB and 15 dB, respectively.

2.3.1 Subharmonic Excitation

According to Equation (24), the harmonic ratio becomes null for V_{DC}=0 V, suggesting that no signal is transmitted at the fundamental frequency. This interesting case can also be analyzed via Equation (23) by setting V_{DC}=0 V, such that

$$V^2(t) = \frac{V_{AC}^2}{2} + \frac{V_{AC}^2}{2}\cos(2\omega t). \tag{25}$$

If the gap dependence of the electrostatic force is neglected, then the electrostatic force has only a dc component in addition to a sinusoidal term at twice the excitation frequency. Exploiting this observation, the nonlinearity caused by the voltage square dependence can

be suppressed by exciting the transducer at half the operation frequency, $\omega = \omega_0/2$, without dc bias where ω_0 is the desired fundamental frequency.

The SIMULINK model is simulated for subharmonic excitation of the transducer at 10 MHz without dc bias to evaluate the performance of the aforementioned subharmonic excitation method. For comparison to the conventional excitation scheme at the fundamental frequency with dc bias, the fundamental component amplitude and the harmonic ratio is evaluated as a function of the AC signal amplitude. In the simulations, the CMUT is driven with $V(t) = V_{AC}E(t)\cos(\omega_0/2)$, where $E(t)$ is the same Gaussian envelope used in the simulations for the conventional excitation case. The output pressure component at 20 MHz is plotted as a function of the excitation signal amplitude in Figure 25 for V_{AC} values which does not collapse the parallel-plate.

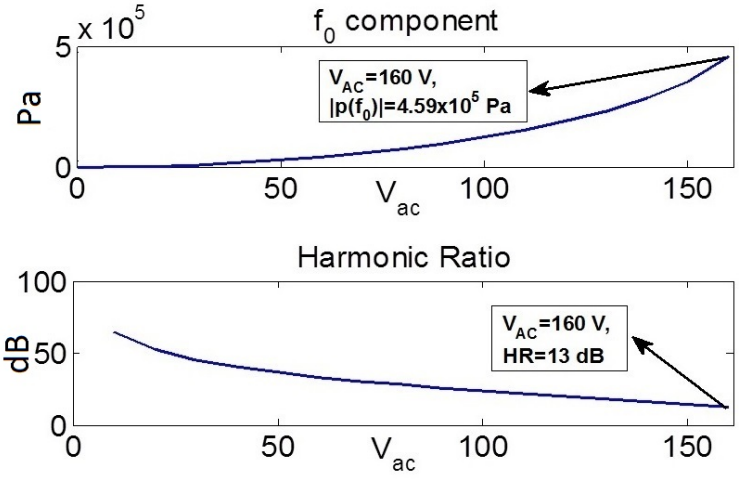

Figure 25: Magnitude of the f_0=20 MHz component and the ratio between 20 MHz and 40 MHz components as a function of V_{AC} with no V_{DC} applied. The excitation frequency is $f_0/2$=10 MHz.

In the subharmonic excitation case, the same pressure, ~460 kPa, is achieved with V_{AC}=160 V with a harmonic ratio of 13 dB, which shows minimal improvement over the conventional 20 MHz excitation case with V_{DC} =115 V and V_{AC}=35 V. This observation suggests that subharmonic excitation of the transducer does not compensate for the nonlinear distortion by itself, and the nonlinearity of the transducer is mainly caused by the

inverse gap dependence of the electrostatic force.

2.4 Gap Feedback Linearization

According to Equations (15) and (16), CMUT dynamics can be linearized if the input voltage signal is scaled with the instantaneous gap together with subharmonic excitation without dc bias. Substituting the voltage acting on the transducer $V(t) = \alpha V_S(t)g(t)$, where α is a constant and $V_S(t)$ is the source voltage, yields

$$F_{ES}(t) = \frac{\varepsilon_0 \pi a^2 \alpha^2}{2} V_S^2(t), \tag{26}$$

so the nonlinear behavior due to gap dependence is compensated via nonlinear gap feedback [87]. The remaining nonlinear term $V_S^2(t)$ is handled by exciting the transducer at half the operating frequency as explained in Section 2.3.1. The nonlinear feedback topology is presented with the block diagram in Figure 26 where the CMUT subsystem is simply the CMUT model given in Figure 22.

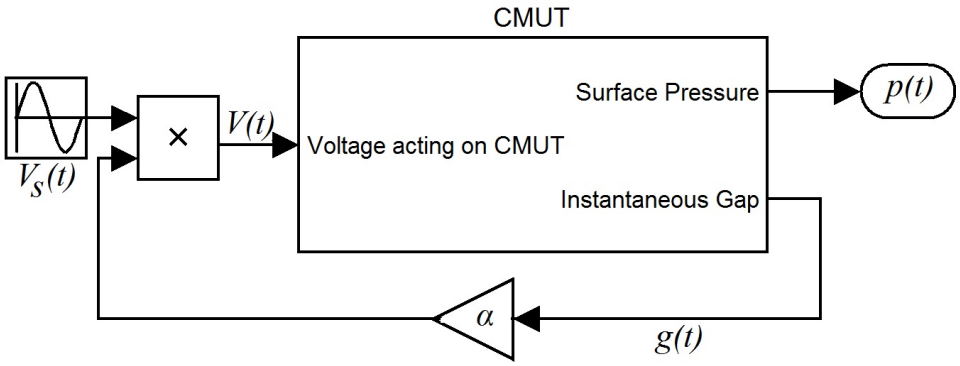

Figure 26: Block diagram of the nonlinear gap feedback topology

It is interesting to note that with $f_0/2$ excitation, nonlinear gap feedback generates a $3f_0/2$ component by distorting the input signal. The effect can be seen in Figure 27, where a 150 V, 10 MHz, 1 μs FWHM Gaussian enveloped tone burst is applied to the transducer with gap feedback and no dc bias. From the frequency domain perspective, the nonlinear

interaction of $f_0/2$ and $3f_0/2$ components in the distorted input signal generate two components at f_0 and $2f_0$ due to the nonlinear behavior of the transducer and the generated $2f_0$ component cancels the second harmonic generation. This observation suggests that the nonlinear compensation approach presented in [42] is indeed an attempt to implement gap feedback. Hence, the need for complex input signals and fine calibration of the added third harmonic signal in that approach can be avoided.

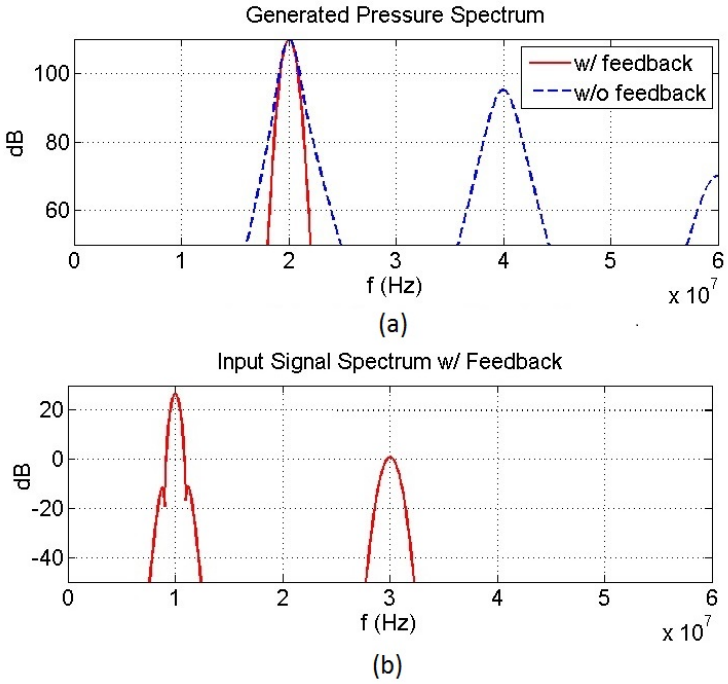

Figure 27: (a) Magnitude spectrum of generated surface pressure for 10 MHz, 150 V excitation signal with and without feedback with corresponding α for the same pressure amplitude at 20 MHz (b) The magnitude spectrum of the input voltage scaled with instantaneous gap, $V(t) = \alpha V_S(t)g(t)$

In essence, the proposed gap feedback method inherently implements charge control of the transducer, because in this case the charge on the CMUT capacitance is linearly proportional to the input voltage such that

$$Q(t) = \varepsilon_0 \pi a^2 \alpha V_S(t), \tag{27}$$

where α is the feedback gain. If the transducer is controlled with a charge driver instead of a voltage source, the electrostatic force acting on the CMUT membrane does not depend

on the instantaneous gap either [60]. However, charge control implementations in literature are limited to static operation, strictly dependent on the parasitic capacitances in the system and require complicated charge driving circuitry [88].

2.4.1 Approximate Gap Feedback via Nonlinear Voltage Division

A simple way of scaling the input voltage with instantaneous gap can be realized through the addition of a series, passive electronic component to the CMUT driving circuit as presented in Figure 28. With the addition of the series impedance, the voltage acting on the transducer becomes

$$V(t) = V_S(t)\frac{g(t)}{g(t) + j\omega Z_S \varepsilon_0 \pi a^2} \tag{28}$$

with harmonic excitation voltage $V_S(t) = V_S e^{j\omega t}$. If Z_S is a function of $g(t)$ such that the denominator of Equation (2.4.1.2) is constant,

$$Z_S(t) = \frac{K - g(t)}{j\omega\varepsilon_0\pi a^2}, \tag{29}$$

where K is a constant, the gap feedback can be implemented exactly. If $\left|j\omega Z_S \varepsilon_0 \pi a^2\right| \gg g(t)$ the voltage acting on the CMUT can be approximated as,

$$V(t) \approx V_S(t)\frac{g(t)}{j\omega Z_S \varepsilon_0 \pi a^2} \tag{30}$$

so the input voltage is scaled with instantaneous gap.

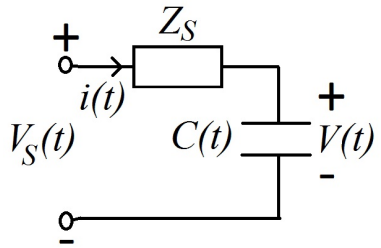

Figure 28: Resulting electrical circuit with the addition of series impedance to the CMUT capacitance

2.4.1.1 Capacitive Feedback

In an effort to extend the actuation range of parallel-plate electrostatic actuators, it was shown that a series capacitor extends the stable region of the CMUT in static operation through gap feedback [89]. With $Z_S = 1/j\omega C_S$ for harmonic excitation, the circuit in Figure 28 is a nonlinear voltage divider because the CMUT capacitance, $C(t)$, is a nonlinear function of the voltage across the transducer. The voltage across the CMUT becomes

$$V(t) = V_S(t)\frac{g(t)}{g(t) + \dfrac{\varepsilon_0 \pi a^2}{C_S}}. \tag{31}$$

As the input source voltage increases, the instantaneous CMUT gap tends to decrease, and this results in a decrease in $V(t)$. This negative feedback effect reduces the nonlinearity and thus stabilizes the transducer for a larger displacement range of the CMUT membrane. However, higher excitation voltages are required as a trade-off for the same membrane displacement because of the voltage division nature of the circuit [89]. The series capacitance value relative to the instantaneous CMUT capacitance determines the voltage division ratio and the harmonic generation. Equation 31 can be approximated as

$$V(t) \approx \begin{cases} V_S(t)\dfrac{g(t)C_S}{\varepsilon \pi a^2} & \text{if } C_S \ll C(t), \\ V_S(t) & \text{if } C_S \gg C(t). \end{cases} \tag{32}$$

The modified SIMULINK model incorporating the series capacitor is presented in Figure 29.

If the series feedback capacitor is designed such that its capacitance changes with CMUT membrane motion, satisfying the relation

$$C_S(t) = \frac{\varepsilon \pi a^2}{K - g(t)}, \tag{33}$$

then the gap feedback can be implemented ideally because the denominator of Equation (31) is constant. This indicates the possibility of an electromechanical device to be used as a variable feedback capacitor to approximate the gap scaling of the input voltage more accurately than the fixed series capacitor case.

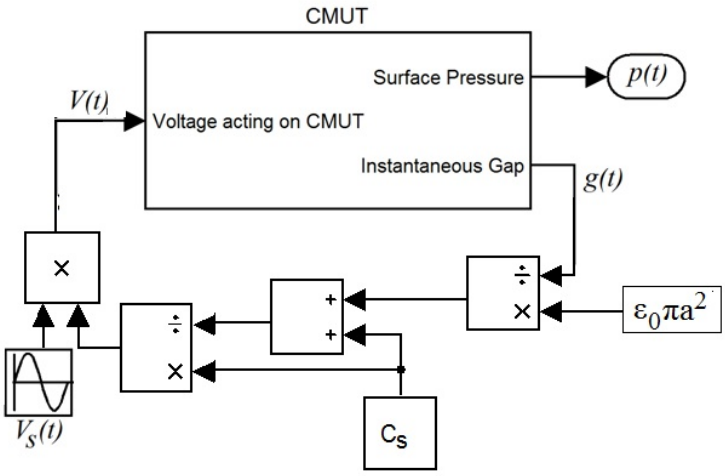

Figure 29: The SIMULINK model with addition of a series feedback capacitor

In Figure 30, the simulated voltage across the transducer normalized to the input voltage is plotted as a function of instantaneous normalized gap. As expected, the relationship between the drive signal and the instantaneous gap becomes more linear as the series capacitor gets smaller as compared to the CMUT capacitance. Figure 30(b) shows that for the same output pressure at the fundamental frequency, the harmonic ratio is improved with feedback. For decreasing C_S values, harmonic ratio improves at the expense of increased source voltage V_S. For the simulated parallel-plate CMUT, 10 dB reduction in the second harmonic component is achieved with $C_S = \varepsilon_0 \pi a^2 / g_0$ by doubling the excitation voltage to generate the same pressure output at the fundamental frequency, $f_0 = 20$ MHz.

2.4.1.2 Resistive Feedback

With a resistor used as the feedback component, $Z_S = R_S$, the circuit in Figure 28 is a nonlinear first-order low-pass filter where the output of the filter is the voltage acting on the CMUT, $V(t)$. Similar to the capacitive feedback case, the magnitude of the voltage across the transducer becomes linearized as a function of CMUT gap as the feedback resistor becomes larger. From the frequency domain perspective, the linearization performance improves as the cutoff frequency of the resulting low-pass filter gets smaller than the excitation frequency. The modified SIMULINK model incorporating the series resistor is

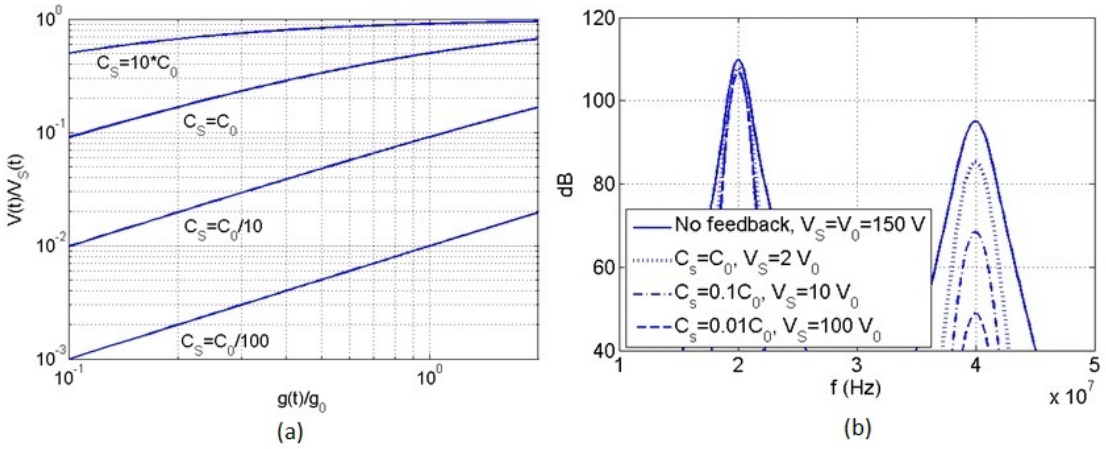

Figure 30: (a) Voltage acting on the transducer as a function of input voltage and instantaneous gap for different feedback capacitor values (b) 20- and 40-MHz components of the transmitted surface pressure for different series capacitor values and input signal amplitudes where the capacitive micromachined ultrasonic transducer is excited at 10 MHz

presented in Figure 31.

The simulation results for the resistive feedback case is given in Figure 32. Comparing the capacitive feedback results in Figure 30 and Figure 32, for the same fundamental and second harmonic pressure amplitudes, the required feedback resistor value can be calculated using the corresponding series capacitance value for the same input signal $V_S(t)$, such that $R_S = |1/j\omega C_S|$ where ω is the excitation frequency. Due to the low pass filter behavior of the circuit, the required feedback resistor value is inversely proportional to the excitation frequency for the same harmonic reduction. This is because the voltage division relation formulated in Equation is a function of frequency for resistive feedback, $Z_S = R_S$. In contrast, capacitive feedback is not dependent on frequency, where nonlinearity is only dependent on the relative value of the feedback capacitor compared to the CMUT capacitance.

2.4.1.3 Resistive-Inductive Feedback

The capacitive nature of the CMUT in the electrical domain can be exploited by connecting a series resistor and a series inductor to the transducer. The resulting circuit becomes a nonlinear second-order low-pass filter, and the resonant behavior of the resulting electrical

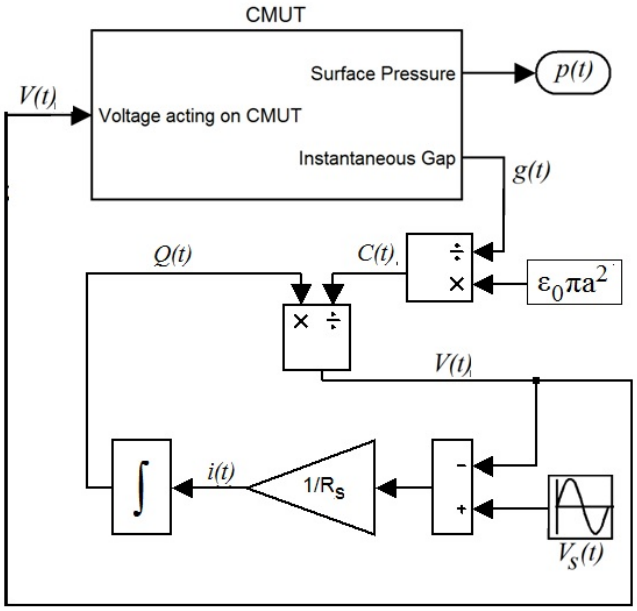

Figure 31: The SIMULINK model with addition of a series feedback resistor

circuit can be used to linearize the CMUT dynamics without the need for increased excitation voltage. A similar method involving a series tuning inductor to stabilize parallel-plate actuators was presented in [90]. With the addition of a series resistor-inductor pair, the differential equation governing the electrical domain of the transducer becomes

$$V_S(t) = R_S\, i(t) + L_S \frac{di(t)}{dt} + \frac{1}{C(t)} \int_0^t i(\tau) d\tau, \tag{34}$$

where the voltage across the transducer generating electrostatic force is

$$V(t) = \frac{1}{C(t)} \int_0^t i(\tau) d\tau. \tag{35}$$

The modified SIMULINK model incorporating the series inductor-resistor pair is presented in Figure 33.

For harmonic drive signal, the nonlinear relationship between $V_S(t)$ and $V(t)$ is

$$V(t) = V_S(t) \frac{g(t)}{g(t) + \left(j\omega R_S - \omega^2 L_S\right) \varepsilon_0 \pi a^2} \tag{36}$$

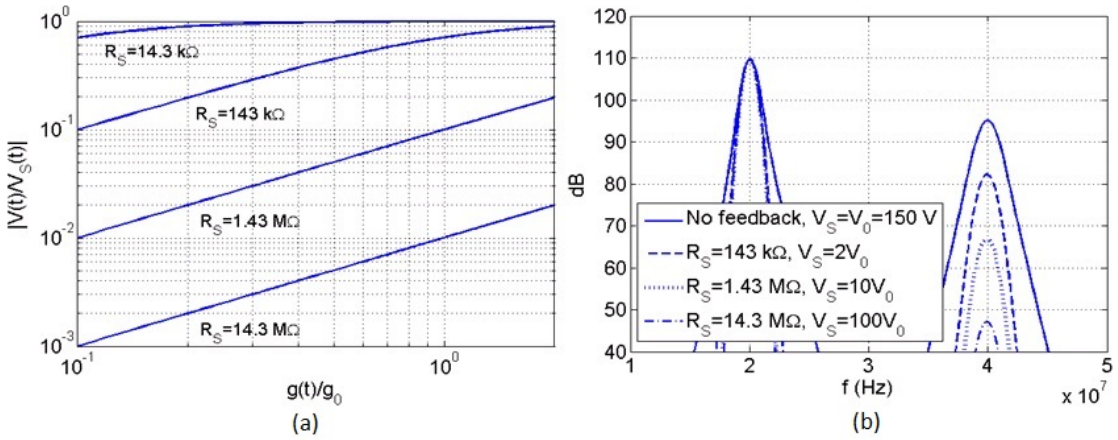

Figure 32: (a) Voltage acting on the transducer at 10 MHz as a function of input voltage and instantaneous gap for different feedback resistor values (b) 20- and 40-MHz components of the transmitted surface pressure for different series resistor values and input signal amplitudes where the capacitive micromachined ultrasonic transducer is excited at 10 MHz

where the damping ratio and the resonance frequency of the filter are

$$\omega_{filter} = \frac{1}{\sqrt{L_S C(t)}}, \qquad \xi = \frac{R_S}{2}\sqrt{\frac{C(t)}{L_S}}. \tag{37}$$

The series resistor and inductor values must be selected such that the relationship between $V(t)$ and $g(t)$ is linearized for $g(t)$ in the range from 0 to g_0. If the series inductor is chosen so that the resonance frequency of the circuit is higher than the excitation frequency the voltage acting on the transducer decreases with increasing gap, resulting in more nonlinear transducer behavior. This undesired phenomenon can be seen in the simulation results for the inductive-resistive feedback case given in Figure 34 (indicated by the solid line). where the voltage acting on the transducer reduces with increasing gap for most of the range. For the other cases in Figure 34 the constraint of $\omega_0 \ll \omega$, where ω is the excitation frequency, is satisfied for most of the desired gap range. With that approach the gap-CMUT voltage relationship can be optimized for harmonic distortion and excitation signal amplitude for a given output pressure at the fundamental frequency. The corresponding simulation results in the bottom graph of Figure 34 show that by using proper RL feedback, the second harmonic component of the generated pressure can be decreased by

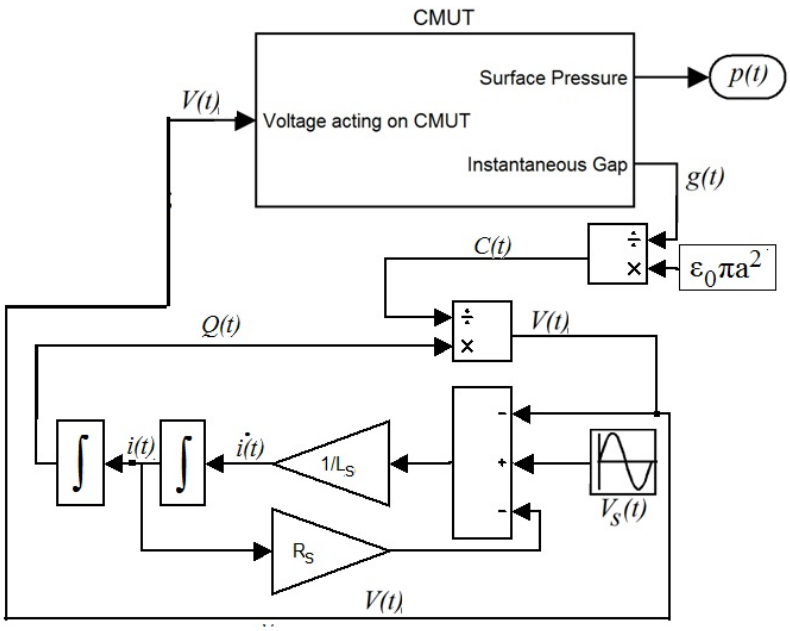

Figure 33: The SIMULINK model with addition of a series feedback resistor inductor pair

more than 20 dB without increasing the excitation signal. Moreover, due to the resonant behavior of the circuit, higher output pressure and lower harmonic distortion is achievable for a given excitation signal depending on the damping coefficient of the filter.

2.4.2 Discussion of the Simulation Results

Since the collapse phenomenon is related to the nonlinearity of the transducer, feedback linearization and charge control extends the stable displacement region of the CMUT. This has been previously shown for static operation in [87–89]. Here, it is essentially shown that similar techniques can be applied for dynamic operation with different feedback schemes. For example, Figure 35 plots the output pressure at the fundamental frequency as a function of ac voltage amplitude for one of the LR feedback cases. In comparison to Figure 25 which gives the same analysis for no feedback case, it is observed that not only the relationship between the excitation signal and pressure output at f_0 is linearized with gap feedback, but it is possible to increase the transmit sensitivity and the maximum pressure at the fundamental frequency of the transducer. It should be noted that with any of the series

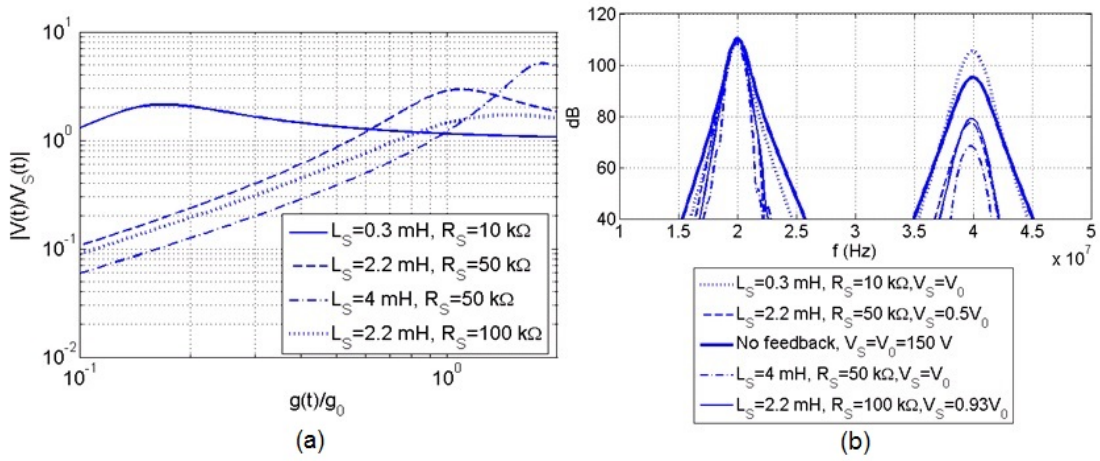

Figure 34: (a) Voltage acting on the transducer at 10 MHz as a function of input voltage and instantaneous gap for different feedback resistor and inductor values (b) 20- and 40-MHz components of the transmitted surface pressure for different series resistorinductor pair values and input signal amplitudes when the capacitive micromachined ultrasonic transducer is excited at 10 MHz

impedance methods the second harmonic levels can be reduced to more than 25 dB below the fundamental for a broadband device, making it suitable for harmonic imaging. This is achieved with either reasonably higher voltages in R and C feedback, or with reduced voltage levels with LR feedback, which maybe more difficult to implement in large arrays. Since the stable region of the transducer is extended with gap feedback linearization, the maximum pressure generated at the desired frequency can be increased without collapsing the membrane. Thus, linearization of the CMUT can be useful for high intensity applications like HIFU. The LR feedback case maybe more feasible for HIFU arrays where the channel count is small.

The method is also evaluated for broadband excitation waveforms which are typically used in harmonic imaging. The model is simulated for conventional operation with 2 cycle 20 MHz input signal, subharmonic excitation with and without resistive feedback. Note that for subharmonic excitation cases the input signal is 1 cycle 10 MHz tone burst to achieve similar bandwidth around 20 MHz. Simulation results for generated surface pressure are presented in Figure 36 in frequency and time domains. Conventional and subharmonic only excitations result in highly distorted pressure waveforms. With resistive feedback,

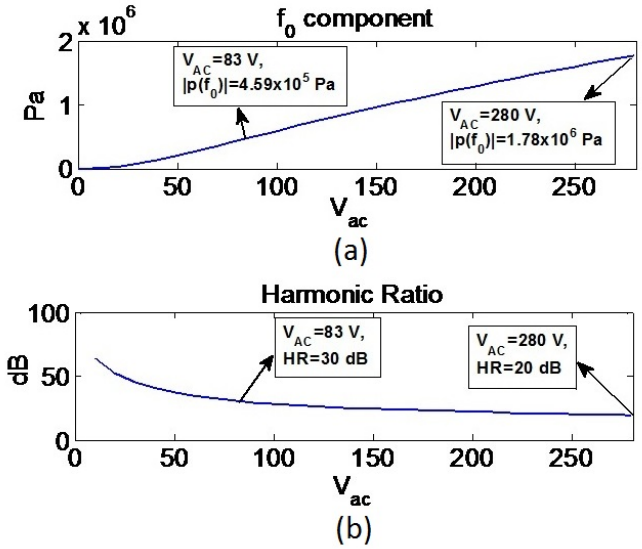

Figure 35: (a) Magnitude of the f_0=20 MHz component of the generated average surface pressure as a function of input signal amplitude at 10 MHz without dc bias with series resistor-inductor pair with values of R_S=50 kΩ and L_S=2.2 mH (b) Ratio of the magnitudes of 20 MHz and 40 MHz components of the generated pressure as a function of input signal amplitude

~10 dB reduction in second harmonic is achieved, where higher order harmonics are also suppressed more effectively. The results show that gap feedback method can be applied to broadband imaging signals as well as narrowband inputs.

An important aspect of the proposed method is that it does not require any changes in the mechanical CMUT design to limit the frequency bandwidth. For applications like harmonic imaging, the gap feedback circuit will be used only for transmission with reduced harmonics so that the bandwidth in receive mode is not affected. Since CMUT design is independent from the linearization method, any generic CMUT can be linearized with the gap feedback method.

A possible implementation of the proposed method in array format would be based on the dual-electrode CMUT structure presented in [76] where the transmit and receive electrodes embedded in the transducer membrane are electrically isolated. With the dual-electrode structure, the same element can be used for harmonic imaging by utilizing gap feedback in the transmit path with subharmonic excitation and with no DC bias without

any detrimental effect on the separately biased receiver electrode and receiver electronics, or the receiver bandwidth.

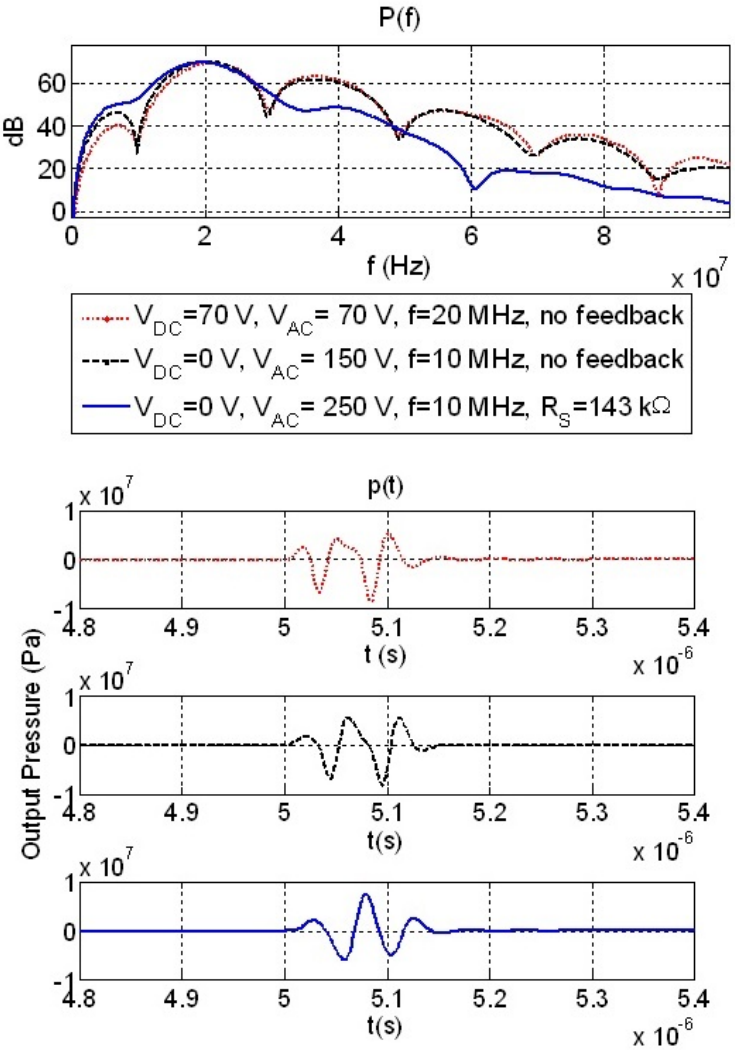

Figure 36: Spectra of the generated surface pressure for broadband excitation waveforms for conventional and subharmonic excitation cases with and without feedback and the their corresponding time domain signals

2.4.3 Experimental Results

Initial experiments demonstrating the presented gap feedback method were conducted. A CMUT with low collapse voltage and low center frequency were chosen for the experiments so that the nonlinearities related to the driver amplifier were minimized at its output up to the collapse voltage of the CMUT where the response gets highly nonlinear. Therefore the whole range of voltage values were explored while the major source of nonlinearity in the measurements was the CMUT behavior, as desired. A CMUT with center frequency of 3 MHz, 133% (1 to 5 MHz) effective fractional bandwidth, and a static collapse voltage of 24 V were used in the experiments. Figure 37 presents the measured pulse echo response of the CMUT and its spectrum when excited with a short pulse. A pair of these transducers is used in a pitchcatch configuration for harmonic distortion measurements. The receiver is biased to 22 V, close to collapse, for high receive sensitivity. Figure 38 gives the received pressure spectrum when the transmitting CMUT is excited by a 24-Vpeak, 1.5-MHz, 15-cycle toneburst for the case without feedback, i.e., direct connection to the amplifier. Note that the excitation is large signal ac at half the desired frequency of 3 MHz with no dc bias. In this case, the harmonic signal at 6 MHz is 15 dB below the desired 3 MHz output.

For gap feedback operation, the series resistor approach was used. First, the capacitance of the transducer is measured with a network analyzer; it is approximately 120 pF and an appropriate resistor, 1 k in this case, is connected in series with the amplifier. This sets up a low-pass filter with a cut-off frequency of 1.5 MHz. With this configuration, where only the transmitter input circuitry is changed, the same output pressure at 3 MHz is received with a 40 V peak ac signal at 1.5 MHz, but the harmonic component at 6 MHz is reduced more than 10 dB as shown by dashed lines in Figure 38. This simple experiment effectively demonstrates that a simple gap feedback implementation significantly reduces the harmonic generation of a broadband CMUT with a moderate increase in the applied ac signal level.

For evaluation of the inductive gap feedback, the CMUT element shown in Figure 39 was utilized. The transducer is immersed in vegetable oil, and the radiated pressure signal

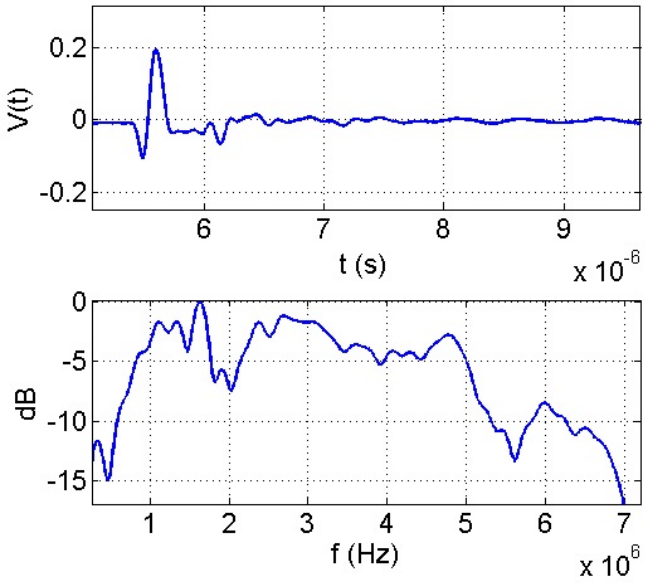

Figure 37: Pulse-echo response of the CMUT used in the experiment and its frequency spectrum

due to the displacement of the membranes in response to an excitation signal is measured using a broadband hydrophone. The frequency response of the CMUT element operating in the 5-15MHz range is also given in Figure 39. The transducer is excited subharmonically at $f_0/2$=3.6 MHz without feedback, with resistive feedback and with inductive feedback using proper electrical component values, and all cases are compared in terms of their spectral content in Figure 40. Approximately 10 dB decrease in the second harmonic of the transmitted pressure signal is achieved for both feedback cases with increased input signal with resistive feedback while the drive signal amplitude is kept constant for the inductive feedback case.

2.5 Summary and Conclusion

A simple one-dimensional transient model is used to investigate the dependency of the non-linear CMUT behavior on the dc and ac components of excitation signal. It is shown that subharmonic excitation of CMUTs without dc bias is of limited use for harmonic distortion

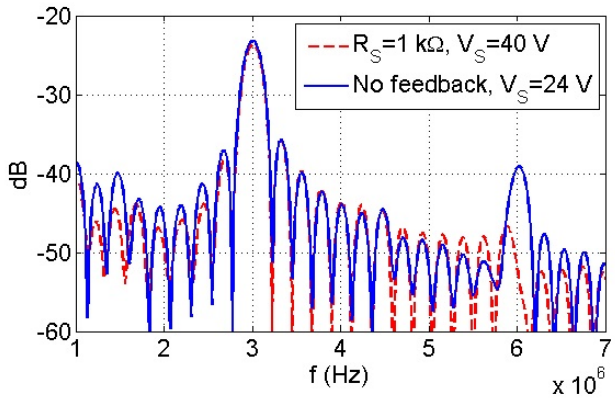

Figure 38: Frequency spectrum of the received signal with and without resistive feedback where the transducer is excited with a 15 cycle 1.5 MHz tone burst

reduction for large displacement amplitudes. Different gap feedback schemes were investigated to reduce harmonic distortion of the CMUT membrane motion and the relationship of the proposed method with linearization methods in the literature were investigated . As a summary, the series feedback capacitor improves the harmonic ratio where the operation of the resulting circuit is independent of the frequency and the maximum pressure that can be generated at the fundamental frequency without collapsing the CMUT membrane is increased at the expense of input voltage. It is shown that series resistance utilizing resistive feedback improves the harmonic ratio where the resulting circuit is a first-order low-pass filter. The maximum pressure that can be generated, with a trade-off of increased input voltage amplitude similar to the capacitive feedback case, is also improved. A series resistor-inductor pair results in second-order filter response. With appropriately selected values in this topology, one may achieve the same pressure at the fundamental frequency with lower input voltage. As in the cases of other feedback configurations, one can also increase the maximum output pressure at the fundamental frequency. The simulations also suggest that the method can be used for broadband excitation signals used for imaging applications. Initial experiments were conducted and the results support the calculations. Approximately 10 dB improvement in the harmonic ratio is achieved over subharmonic ac-only excitation by adding a simple series resistor to a CMUT and increasing the input

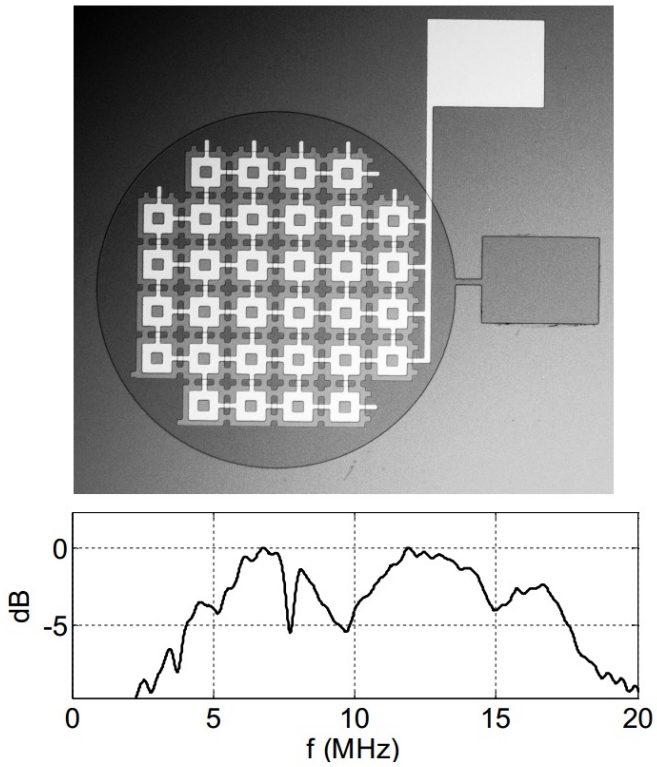

Figure 39: CMUT element composed of 32 individual 70 μm $\times$ 70μm membranes connected in parallel and the normalized frequency response of the transducer measured by a broadband hydrophone immersed in vegetable oil

voltage level, while keeping the magnitude of the fundamental component of the transmitted pressure constant.

The proposed gap feedback linearization method was developed using a nonlinear parallel plate model for a single CMUT membrane. Although this model captures the CMUT nonlinearity to some extent, the model neglects the additional nonlinearities due to membrane curvature. The electrostatic force distribution on a membrane changes due to the membrane curvature as the device goes through large displacements. Therefore membrane based CMUTs deviate from parallel plate operation for large displacements and the performance of the proposed linearization method degrades since the uniform electrostatic force assumption in the parallel plate model does not hold. Additionally, as the proposed method is based on sensing the change in the CMUT capacitance as a measure of instantaneous gap, parasitic capacitances also affect the gap feedback operation. Therefore for careful

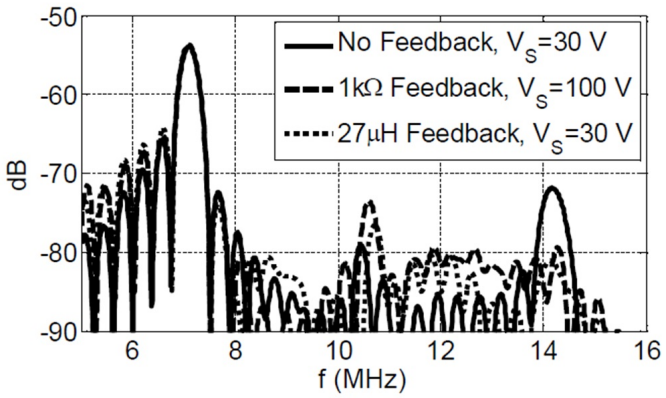

Figure 40: Spectral content of the transmitted ultrasound wave measured by a hydrophone when the transducer is excited with a 10 cycle 3.6 MHz tone burst without feedback and with different feedback topologies

modeling and implementation of the proposed method, accurate large signal modeling of membrane based CMUTs in array operation is crucial. A nonlinear numerical model with such capabilities is presented in Chapter 3.

CHAPTER 3

LUMPED LARGE-SIGNAL MODELING OF CMUT ARRAYS IN TRANSMIT MODE

In this chapter a computationally efficient, MATLAB based transient model capable of large signal analysis of CMUT arrays with arbitrary array/membrane geometries and electrical termination conditions is presented. The model is based on separation of the linear structural acoustics problem and the nonlinear electrostatic force calculation. A similar approach was taken in [74] where the nonlinear CMUT behavior was described by a nonlinear electrostatic transformer and a linear mass-spring-damper system for a single CMUT membrane which neglects higher order membrane shapes. By exploiting this separability, the solution of the distributed complex linear acoustic behavior of an array can be incorporated into a reduced order lumped nonlinear model.

3.1 Model Overview

The model presented in this chapter can be divided into three main sections, as described by the three blocks in Figure 41, with voltage input and pressure output as indicated. In block A, the drive signal vector, $\mathbf{V}(t)$, contains the applied voltages for each of the CMUT electrodes as a function of time. The voltage inputs of block A and the average electrode displacements are used to calculate the total electrostatic forces iteratively for each electrode in the array. This block accounts for sources of nonlinearity in large-signal CMUT modeling, where stress stiffening effects are neglected because the vacuum gaps are much smaller than the lateral dimensions and the induced strain will be small even under full deflection [91]. The sources of the nonlinearity in CMUT operation are the voltage square and inverse gap square dependence of the electrostatic force acting on the electrodes, as discussed in Section 2.3, and the change in force distribution on the electrodes as the CMUT membrane deflects. To capture the nonlinearity resulting from the change of electrostatic

force distribution on the CMUT electrode, the electrode may be divided into patches and modeled as separate electrodes, depending on the electrode size. This incorporates higher order modes of the membrane in electrostatic force calculation, which increases the model accuracy significantly. The method of electrode separation into patches will be explained in detail in Section 3.3.1.

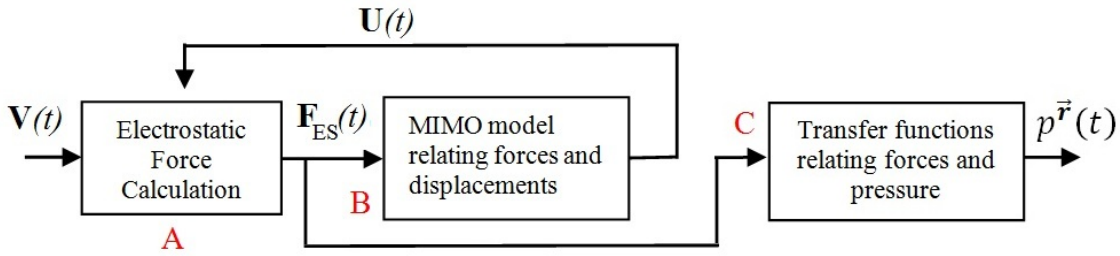

Figure 41: Block diagram describing the transient model.

Block B describes the vibroacoustic behavior of the array as a linear MIMO system relating the total electrostatic forces acting on each electrode patch and their respective average displacements. This block is derived from the linear acoustic analysis of the CMUT array using the boundary element method presented in [70]. Using the BEM, nodal displacements are calculated as a function of frequency for multiple cases where each electrode patch in the array is excited individually with unit pressure applied to the patch. As the mechanical dynamics of the CMUT array are linear, the superposition of the individual solutions can be used for the solution of arbitrary excitation configurations. To reduce the order of the distributed model, the nodal frequency response data are lumped into frequency domain relationships that are taken from total forces acting on electrode patches to the average displacement of each patch. The calculated relations are analogous to self and mutual mechanical impedances of electrode patches, where the variables would be patch velocities and total forces acting on them. A MIMO finite impulse response (FIR) filter is then described by using the calculated frequency response data to obtain a time-domain solution. As the linear acoustic problem is solved via BEM, a MIMO FIR filter block is constructed which relates the total forces acting on each electrode patch and their mean

displacements.

This linear MIMO model block couples the dynamics of individual electrode patches through acoustic interaction, and therefore it models the linear mechanical behavior of the array, including acoustic crosstalk and higher order membrane shapes. Fluid coupling is considered to be the only source of crosstalk; the mechanical coupling between CMUT membranes through the substrate is neglected. Electrostatic force (block A) and membrane displacement (block B) calculations completely define the electromechanical behavior of the modeled CMUT array. The solution of the transient model is then used to calculate the time-domain pressure signal at an arbitrary point of interest. Block C can be considered a multi-input single-output (MISO) system in which the block inputs are the total electrostatic forces acting on array electrode patches, and the output is the pressure at the desired point in the immersion fluid. As the electrostatic forces acting on electrode patches are obtained with the transient simulation in SIMULINK, the time-domain pressure signal at point $\vec{\mathbf{r}}$ can be calculated as

$$p^{\vec{\mathbf{r}}}(t) = \mathcal{F}^{-1}\left\{ \begin{bmatrix} P_1^{\vec{\mathbf{r}}}(\omega) & P_2^{\vec{\mathbf{r}}}(\omega) & \dots & P_M^{\vec{\mathbf{r}}}(\omega) \end{bmatrix} \begin{bmatrix} \mathcal{F}\{F_1(t)\} \\ \mathcal{F}\{F_2(t)\} \\ \vdots \\ \mathcal{F}\{F_M(t)\} \end{bmatrix} \right\}, \tag{38}$$

where $P_m^{\vec{\mathbf{r}}}(\omega)$is the frequency domain relationship relating the total electrostatic force acting on the m^{th} patch and the pressure at point $\vec{\mathbf{r}}$ and $\mathcal{F}\{F_m(t)\}$ is the Fourier transform of the electrostatic force acting on m^{th} patch calculated the input voltage vector $\mathbf{V}(t)$.

3.2 Boundary Element Modeling of Vibroacoustic CMUT Dynamics

The blocks in Figure 41 that describe the vibroacoustic behavior are derived using the computationally efficient boundary element method. BEM has been previously introduced to simulate the linear vibroacoustic CMUT array dynamics in fluidic environments [70]. In this method, the vibrating array surface is meshed and the force balance is solved for each node, reducing the distributed CMUT array behavior to an N degree of freedom vibration

problem, where N is the total number of nodes in the array mesh. For simulation accuracy, N should be selected such that every node can be considered as a baffled acoustic point source with uniform radiation pattern for the frequency range of interest, and mesh convergence is satisfied for stiffness matrix, $\mathbf{K}$, calculation [92]. An example membrane discretized into a 5×5 grid is shown in Figure 42 with a $dx \times dy$ nodal area. The force balance equation for each node i can be expressed as

$$p_{app,i} = m\ddot{u}_i + \mathbf{k}_i\mathbf{u} + \sum_{n=1}^{N} \frac{\rho_0 S\, \ddot{u}_n(t - r_{n,i}/c)}{2\pi r_{n,i}} \beta(r_{n,i}, u_n). \tag{39}$$

Here, the external mechanical pressure applied on node i, $p_{app,i}$, is balanced by the membrane reaction forces and fluid loading, where u_i is the displacement of the i^{th} node and $\mathbf{u} = \begin{bmatrix} u_1 & u_2 & \dots & u_N \end{bmatrix}^T$ is the displacement vector of all nodes in the array mesh. The first term in right-hand side of Equation (39) is the inertia of the node i with local mass density m, which is membrane density $\times$ thickness. The second term is the stiffness, which is in vector form as $\mathbf{k}_i = \begin{bmatrix} k_{1,i} & k_{2,i} & \dots & k_{N,i} \end{bmatrix}$. For cases in which analytical solutions can be obtained, such as Timoshenko's thin plate equation, $\mathbf{k}_i$ can be calculated numerically using the finite difference (FD) approximation of these solutions for the meshed membrane [70, 71, 93]. The last term in Equation (39) is the fluid-loading term, which makes use of the Greens function of a baffled point source. The term is the sum of the pressure contributions acting on node i from the displacement of each node in the array mesh where ρ_0 and c are the density and speed of sound in the immersion fluid, respectively, S is the nodal area, $dx \times dy$, $r_{n,i}$ is the distance between node i and node n, and $\beta(r_{n,i}, u_n)$ is the attenuation in the immersion fluid.

Equation (39) defines a unique equation for each node in the array mesh and results in N coupled equations which can be represented in matrix form. Considering harmonic excitation at frequency ω, the vibroacoustic response of the array is described in frequency domain as a system of linear equations

$$\mathbf{u}(\omega) = \mathbf{G}^{-1}(\omega)\mathbf{p}_{app}. \tag{40}$$

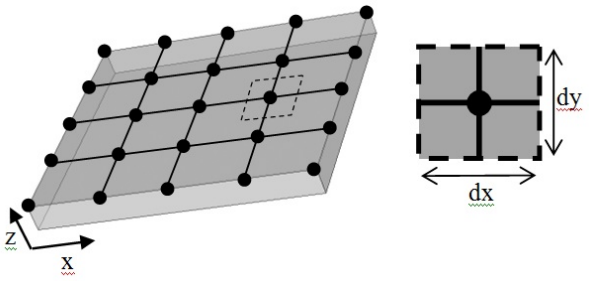

Figure 42: CMUT membrane divided into 5×5 matrix of nodes, $N = 25$, with corresponding areas $dx \times dy$.

Here, $\mathbf{p}_{app}$ is the vector comprised of external pressures acting on array nodes and $\mathbf{u}(\omega)$ is the nodal displacement vector. $\mathbf{G}(\omega)$ is the force balance matrix, which is calculated using the stiffness, $\mathbf{K}$, mass, $\mathbf{M}$, and the mutual impedance, $\mathbf{Z}_r(\omega)$, matrices such that

$$\mathbf{G}(\omega) = \mathbf{K} - \omega^2\mathbf{M} + j\omega\mathbf{Z}_r(\omega). \tag{41}$$

As the force balance matrix $\mathbf{G}(\omega)$ is calculated, Equation (40) can be solved for nodal displacements when the array is excited with the harmonic load distribution, $\mathbf{p}_{app}e^{j\omega t}$. Derivations of the stiffness, mass and fluid coupling matrices in Equation (41) are given in the next subsections.

3.2.1 Stiffness Matrix Calculation for Thin CMUT Membranes

The stiffness matrix in Equation (41), $\mathbf{K}$, describes how the normal static force acting on a given element area influences the displacement of the entire membrane surface. For static loading of the membrane, assuming that the lateral dimensions are much larger than the thickness, the stiffness can be approximated by the thin plate equation

$$P(x, y) = \frac{\partial^2 M_x}{\partial x^2} + \frac{\partial^2 M_y}{\partial x^y} + \frac{\partial^2 M_{xy}}{\partial x \partial y}, \tag{42}$$

where $P(x, y)$ is the distribution of pressure acting on the CMUT membrane [71, 93]. This is given as the flexural plate operator where M_x, M_y, and M_{xy} are the bending moments on

an element volume of the membrane such that

$$\begin{aligned} M_x &= D\left(\frac{d^2u}{dx^2} + \nu\frac{d^2u}{dy^2}\right), \\ M_y &= D\left(\nu\frac{d^2u}{dx^2} + \frac{d^2u}{dy^2}\right), \\ M_{xy} &= D(1-\nu)\frac{d^2u}{dxdy}, \end{aligned} \tag{43}$$

where ν is the Poisson's ratio, D is the flexural rigidity of the membrane

$$D = \frac{Eh^3}{12(1-\nu^2)}, \tag{44}$$

E is the Young's modulus and h is the membrane thickness.

For the case of static loading, Equation (42) can be written in matrix form for a meshed membrane such that

$$\mathbf{p}_{app} = \mathbf{K}\mathbf{u}, \tag{45}$$

where $\mathbf{p}_{app}$ and $\mathbf{u}$, are the pressure and displacement vectors of the surface nodes, respectively, and $\mathbf{K}$ is the stiffness matrix describing the reaction stresses in an elemental area of the plate

$$\mathbf{K} = \begin{bmatrix} k_{1,1} & k_{2,1} & \dots & k_{N,1} \\ k_{1,2} & k_{2,2} & \dots & k_{N,2} \\ \vdots & \vdots & \ddots & \vdots \\ k_{1,N} & k_{2,N} & \dots & k_{N,N} \end{bmatrix}. \tag{46}$$

The unique $\mathbf{K}$ expression for the force balance is generated through finite difference (FD) approximations to estimate the derivatives used to describe the bending moments in Equation (42). Displacement of each node is a linear function of the nodal displacement values from surrounding nodes and the distance between nodes, resulting in a system of N force balance equations. Therefore in matrix form, the membrane stiffness can be described as an $N \times N$ matrix. The fixed boundary conditions sets nodal displacements at the membrane edges to zero. The stiffness matrix generated using this approach is a sparse matrix containing information that relates one node and its immediate surrounding nodes.

3.2.2 Stiffness Matrix Calculation for Arbitrary Membrane Geometries

The thin plate equations used to generate the **K** matrix above inherently limit the numerical modeling capabilities of the BEM approach. For high frequency applications beyond 40 MHz, CMUT arrays comprised of membranes 18 μm wide and 3 μm thick have been fabricated and tested, but are not accurately described by the thin plate equations [94].

As an alternative, static FEA can be used to generate an equivalent stiffness matrix, **K** for an arbitrary membrane geometry. For this purpose, FEA is implemented using the same nodal locations associated with the BEM mesh. For each finite area centered on each node of the 2D membrane surface, a uniform pressure of 1 Pa is applied, and the resulting displacement for each nodal location is calculated. Each FEA simulation produces displacement information over the entire membrane where $u^{i,j}$ is the displacement of node j when unit pressure is applied to node i. With all N FEA simulations, the displacement matrix is fully populated, and the stiffness matrix can be calculated as:

$$\mathbf{K} = \begin{bmatrix} u^{1,1} & u^{2,1} & \dots & u^{N,1} \\ u^{1,2} & u^{2,2} & \dots & u^{N,2} \\ \vdots & \vdots & \ddots & \vdots \\ u^{1,N} & u^{2,N} & \dots & u^{N,N} \end{bmatrix}^{-1} \tag{47}$$

With this approach thin plate approximations are removed, realistic edge boundary conditions can be applied, and complex geometries can be evaluated. Also, for a given geometry and mesh density, the FEA need only be performed once as it can be reused for an array of the same membranes. The resulting **K** matrix is directly included in the BEM formulation for linear CMUT dynamics.

3.2.3 Calculation of Mass and Fluid Coupling Matrices

The mass matrix, **M**, is a diagonal $N \times N$ matrix consisting of the local surface density and thickness at each node. For an array with arbitrary membrane geometries, the mass matrix

is

$$\mathbf{M} = \begin{bmatrix} \rho_1 h_1 & 0 & \dots & 0 \\ 0 & \rho_2 h_2 & \dots & 0 \\ \vdots & \vdots & \ddots & \vdots \\ 0 & 0 & \dots & \rho_N h_N \end{bmatrix}. \tag{48}$$

where ρ_n and h_n are the local density and membrane thickness at node n, respectively.

The last matrix in Equation (41) is the fluid coupling matrix which couples the nodal displacements through acoustic propagation. The fluid loading on node i resulting from the displacement of node n can be expressed as $j\omega Z_r^{i,n}(\omega)u_n$, where

$$Z_r^{i,n}(\omega) = \frac{j\rho_0 \omega S}{2\pi} \frac{e^{-jkr_{i,n}}}{r_{i,n}} 10^{-\alpha(\omega) r_{i,n}/20}, \tag{49}$$

k is the wavenumber, $\alpha(\omega)$ is the attenuation coefficient as a function of frequency in decibels per meter, and $r_{i,n}$ is the distance between node i and node n. This formulation is based on the Green's function of a baffled point radiator in a semi-infinite fluid. It assumes that the mesh is fine enough that the normal velocity is uniform over the nodal area and the node can be considered as a point source in the frequency range of interest. Because the Green's function accounts for the radiation boundary conditions of the acoustics problem, the fluid is not meshed in the BEM, which allows for the significant reduction in computational time as compared with FEA [70]. The formulated fluid coupling is included in the force balance matrix as

$$\mathbf{Z}_r(\omega) = \begin{bmatrix} Z_r^{1,1} & Z_r^{2,1} & \dots & Z_r^{N,1} \\ Z_r^{1,2} & Z_r^{2,2} & \dots & Z_r^{N,2} \\ \vdots & \vdots & \ddots & \vdots \\ Z_r^{1,N} & Z_r^{2,N} & \dots & Z_r^{N,N} \end{bmatrix}. \tag{50}$$

For diagonal elements in (50), where $r_{i,i} = 0$, the node is modeled as an infinitesimally small circular piston with an effective radius, $a_{eff} = \sqrt{S/\pi}$, such that

$$Z_r^{i,i}(\omega) = \rho_0 c \left[\frac{1}{2}(ka_{eff})^2 + j\frac{8}{3\pi}(ka_{eff}) \right]. \tag{51}$$

It should be noted that the fluid coupling matrix $\mathbf{Z}_r(\omega)$ is symmetric, such that $Z_r^{i,n} = Z_r^{n,i}$.

3.2.4 Verification of the Linear Vibroacoustic Model

Verification of this linear acoustic model was performed experimentally using CMUT arrays with $35 \times 35\mu$m, 2-μm-thick membranes [56]. The small-signal thermal-mechanical noise of the test array under applied dc bias was measured and was compared with the FD-BEM simulations, showing good agreement. In [56], CMUT array behavior was linearized around the operation point corresponding to the applied dc bias value, including a spring softening effect in the simulations.

To validate the stiffness matrix calculations and indicate the limitations of the thin plate approximation, simulations in vacuum were performed in COMSOL to calculate the first eigenfrequency of a CMUT membrane. The results were compared with both the numerical method with the stiffness matrix based on thin plate approximations given in Section 3.2.1 and the FEM based method presented in Section 3.2.2. The membrane material properties used in simulations are given in Table 2.

Table 2: Material Properties Used in Simulations

Property	SiN_x	Al
Density	2040 kg/m^3	2700 kg/m^3
Poisson's ratio	0.22	0.35
Young's modulus	110 GPa	70 GPa

The FEA mesh convergence was verified for all simulations. The square CMUT membrane thickness was fixed at 2 μm with electrode coverage dimensions set to 75% of the edge dimensions which were adjusted from 40 μm to 10 μm, aspect ratios 20 to 5. These dimensions were chosen to be consistent with CMUT membranes previously fabricated for ultrasonic imaging applications [39, 53, 56, 66, 67, 76, 94]. Table 3 shows that the hybrid method and FEA simulations are in good agreement for all aspect ratios, deviating by less than 1.5% for 2 μm nodal meshing in the BEM domain. The element sizes for simulations were chosen based on convergence criteria of less than 5%. With the low aspect ratio of 5, the thin plate approximation deviates by 25% from FEA, whereas the presented FEA based

hybrid method deviates by less than 2%, as seen in Table 3.

Table 3: Calculated First Eigenfrequencies in Vacuum

Aspect Ratio	FEM	Hybrid Method	FD-Thin Plate Equation
20	15 MHz	15 MHz	15 MHz
15	27 MHz	27 MHz	27 MHz
10	57 MHz	58 MHz	59 MHz
5	190 MHz	193 MHz	237 MHz

To further validate the hybrid method, a single mass loaded membrane, shown in Figure 43, with a buried electrode was simulated in water with the material properties listed in Table 2. The frequency response using the hybrid method was compared with FEA utilizing symmetry in a quarter-sphere with an outer matched layer which models an infinite fluidic space. Figure 44, shows the FEA results with 1 MHz resolution from 20 to 70 MHz, along with the hybrid method, using 1 MHz resolution from 5 to 80 MHz, showing excellent agreement in center frequency and bandwidth, with 0.2 MHz difference in center frequency. It can also be seen that the FEA above 45 MHz shows oscillations, which is a known issue with insufficient fluid meshing density at higher frequencies.

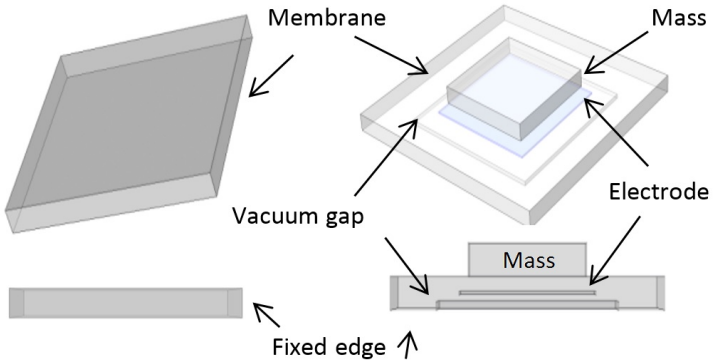

Figure 43: Simple square membrane with fixed edge and membrane with mass loading, metal electrode, and variable fixed boundary

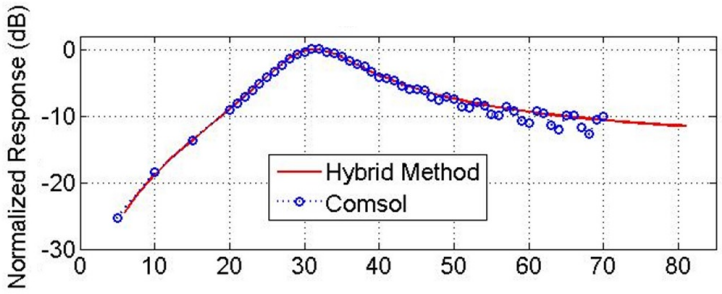

Figure 44: Comparison of hybrid method to FEA using Comsol for a single mass loaded CMUT

3.3 Lumped Large-Signal Array Model

With the linear vibroacoustics solution obtained for membrane arrays with arbitrary geometry, the next step is the transient simulation of the forced response of the array driven by large drive signals. To incorporate nonlinear electrostatic signals in the analysis, the SIMULINK model shown in Figure 45 was developed. The model takes the electrical drive signals of each transmit electrode patch as the input vector $\mathbf{V}(t)$, and outputs the electrostatic forces acting on each patch as vector $\mathbf{F}(t)$ as a function of time. It should be noted that every signal in the model is multiplexed and carries separate time-domain signals for each electrode patch. The force vector $\mathbf{F}(t)$ is then postprocessed for calculation of time-domain pressure at an arbitrary point in the immersion field. In the model, the MIMO FIR filter block represents the linear vibroacoustic response of the CMUT array suitable for time-domain solution, which is block B in Figure 41. The nonlinear electrostatic force calculation block is implemented via a look-up table providing the relationship between the mean gap under the CMUT electrode patch and the normalized total electrostatic force acting on it. The details of the block diagram are explained in the next subsections.

3.3.1 Reduced Order Lumped Model Approximation for Electrostatic Force Calculation

Because the ratio of lateral dimensions to the gap is large in most CMUTs, the total electrostatic force acting on a membrane electrode can be approximated by the parallel-plate model given in Section 2.2. However the parallel-plate equation which assumes uniform

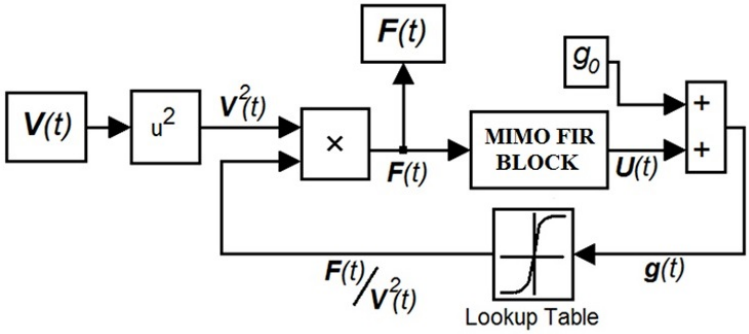

Figure 45: Simulink block diagram with the input vector of voltage signals applied to array electrode patches. The output vector $F(t)$ is the time domain electrostatic forces acting on the electrode patches, which is post-processed for pressure calculation.

charge distribution within the CMUT electrode does not hold for large displacements. As the membrane deflects, the charge and force distribution on the membrane also changes because of the local gap variation over the CMUT electrode. Therefore, the parallel plate approximation fails and the relationship between the mean gap and the total electrostatic force becomes a more complex function for a deflected membrane which must be dealt with separately.

A straightforward approach consistent with the BEM analysis would be to model each BEM nodal area under the electrode as a separate parallel-plate device that is mechanically coupled to the rest of the structure, but this would result in a large system of equations. To reduce the size of the problem while still maintaining accuracy, the membrane electrode is modeled with multiple electrode patches with coupled dynamics accounting for the variable electrostatic force distribution on the membrane. The patch shapes and locations are chosen by separating the electrode into multiple displacement regions based on the modal analysis of the membrane. For example, for a square CMUT membrane, as shown in Figure 46, with a central electrode, only the symmetric modes of the membrane are excited with electrostatic excitation. Although the first mode of the membrane is dominant in the motion, higher order symmetric modes are also excited. Especially when the membrane undergoes large displacements while the electrostatic input voltage is applied, the force distribution on the electrode changes and the electrostatic forces are more localized at the

center of the electrode because of gap dependence of the force. This localized force can excite the second symmetrical mode of the membrane (fifth mode in Figure 46) which has a resonance frequency of ~3.6 times the first mode, covering the useful frequency range for most CMUT applications.

For this particular geometry, which can represent a large group of CMUT devices with circular and hexagonal membranes, it has been observed that two electrode patches placed on the out-of-phase regions of the second symmetric mode result in an accurate prediction of the nonlinear behavior with full gap swing. The patch shape selection is automated and can be done efficiently. The mode shapes, and therefore the electrode patch shapes, of a single membrane are calculated as the eigenvectors of the matrix $\mathbf{M}^{-1}\mathbf{K}$, where the mass matrix, $\mathbf{M}$, and the stiffness matrix, $\mathbf{K}$, are already calculated for the BEM formulation [95]. The mode shapes and the resulting two electrode patches for the 40 μm wide, 2 μm thick square membrane with full electrode coverage are also given in Figure 46.

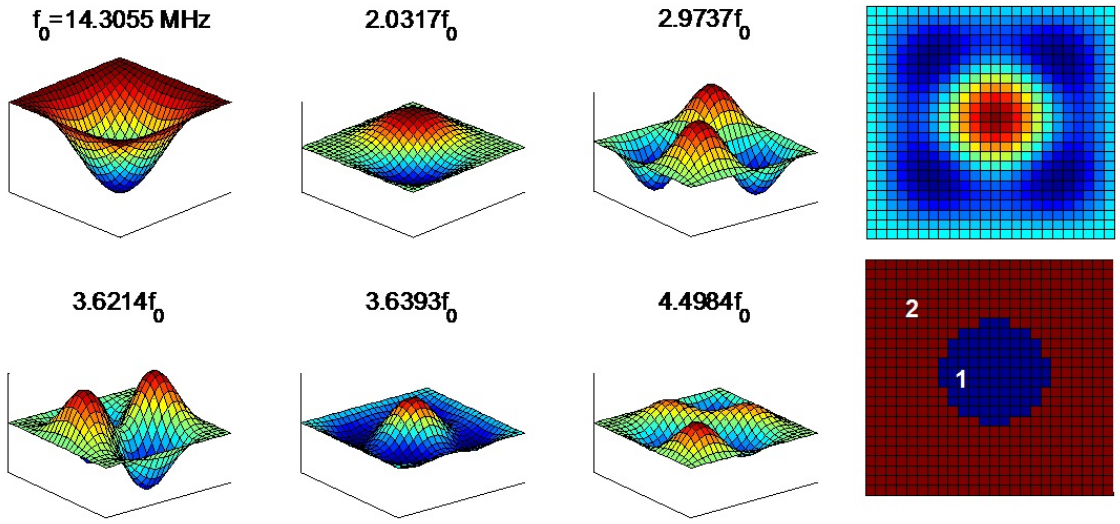

Figure 46: First 6 modes of modeled membrane, calculated as the eigenvectors of the matrix $\mathbf{M}^{-1}\mathbf{K}$. The membrane is SiN_X, 2 μm thick, The actuation electrode separated to 2 patches using the out of phase displacement regions of fifth membrane mode.

For increased accuracy, the CMUT electrode can be modeled with an increased number of patches considering higher order modes; however, the trade-off is a larger system with

an increased number of inputs and outputs. For membranes with partial electrode coverage that does not extend into both out-of-phase regions of the second symmetric mode of the membrane, a single electrode patch is sufficient to capture the large-signal behavior accurately without the need of separation of the electrode into multiple patches.

3.3.2 Calculation of the Electrostatic Force Lookup Table

The relationship between the average gap under an electrode patch and the total force acting on it is defined using the stiffness matrix $\mathbf{K}$, as

$$\mathbf{u} = \mathbf{K}^{-1}\delta^{patch}, \tag{52}$$

where $\mathbf{u}$ is the displacement vector of the membrane when the electrode patch is loaded with 1 Pa static pressure. The sifting vector, δ^{patch}, specifies the nodes of the active electrode patch such that $\delta^{patch} = [\ \delta_1 \quad \delta_2 \quad \dots \quad \delta_i \quad \dots \quad \delta_N\ ]^T$ and

$$\delta_i = \begin{cases} 1 & \text{if node } i \in \text{active electrode patch,} \\ 0 & \text{else.} \end{cases} \tag{53}$$

To calculate the relationship between the mean displacement and total electrostatic force on an electrode patch, the solution of Equation (52) is used for the whole range of membrane displacement. The assumption made here is that the deflection profile within an electrode patch does not change in dynamic operation, so the total electrostatic force acting on the electrode patch can be defined by sweeping the normalized deflection profile calculated by Equation (52) throughout the whole gap. In other words, $(\mathbf{u}/u_{max})g_0 d$ gives any possible non-collapse displacement vector, where u_{max} is the maximum displacement value of the solution of Equation (52), and d is the percentage of deflection such that $0 \leq d \leq 1$. For $d = 0$, the membrane is not deflected and for $d = 1$ the membrane touches the substrate.

For any given membrane displacement profile, the corresponding mean gap and electrostatic force is calculated as

$$g_{mean}(d) = g_0 + \frac{1}{N_{patch}} \sum \frac{\mathbf{u}}{u_{max}} g_0 d,$$
$$\frac{F_{ES}(d)}{V^2} = \sum \frac{-\varepsilon_0 S}{2\left(g_{eff,0} + \frac{\mathbf{u}}{u_{max}} g_0 d\right)^2}, \tag{54}$$

where summation is done over the nodes in the electrode patch of interest, N_{patch} is the number of nodes in the patch, S is the area associated with a single node, and $g_{eff,0}$ is the effective initial gap with an insulation layer with thickness $h_{isolation}$ and relative permittivity $\varepsilon_{isolation}$

$$g_{eff,0} = g_0 + \frac{h_{isolation}}{\varepsilon_{isolation}}. \tag{55}$$

Calculating Equation (54) using the membrane displacement shape calculated in (54) results in the desired relationship between the lumped system variables: total electrostatic force acting on the electrode patch and its mean displacement. Note that in this approach, each nodal area is considered as a separate parallel plate contributing to the total force depending on the gap under that node, thus accounting for the nonuniform membrane deflection in the electrostatic force calculation. This is in contrast with the case in which the whole electrode is modeled as a single parallel plate where the gap and corresponding charge distribution is assumed to be uniform. To emphasize this difference, the force versus average displacement relationship is calculated for both cases for a CMUT which has a 2 μm thickness, 40μm $\times$40μm SiN_x membrane, full electrode coverage, and 100 nm gap thickness with no isolation. The CMUT electrode is divided into two patches to include the effect of change in displacement profile and force distribution within the electrode as the membrane deflects. Figure 47 presents the calculated normalized electrostatic forces as a function of mean gap under the actuation electrode patches. The calculation is done for both electrode patches separately. The proposed method is also compared with the parallel-plate approximation in which the normalized electrostatic force is calculated as a function of the mean gap via the parallel-plate approximation given in Equation (16) in Section 2.2.

In the figure, it can be seen that for large displacements, the total electrostatic forces acting on the electrode patches deviate from the parallel-plate approximation. Note that the center of the membrane has traveled a full 100 nm when the average gap under the center electrode patch (patch 1) is about 32 nm. As expected, the deviation is larger for patch 1, which has a larger curvature and more charge non-uniformity as compared with the side electrode patch (patch 2) as the membrane displacement gets larger. More linear behavior of patch 2 in Figure 47 suggests that the nonlinearity resulting from nonuniform charge distribution can be reduced by exciting the membrane with side electrode actuation, as also presented in [76], where 4 dB reduction in second harmonic distortion is reported with side electrode only excitation utilizing a dual-electrode CMUT.

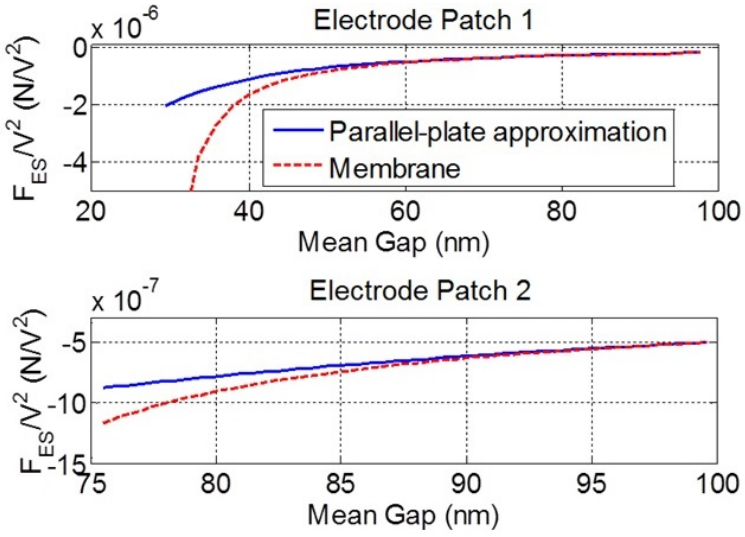

Figure 47: Relationships obtained for the mean gap and total electrostatic force for both electrode patches of the modeled membrane. The relationship is also compared with the parallel-plate approximation.

The calculated relationship is included in the SIMULINK model as a look-up table which takes the average gap of an active electrode patch as its input with the normalized total electrostatic force as the output. The calculation is interpolated linearly by the lookup table in the SIMULINK model for gap values different than the calculated values. Then, the total electrostatic force acting on the electrode patch is calculated by multiplication with the input signal squared, $V^2(t)$.

3.3.3 Transient-vibroacoustic-response Calculation for the Reduced Order System

Because every active electrode patch is modeled separately in our reduced order model, the dynamic problem in Equation (41) is solved for multiple cases, where a single electrode patch is excited in each case. For M total active electrode patches in the model, Equation (41) becomes

$$\left[\mathbf{u}^1\ \mathbf{u}^2\ \ldots\ \mathbf{u}^m\ \ldots\ \mathbf{u}^M\right] = \mathbf{G}^{-1}(\omega)\left[\boldsymbol{\delta}^1\ \boldsymbol{\delta}^2\ \ldots\ \boldsymbol{\delta}^m\ \ldots\ \boldsymbol{\delta}^M\right]. \tag{56}$$

Here, $\mathbf{u}^m$ denotes the displacement vector of the whole meshed array when electrode m is loaded with 1 Pa pressure at frequency of ω. It should be noted that the BEM system is an N degree of freedom coupled system where N is the total number of nodes in the BEM mesh. To reduce the system to an M degree of freedom system where M is the total number of electrode patches, the patches are modeled as lumped elements which take the total electrostatic force acting on them as their input and output the mean displacement. Considering that in an array, the number of mesh nodes is much larger than the number of electrode patches, ($N \gg M$), this approach greatly reduces the number of equations to solve simultaneously for the transient problem.

To model the array as an M-input and M-output system, the relationship between the total electrostatic force acting on the m^{th} electrode patch to the mean displacement of the n^{th} patch is calculated as a function of frequency as

$$\begin{aligned} \bar{u}_n(\omega) &= \frac{1}{N_{patch,n}} \sum \mathbf{u}^m \boldsymbol{\delta}^n, \\ H_{m,n}(\omega) &= \frac{\bar{u}_n(\omega)}{S_m}, \end{aligned} \tag{57}$$

using the solution of (56). Here, the summation is done over the nodes in the n^{th} electrode patch and S_m is the area of the m^{th} patch. In (57), $\bar{u}_n(\omega)$ is the mean displacement of the patch n and $\mathbf{S}$ is the total force acting on the patch m, which is equal its area because a uniform 1 Pa pressure is applied to the patch in (56). The inverse discrete Fourier transform of $H_{m,n}(\omega)$ yields in the impulse response, $h_{m,n}(t)$, the displacement of patch n when m^{th} patch is excited with an impulse. Here, the Hermitian symmetry of $H_{m,n}(\omega)$ is exploited for

the Fourier transform calculation by substituting $H_{m,n}(-\omega) = H^{*}_{m,n}(\omega)$ because $h_{m,n}(t)$ must be a real function [96]. The impulse response relating the force acting on the m^{th} patch and the displacement of the n^{th} patch is incorporated in the SIMULINK model as a discrete FIR filter, where the filter coefficients are the impulse response samples, such that [97]

$$\hat{u}_n[\nu] = \sum_{\tau=1}^{T} B_{\tau}^{m,n} \hat{F}_m[\nu - \tau] = \sum_{\tau=1}^{T} \hat{h}_{m,n}[\tau] \hat{F}_m[\nu - \tau] \tag{58}$$

Here $\hat{u}_n$, $\hat{F}_m$ and $\hat{h}_{m,n}$ are the discrete time-domain displacement of the n^{th} patch, total force acting on the m^{th} patch, and the impulse response relating $\hat{u}_n$ and $\hat{F}_m$. T is the total number of samples and τ is the time step. The time step τ is determined by the maximum frequency for which the BEM problem in (56) is solved and T is determined by the frequency resolution. For example, if (56) is solved for frequencies up to 100 MHz with 50 kHz resolution, the time resolution is 5 ns and T is 4000, which corresponds to total simulation time of 20 μs. A similar approach was pursued to model the radiation impedance of a circular baffled piston for transient SIMULINK simulation of a single piston in Section 2.2.1. The analytical frequency domain representation of the radiation impedance of the circular piston, which relates its velocity and the fluid load acting on itself as a result of its own motion, was incorporated into the model as an arbitrary response FIR filter block with the frequency response equal to the radiation impedance of the piston.

3.3.3.1 MIMO FIR Filter Block

For an example case, the MIMO Simulink filter block for a single membrane with two inputs and two outputs for two electrode patches is presented in Figure 48. The block takes two discrete time force signals as inputs, $\hat{F}_1$ and $\hat{F}_2$, and outputs the multiplexed vector of respective displacements. The FIR filter coefficients are

$$\begin{aligned} \mathbf{B}_1 &= \begin{bmatrix} \hat{\mathbf{h}}_{1,1} \\ \hat{\mathbf{h}}_{1,2} \end{bmatrix} = \begin{bmatrix} \hat{h}_{1,1}[1] & \hat{h}_{1,1}[2] & \dots & \hat{h}_{1,1}[T] \\ \hat{h}_{1,2}[1] & \hat{h}_{1,2}[2] & \dots & \hat{h}_{1,2}[T] \end{bmatrix}, \\ \mathbf{B}_2 &= \begin{bmatrix} \hat{\mathbf{h}}_{2,1} \\ \hat{\mathbf{h}}_{2,2} \end{bmatrix} = \begin{bmatrix} \hat{h}_{2,1}[1] & \hat{h}_{2,1}[2] & \dots & \hat{h}_{2,1}[T] \\ \hat{h}_{2,2}[1] & \hat{h}_{2,2}[2] & \dots & \hat{h}_{2,2}[T] \end{bmatrix}, \end{aligned} \tag{59}$$

where the number of rows in each coefficient matrix is equal to the number of patches, M, where is $M = 2$ in this case. Each filter block takes the respective total force as its input and outputs the multiplexed displacements. The contributions from each block are then added together, giving the linear multiplexed MIMO displacement output vector. The unit delay block is added to break the algebraic loop introduced by the FIR filters and the gap feedback in the SIMULINK model in Figure 45. Information about the details of the algebraic loop phenomenon in the SIMULINK model can be found in the SIMULINK documentation [98]. Introduction of the unit delay to break the algebraic loop introduces inaccuracies to the transient solution, especially in the nonlinear operation regime. To compensate for the loss of accuracy caused by the unit delay, the calculated impulse responses $\hat{h}_{m,n}$ can be upsampled, increasing the sampling time in the time domain calculation in SIMULINK [97]. However, increased sampling time for the sake of nonlinear calculation accuracy results in longer simulation time.

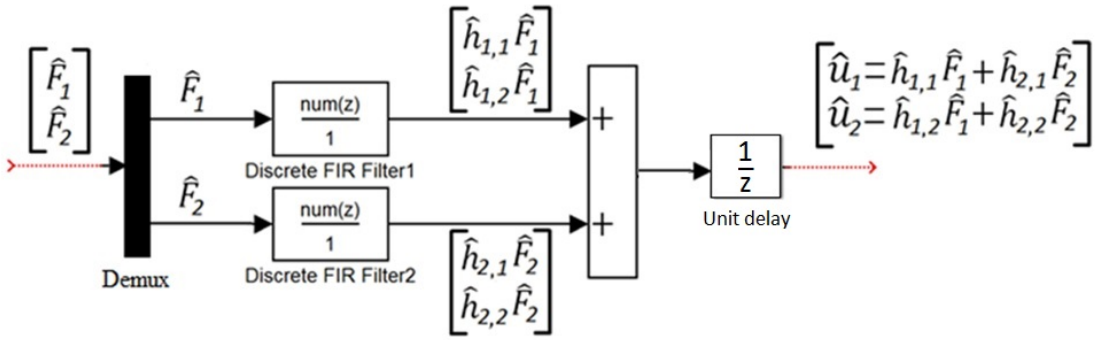

Figure 48: The MIMO FIR block in the Simulink model relating total forces acting on electrode patches and mean patch displacements for an example case of a single membrane with two patches

The extension of the approach to an arbitrary number of electrode patches is straightforward, requiring one FIR filter block per patch, modeling the array as an M-input M-output system with the total electrostatic forces acting on array electrode patches as the inputs and the mean displacements as the outputs. If the total electrostatic forces acting on each transmitting electrode patch are known, the mean displacements can be solved using the MIMO

FIR filter block. Together with the electrostatic force calculation, this block completes the SIMULINK model, which takes the time-domain drive signals for each electrode patch as input and outputs the total electrostatic forces for pressure calculation.

3.3.4 Pressure Calculation at an Arbitrary Point in the Immersion Fluid

Once the forces on the electrode patches are known, the pressure at point $\vec{\mathbf{r}}$ when the m^{th} electrode patch is excited can be calculated as a function of frequency using the baffled point-radiator model [99]

$$p_m^{\vec{\mathbf{r}}}(\omega) = \sum_{i=1}^{N} \frac{-\rho_{fl}\omega^2 S}{2\pi} \frac{e^{-j\mathbf{r}_{\vec{\mathbf{r}}}k}}{\mathbf{r}_{\vec{\mathbf{r}}}} 10^{-\alpha \mathbf{r}_{\vec{\mathbf{r}}}/20} \mathbf{u}^m \tag{60}$$

where the summation is done over the whole meshed array with the nodal displacements calculated in Equation (56), and $\mathbf{u}^m$ is the displacement of the nodes when only the m^{th} electrode patch is excited. Here, $\mathbf{r}_{\vec{\mathbf{r}}} = \begin{bmatrix} r_1 & r_2 & \dots & r_i & \dots & r_N \end{bmatrix}^T$ is the distance vector composed of the distances between the point where pressure is calculated and the BEM nodes. Note that with this approach, the pressure is not calculated from average electrode patch displacements as pistons, rather all the high-spatial-resolution nodal displacement information from BEM is retained while performing the pressure calculation. Similar to the derivation of (57), a frequency-domain relationship relating the total electrostatic force acting on the mth patch and the pressure at point $\vec{\mathbf{r}}$ is calculated as

$$P_m^{\vec{\mathbf{r}}}(\omega) = \frac{p_m^{\vec{\mathbf{r}}}(\omega)}{S_m}. \tag{61}$$

Using the superposition principle, the system can be modeled as a MISO system and the pressure contributions from each excited electrode patch can be added up to find the total pressure at the point of interest via Equation (38).

3.4 Model Verification

3.4.1 FEA Comparison

For verification purposes, the CMUT element shown in Figure 46 is modeled in a 2×2 array configuration for large-signal transient analysis and each full electrode is divided into two

patches as shown in Figure 46. The membrane pitch was set to 50 μm. The simulation is set up such that all four array elements are excited with the same drive signal and the pressure at the array surface in the middle of the array is calculated both with COMSOL and the presented model. In the first case, a 20-ns-long 70-V pulse is applied to the array without dc bias, which results in full-gap membrane swing. The time-domain pressure signals and their spectra for both FEA and the lumped model are presented in Figure 49. The two are in excellent agreement, with 1 dB max difference up to 40 MHz for this 10-MHz CMUT, which shows the capability of the model with large-signal actuation.

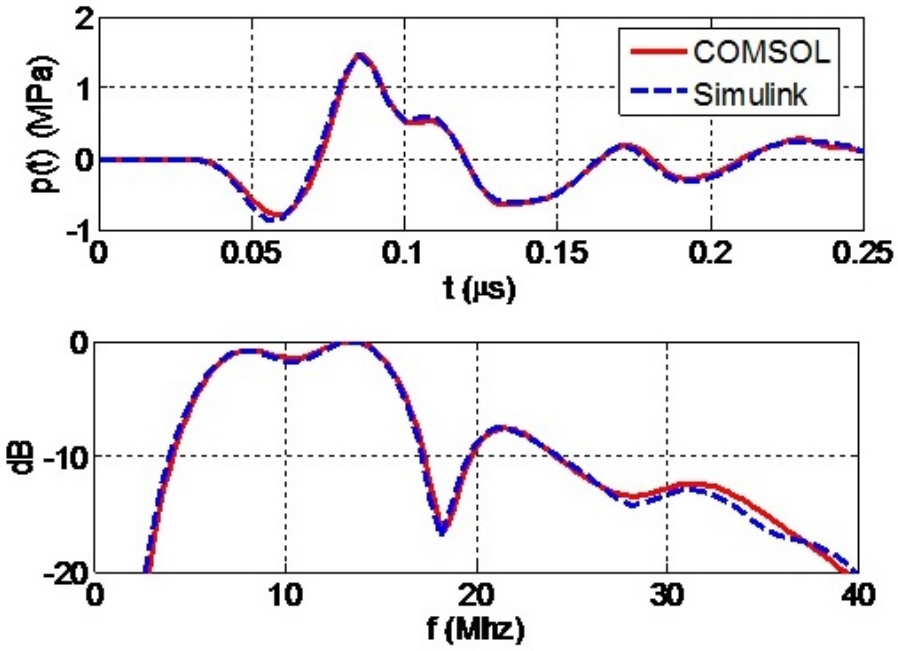

Figure 49: Simulated pressure at the array surface with FEA and the model from this study, with corresponding spectrum for a high amplitude, short pulse resulting in full gap swing.

In the second case, the same device is driven by a 50-V, 5-MHz, 1-cycle tone burst with no dc bias, similar to the suggested sub-harmonic drive mechanism in Section 2.3.1. The applied signal results in full-gap membrane swing to drive the CMUT array and also the electrostatic actuation signal is still active when the full gap is achieved, representing the worst case scenario in terms of nonlinearities. Figure 50 presents the time domain pressure signals and their spectra for the lumped model and FEA. To emphasize the significance of

multiple patches, the FEA result is also compared with the model without separating the transmit electrode into two patches. In Figure 50, it can be seen that the nonlinear behavior of the CMUT array is captured more accurately when the transmit electrode is divided into two patches, which incorporates the effect of the change in the displacement profile and charge distribution within the electrode when the CMUT membrane goes through large displacements, as discussed in Section 3.3.1.

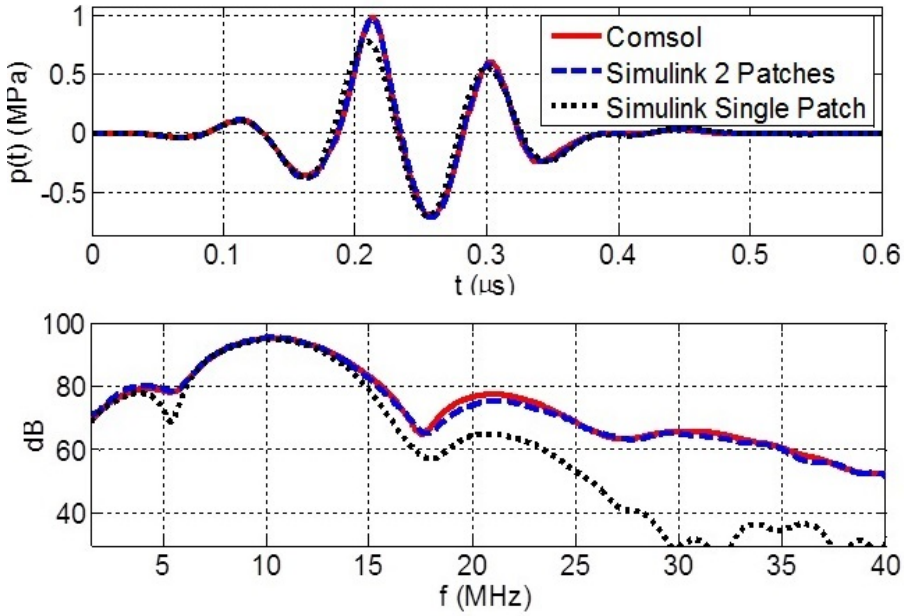

Figure 50: Simulated time and frequency domain pressure signals at the array surface for a 1 cycle tone-burst with no dc bias resulting in full-gap swing evaluated with FEA and the lumped model with a single electrode patch and two electrode patches modeling the transmit electrode

3.4.2 Experimental Validation

A 16-membrane CMUT element was used, shown in Figure 51, for experimental verification of the model. The device is composed of 2.2-μm-thick, 35-μm square SiN_x membranes with 25 μm electrodes. The gap thickness is 50 nm at rest, the SiN_x electrode isolation layer is 200 nm thick, and the array pitch is 45 μm. The low-temperature process presented in [100] was used for transducer fabrication. The array was tested in vegetable oil and the transmitted pressure was measured with a broadband hydrophone which has a bandwidth

of 40 MHz (HGL-0085, Onda Corp., Sunnyvale, CA). The experimental setup is shown in Figure 51. The attenuation in the vegetable oil was measured as a function of frequency, as given in Figure 52, using the attenuation parameter estimation method presented in [101] and a curve was fit to the measured data assuming that the attenuation coefficient is in the form of Af^B, where f is frequency, and A and B are constants.

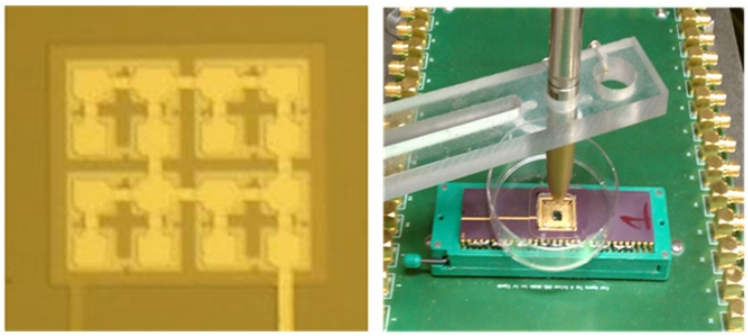

Figure 51: 16-membrane CMUT array used for experiments and the experimental setup with a broadband hydrophone

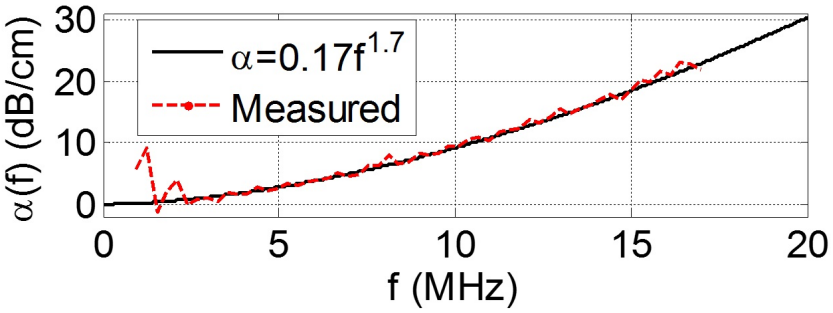

Figure 52: Measured attenuation coefficient of vegetable oil as a function of frequency and the curve fit used in simulations

For model validation, the pressure 2.2 mm away from the array was measured for the same drive signal which was measured in the experimental setup and used in the simulations. The collapse voltage of the CMUT in test was measured and simulated to be 40 V. The resonance frequency of the device in air for 25 V dc bias was simulated as 17 MHz, and measured as 18 MHz with a network analyzer. Each individual membrane was modeled with an 11×11 mesh grid in the BEM formulation, and each electrode was divided into

two patches. The time domain pressure signals for no dc bias and 45-V 30-ns pulse and their frequency spectra are presented in Figure 53. The simulation and experiment match within 2 dB up to 40 MHz, which is 20 MHz above the upper 3 dB cut-off frequency of the transducer. The results match fairly well considering the 10% uncertainty in fabrication in terms of membrane and gap thickness.

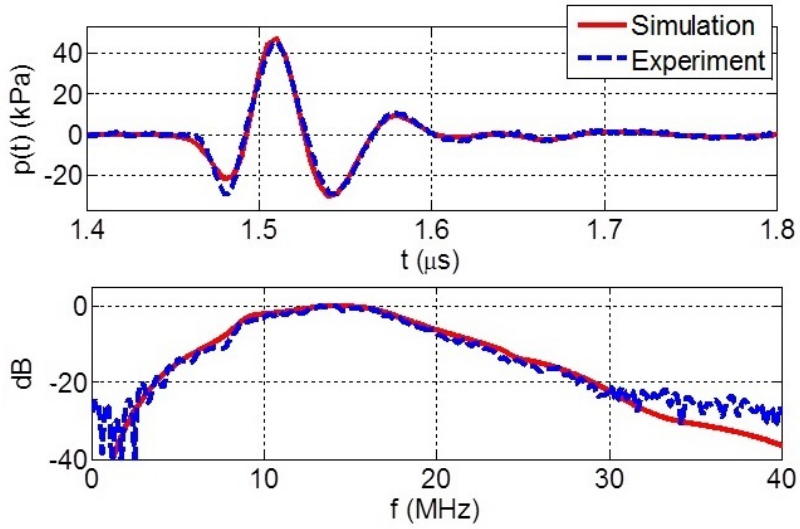

Figure 53: Simulated and experimental pressure when the transducer is excited with no dc bias and 30-ns 45-V pulse.

3.4.3 Simulation of a Phased Array

With the ability to apply arbitrary signals to multiple individual CMUT membranes, the model can be used for the investigation of phased arrays. As an example, a 16-element CMUT array as shown in Figure 54 is simulated when each of the array elements are excited with different input signals. The array size and symmetry constraints were set by the maximum size of the three-dimensional transient FEA problem that can be handled by a desktop computer using COMSOL. The CMUT array comprised of 2-μm-thick 40-μm-square membranes with 100 nm gap and no electrode isolation. The pressure 100 μm away from the center of the array surface at $\vec{\mathbf{r}}_f = [0, 0, 100\mu m]$ is calculated both with the lumped model and COMSOL when the array is excited to focus at $\vec{\mathbf{r}}_f$ and without

focus. Appropriate time delays presented in Table 4 are introduced to the drive signals for each membrane to focus the array, as determined by the distances between the center of membranes and $\vec{\mathbf{r}}_f$ such that

$$\begin{aligned} t_{d,i} &= \frac{\left|\vec{\mathbf{r}}_f - \vec{\mathbf{r}}_4\right| - \left|\vec{\mathbf{r}}_f - \vec{\mathbf{r}}_i\right|}{c}, \\ V_i(t) &= V(t - t_{d,i}). \end{aligned} \tag{62}$$

Here, $\vec{\mathbf{r}}_i$ indicates the coordinates of the center of i^{th} membrane, $V(t)$ is the drive signal applied to the elements, and $V_i(t)$ is the voltage signal acting on the i^{th} element in the array. The pressure signals at $\vec{\mathbf{r}}_f$ are also presented in Figure 54 for a 65-V, 40-ns pulse applied to the array elements with and without the focusing delay. It can be seen that the pressure at the desired point is increased when the focusing delay is applied, as expected. The results compare well to COMSOL simulations and demonstrate the capability of the model for phased-array simulations.

Table 4: Required delays to focus at $[0, 0, 100\mu m]$

Patch	Delay
1a, 1b	~26 ns
2a, 2b, 3a, 3b	~12 ns
4a, 4b	0 ns

3.5 Incorporation of Source Impedance

To include the transmit electronics in the model, the CMUT is considered as a nonlinear capacitor in the electrical domain. The transmit circuitry is modeled with its output impedance assuming the interface circuit is linear within the operation range. With the addition of the source impedance, the resulting circuit is shown in Figure 55. Given the source voltage $V_S(t)$, the voltage acting on the CMUT capacitance, V(t), and the current

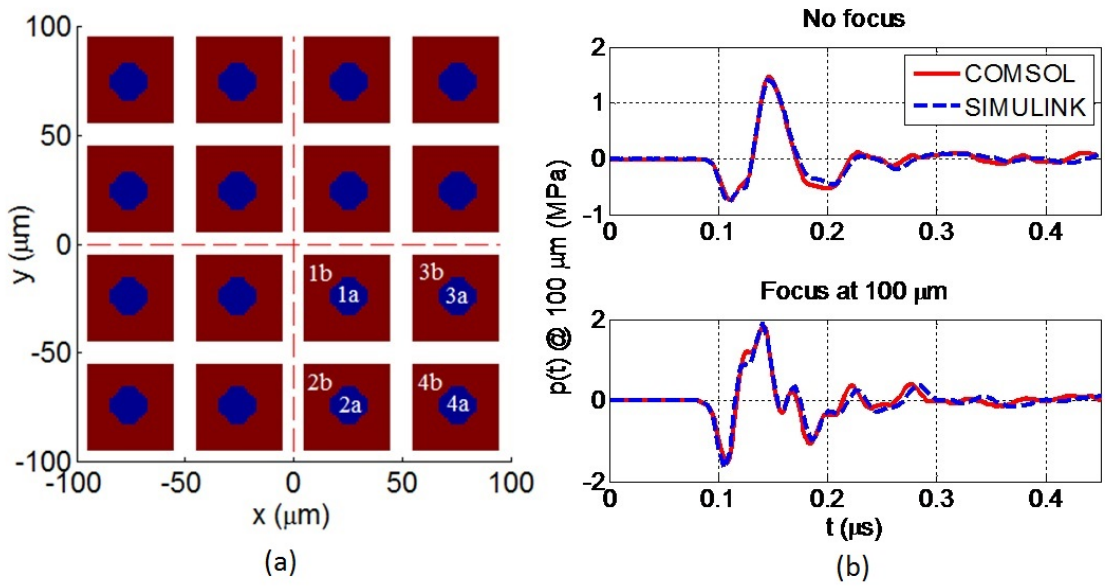

Figure 54: (a) Simulated phased array geometry (b) Pressure at 100 μm with and without focus when array is excited with a short pulse

flowing through the source i(t) can be calculated as

$$\begin{aligned} V(t) &= V_S(t) - i(t) * \mathcal{F}^{-1}\{Z_S(\omega)\}, \\ i(t) &= \frac{dQ(t)}{dt} = \frac{d\left(V(t)\left(C(t) + C_p\right)\right)}{dt}. \end{aligned} \tag{63}$$

Here $\mathcal{F}^{-1}\{Z_S(\omega)\}$ is the inverse Fourier Transform of the source impedance and C_p is the parasitic capacitance. The electrode of the CMUT is divided into two patches and the capacitance of each electrode patch is calculated as a function of its mean displacement using the parallel plate approximation where

$$C(t) = \frac{\varepsilon_0 A}{g_0 + \bar{u}(t)}, \tag{64}$$

A is the patch area, g_0 is the effective gap at rest and $\bar{u}(t)$ is the mean displacement of the patch.

The SIMULINK model for the transmit mode is shown in Figure 56. The model takes the electrical drive signals of each transmit electrode patch as the input vector $\mathbf{V}_S(t)$, and outputs the electrostatic forces acting on each patch as vector $\mathbf{F}(t)$ and electrode patch displacements, $\mathbf{U}(t)$, as a function of time. It should be noted that every signal in the model

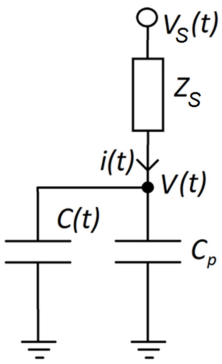

Figure 55: Electrical circuit employing the CMUT as a variable capacitor, the source impedance and the parasitic capacitance

is multiplexed and carries separate time domain signals for each electrode patch. The force vector $\mathbf{F}(t)$ is then post-processed for calculation of time domain pressure at an arbitrary point in the immersion field as explained in Section 3.3.4.

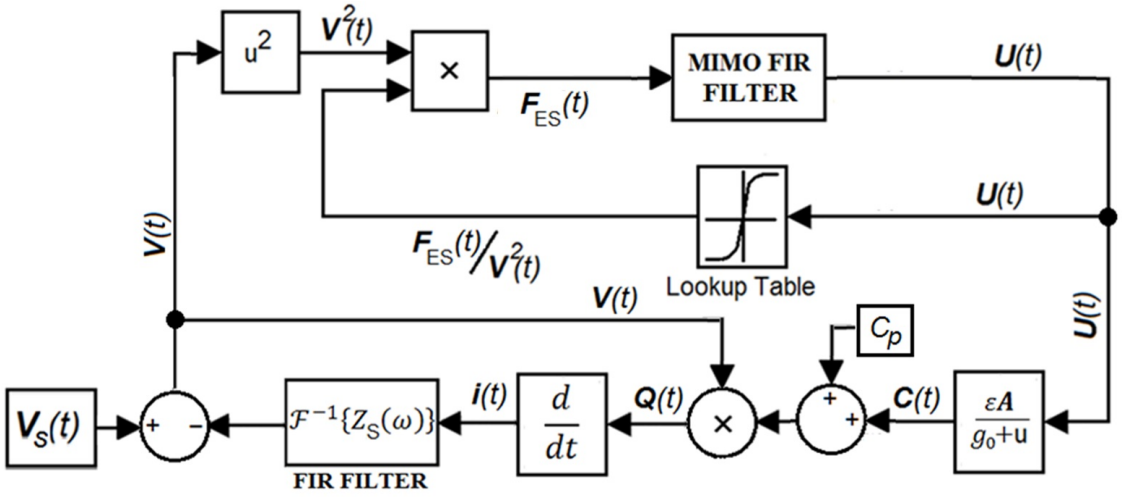

Figure 56: Large-signal SIMULINK model for transmit mode with incorporated parasitic capacitance and source impedance

3.5.1 Verification Example: Gap Feedback Linearization of a Dual-electrode CMUT

The presented modeling approach is verified by comparison to COMSOL simulations for the case of a single circular CMUT membrane in transmit, receive and pulse-echo modes. A single circular membrane is chosen in order to have a computationally feasible size for the FEA model as it gets computationally more expensive with increasing number of array

elements. A 2 μm thick SiN_x circular CMUT element is modeled as the example device. The CMUT membrane radius is 20 μm. The device has 50 nm gap, no electrode isolation, 75% electrode coverage and is immersed in water. The transducer has 8.5 MHz center frequency and the collapse voltage is 13 V. The device electrode is separated into two patches based on the modal analysis of the membrane for increased accuracy and also to have the capability of simulating a dual-electrode CMUT as described below. The meshed membrane is shown in Figure 57.

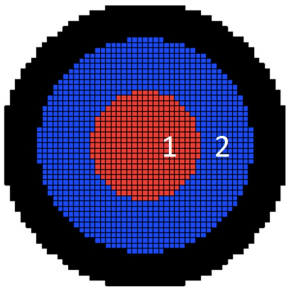

Figure 57: The simulated circular CMUT membrane with 75% electrode coverage

The modeled CMUT is simulated for harmonic distortion analysis both with the presented method and COMSOL. A dual-electrode CMUT structure with separate electrodes connected to different driver circuitry was simulated to show the generality of the model as well as to demonstrate further improvements in harmonic reduction using a series impedance feedback approach presented in Section 2.4. In [76] it has been reported previously that side electrode actuation of CMUTs result in reduced nonlinear behavior. Since the dual-electrode CMUT structure presented in [76] makes use of leveraged bending [91], large membrane displacements can be attained while the side electrodes go under smaller displacements. Consequently, electrostatic nonlinearity is reduced as the electrode displacement is decreased for the same membrane displacement amplitude. When combined with the gap feedback method as shown in Figure 58, this property of the dual-electrode CMUT can further suppress the CMUT nonlinearity. The proposed topology employs two feedback impedances connected in series to the side and center electrodes, driven by the same

voltage source. As the CMUT is actuated and displaced, the voltages acting on both electrodes are adjusted by the resulting RC filter separately, as a function of each electrodes individual displacement.

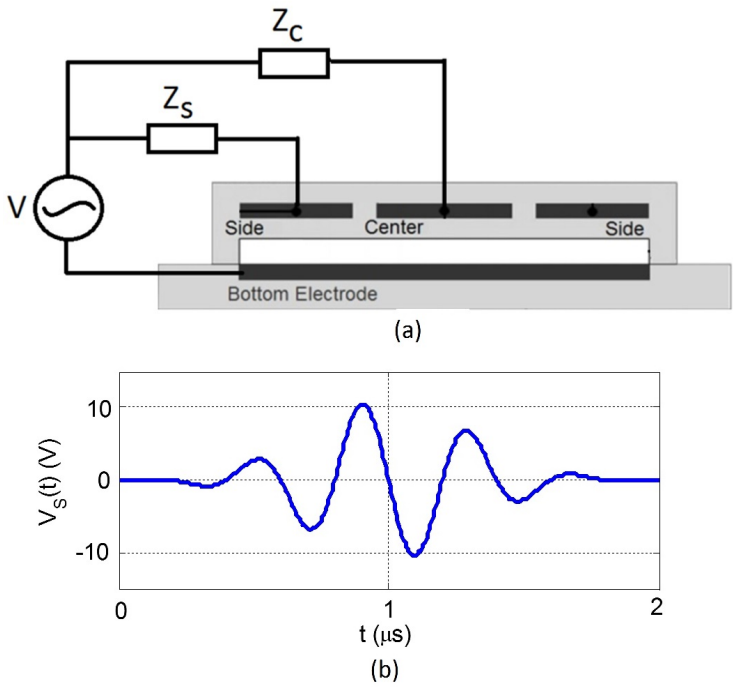

Figure 58: (a) Dual electrode gap feedback topology (b) Applied drive signal

The dual-electrode gap feedback approach is implemented on the example circular CMUT. The electrode patches 1 and 2 in Figure 57 are utilized as separate center and side electrodes, respectively. The fundamental operation frequency is selected as 5 MHz, so the second harmonic component is at 10 MHz. The device is actuated with an 11V 2.5 MHz sine wave enveloped by a 300 ns Gaussian signal and no dc bias (Figure 58(b)). It should be noted that as the device is driven without dc bias, the fundamental component of the output pressure is at twice the frequency of excitation. The simulation results are presented in Figure 59. The resulting time domain mean membrane displacement and the output pressure at 20 μm away from the transducer are shown in Figure 59(a,c) for the no feedback case. Figure 59(b,d) presents the results for the dual electrode gap feedback

implementation where the transducer is driven by amplitude doubled 22 V excitation signal and 3 MΩ and 1 MΩ feedback resistors are used as feedback components for center and side electrode, respectively. Selected resistor values apply a larger feedback gain to the center electrode, which behaves more nonlinearly compared to the side electrode. The pressure spectra for the cases with and without feedback are given in Figure 59(e). Using the dual electrode feedback topology, the second harmonic magnitude is suppressed by ~12 dB, reducing the harmonics ~23 dB below the fundamental by doubling the input voltage. Also note that the results show excellent agreement with the COMSOL simulations, demonstrating the versatility and the accuracy of the model.

3.6 Conclusion

A key benefit of the modeling and simulation approach presented is its generality in terms of individual CMUT geometry, CMUT placement in an array, and large-signal actuation capability of phased CMUT arrays. With this approach, it is possible to investigate the interaction of arrays of CMUTs with arbitrary geometry and actuation for expedited iterative design optimization. Because the model is based on a two-dimensional surface mesh, increasing the array size has been shown to be computationally less expensive than using three-dimensional transient FEA. Because the Simulink model blocks are pre-calculated for a given array geometry, the transient Simulink model takes less than a second to run. This is a significant advantage over FEA, because the model can be simulated for different drive signals for individual array elements iteratively in a significantly reduced computation time. The model is also capable of modeling CMUT behavior with external circuit elements because time-domain instantaneous capacitance can be calculated As a further development, a SPICE netlist of the driving circuitry can be incorporated in the SIMULINK model as a block, so the whole system can be simulated simultaneously.

For an initial set of parameters, and based on the individual membrane geometry, either

the finite difference method or the hybrid-FEA method can be used to generate the stiffness matrix depending on the geometry. Single or multiple membrane geometries, each with a separate **K** matrix, can be arranged into an array with subsequent analysis using the BEM. With the MIMO vibroacoustic and MISO pressure calculation blocks derived from these calculations, SIMULINK is used with drive signals to compute the output pressure. Because the model is generated in discrete steps, it can be seen that optimization or modification can be more or less computationally expensive depending upon the parameter modified, such as mass loading, array spacing, gap thickness, and applied signal. For example, because the gap thickness has minimal influence on the frequency response, that parameter can be iterated quickly without modifying the MIMO and MISO blocks or changing the array geometry, and does not require recalculation of the **K** matrix. Because iterative optimization is an important feature of ultrasound transducer design, this model is generally well-suited for rapid and accurate design of CMUT arrays for a variety of applications and quantitative studies of fundamental transducer characteristics, such as energy conversion efficiency and linearity.

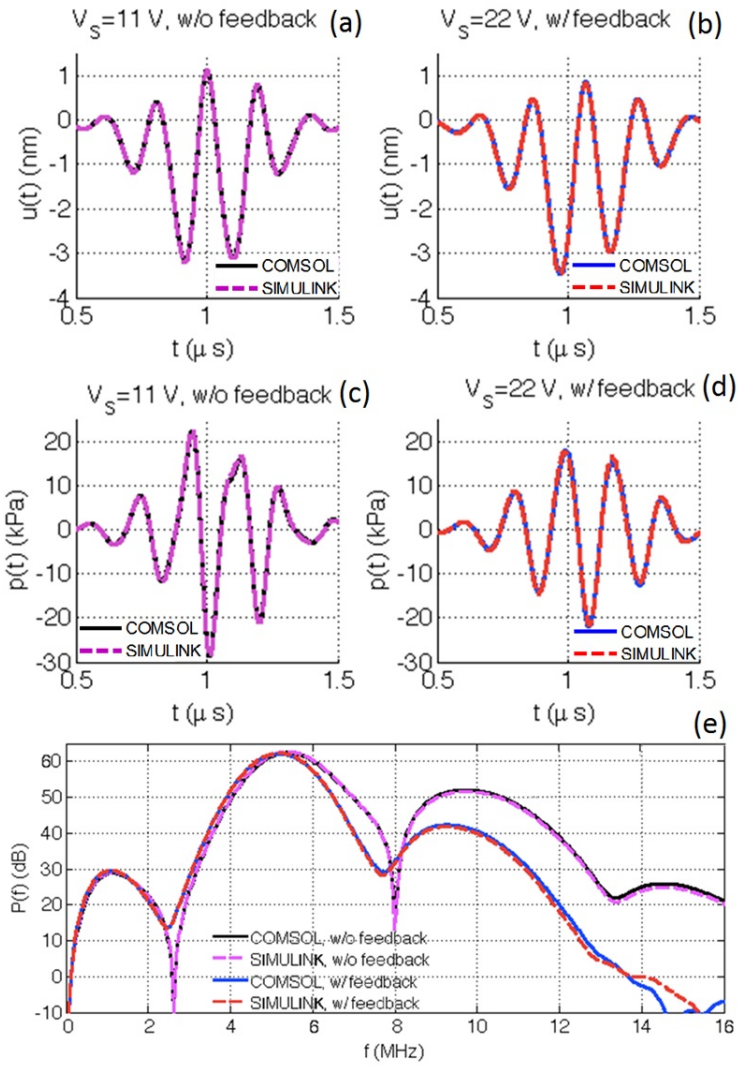

Figure 59: (a) Time domain displacement for conventional single electrode operation (b) Time domain displacement for dual electrode gap feedback operation (c) Transmitted pressure for conventional single electrode operation (d) Transmitted pressure for dual electrode gap feedback operation (e) Spectra of the transmitted pressure for conventional single electrode and dual electrode gap feedback operation

CHAPTER 4

LUMPED LARGE-SIGNAL MODELING OF CMUT ARRAYS IN RECEIVE AND PULSE-ECHO MODES

In this chapter, the extension of the large-signal CMUT transmit array model presented in Chapter 3 to receive and pulse-echo modes of operation is presented with the addition of transmit-receive electronics. First the receive model is described where the output electrical signals are calculated with a pressure field generated by another ultrasound source present in the immersion medium. Next, pulse-echo operation, more specifically reflection from a hard or a soft wall, is considered as a special case, where the incident field is generated by the image of the CMUT array itself. Model validation is performed via COMSOL simulation comparisons for several example cases covering the receive and pulse-echo models. To demonstrate the computational efficiency, the two-way response of a partial dual-ring intravascular ultrasound array is simulated using a high-performance computing cluster, where the output currents of individual array elements are calculated for given input pulse. Dependence of the output signals on receiver dc bias levels is investigated to indicate the potential of the model as a versatile tool for rapid iterative CMUT array design and simulation in MATLAB environment.

4.1 Receive Model

In receive mode operation, the critical step is the proper inclusion of the incident pressure field, $\mathbf{p}_{in}$, in the boundary element problem formulation. Given the mass $\mathbf{M}$ and stiffness $\mathbf{M}$, matrices of the boundary element problem description formulated in Equation (40), and the electrostatic pressure vector acting on the transducer nodes, $\mathbf{p}_{ES}$, the nonlinear array response can be calculated in the presence of an incident sound field transmitted by an arbitrary source in the immersion fluid. In the receive mode, the reflected field from the array surface is the sum of the blocked reflected field, which is the reflection of the incident

field from the rigid baffle and the radiated field due to the surface vibrations [72]. An example meshed CMUT membrane in the presence of another source is shown in Figure 60, where the time domain force balance equation governing the dynamics of the node j becomes

$$m\ddot{u}_j + \mathbf{k}_j\mathbf{u} + \sum_{i=1}^{N} \frac{\rho_{fl} S\, \ddot{u}_i(t - \frac{r_{i,j}}{c_{fl}})}{2\pi r_{i,j}} \beta(r_{n,i}, u_n). = p_{ES,j} + 2p_{in,j} \tag{65}$$

in the presence of an incident sound field. Here the u_j is the displacement of j^{th} node and u is the nodal displacement vector.

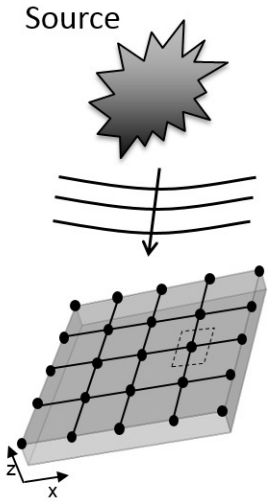

Figure 60: Example CMUT membrane as a receiver divided into 5×5 matrix of nodes in the presence of another source in the immersion fluid.

The third term on the left hand side of Equation (65) is the total radiated field due to vibration of the whole array surface with nodal area, S, and $2p_{in,j}$ is the blocked pressure acting on node j, i.e. the pressure acting on the node due to the incident field and its mirror with respect to the array surface. Equation (65) is nonlinear due to the gap dependence of the electrostatic pressure; hence the solutions for the electrostatic pressure and the incident field cannot be separated using the superposition principle. The reduced order lumped modeling approach is pursued as in transmit modeling in Section 3.3 where the total forces and displacements of membrane patches are system variables. The total driving force acting on electrode patch m is $F_m = F_{ES,m} + 2F_{in,m}$. Here $F_{ES,m}$ is the total electrostatic force acting

on the electrode patch and $F_{in,m}$ is the total force acting on the patch due to the incident sound field, i.e.

$$F_{in,m} = S \sum_{i \in m} p_{in,i} \tag{66}$$

where the summation is done over the m^{th} patch.

4.1.1 SIMULINK Model with Receive Electronics

The receive circuitry is incorporated in the model with its output impedance assuming the interface circuit is linear within the operation range. Assuming a bias voltage $V_{DC}(t)$, the resulting circuit with the addition of the receive impedance is shown in Figure 61, where the voltage acting on the CMUT capacitance, $V(t)$, and the CMUT output current, $i(t)$, are calculated as

$$\begin{aligned} V(t) =& V_{DC}(t) - i(t) * \mathcal{F}^{-1}\left\{Z_R(\omega) \parallel C_p\right\}, \\ i(t) =& \frac{dQ(t)}{dt} = \frac{d\left(V(t)C(t)\right)}{dt}. \end{aligned} \tag{67}$$

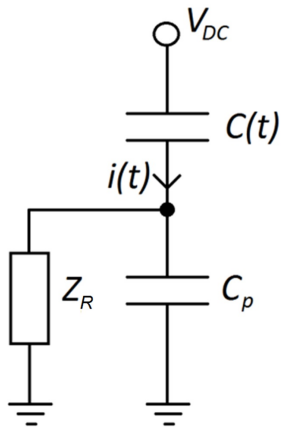

Figure 61: Electrical circuit for receive operation employing the CMUT as a variable capacitor

The resulting SIMULINK model is shown in Figure 62 where the total forces due to the incident field and electrostatic actuation are added for transient array simulation in receive mode. With the output signal available, and knowing the noise characteristics of the CMUT element and electronics through their electrical impedances, one can obtain the signal to noise ratio for given pressure input. Hence the model is useful in computing

the minimum detectable pressure of the array elements considering the parameters of the integrated system.

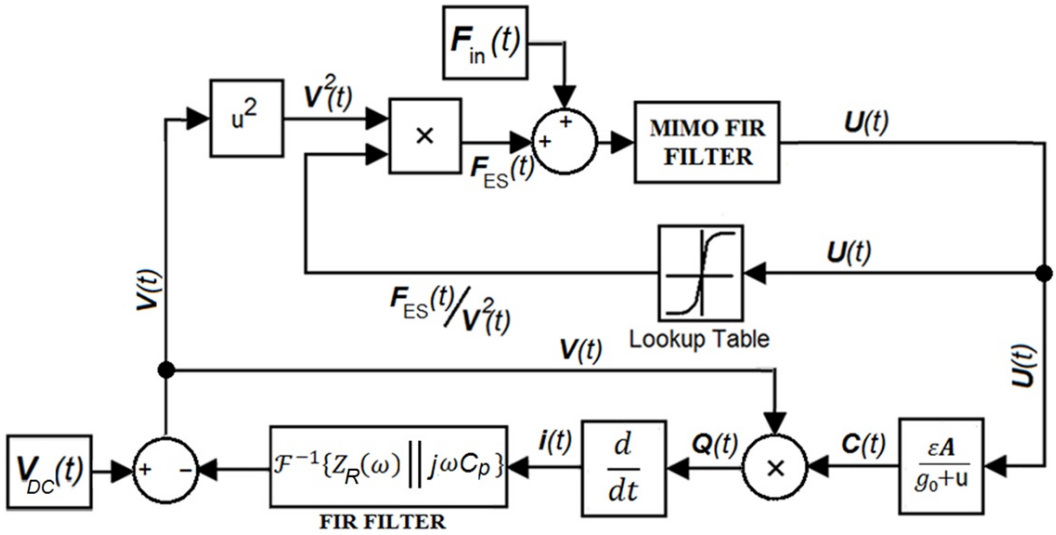

Figure 62: Large Signal SIMULINK Model for Receive Mode

4.1.2 Receive Model Verification via FEA Comparison

To demonstrate the receive modeling capability with arbitrary electrical termination, the example circular CMUT presented in Figure 57 in Section 3.5.1 is simulated for an incident plane wave with normal incidence when the CMUT is biased to 90% of its collapse voltage for short circuit and resistive termination cases. The electrical termination conditions affect the CMUT dynamics and the gain-bandwidth product of a CMUT [102]. In the simulations, the incident plane wave is a Gaussian enveloped tone burst with 7 MHz center frequency and 1 kPA amplitude as shown in Figure 63.

The time domain mean displacements averaged over the whole CMUT membrane and output currents due to the incident plane wave and their spectra for short circuit and 50 kΩ terminations are given in Figure 64. The discrepancy of mean membrane displacements and the calculated output currents between the COMSOL and the SIMULINK model results is less than 1% where the accuracy would be improved by using more patches to model the device electrode. This small set of results show that bandwidth of the receiving CMUT is

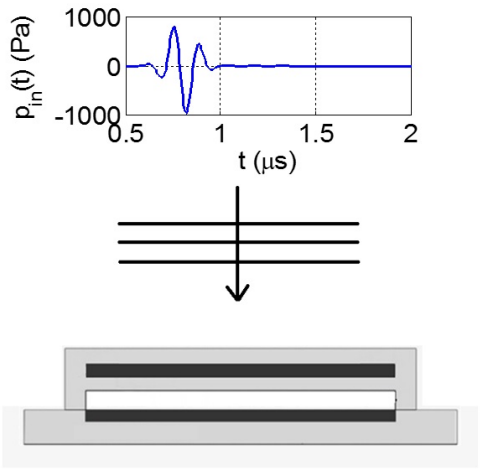

Figure 63: Large Signal SIMULINK Model for Receive Mode

improved while the receive gain is reduced with resistive loading, indicating the possibility of optimizing the device performance with certain trade-offs.

4.2 Pulse-echo Model

Ultrasonic transducers, including both micromachined and piezoelectric ones, are commonly characterized with pulse echo experiments. Using a metal block as the reflector, approximating a hard wall, a linear, reversible ultrasonic transducer can be fully calibrated with a single voltage measurement [103]. These calibration methods rely on the self-reciprocity of the piezoelectric transducers. Although CMUTs don't satisfy the linearity and reciprocity requirements for the developed methods, pulse echo testing is the most common method for CMUT characterization. Therefore a model capable of simulating such a case would a useful tool for CMUT design and it can be used for simple CMUT-piezoelectric transducer comparisons. The modeling of pulse-echo operation via FEA is especially computationally expensive since the immersion fluid must be meshed fine enough within the whole fluid domain to model the propagation of the transmitted and reflected wave accurately [104]. This is in contrast with transmit only case where fine meshing is needed only close to the source. Requirements for mesh size, time step and

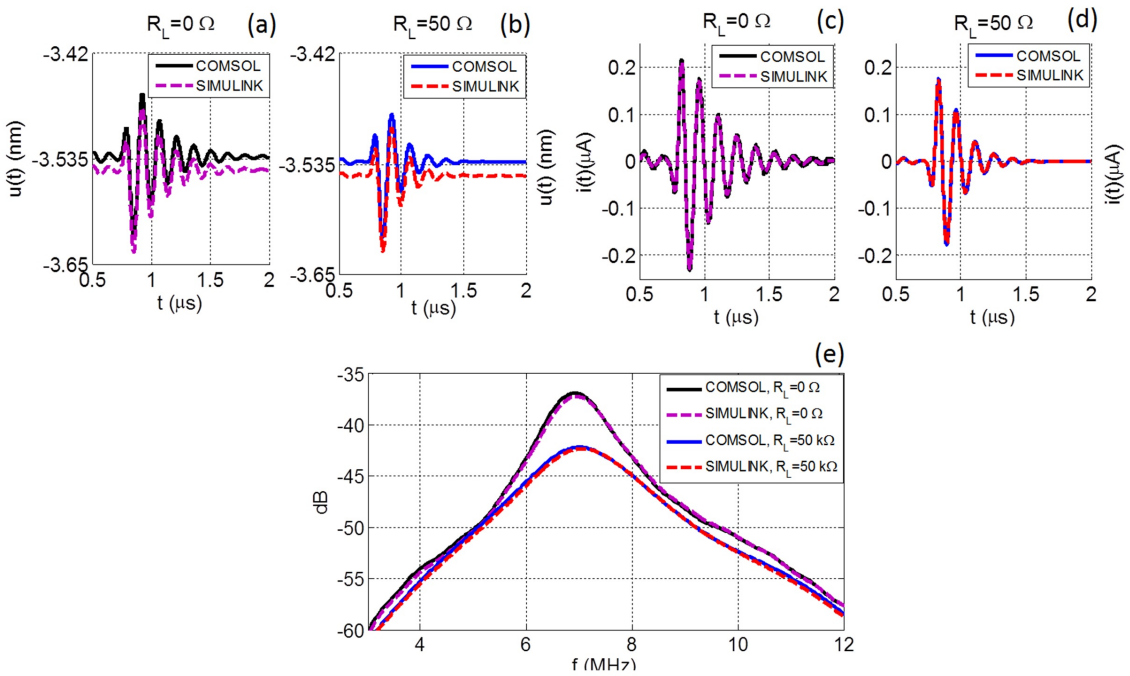

Figure 64: (a) Mean membrane displacement in receive mode for short circuit termination (b) Mean membrane displacement in receive mode when the CMUT is terminated with a 50 kΩ resistor (c) Output current for short circuit termination (d) Output current for 50 kΩ resistive termination (e) Output current spectra in receive mode for short circuit termination and when the CMUT is terminated with a 50 kΩ resistor

modeling of the whole fluid domain for two-way propagation renders FEA computationally impractical for CMUT pulse echo simulations using a desktop computer. On the other hand pulse echo operation affects the computational load minimally for BEM as the fluid loading is incorporated in the calculations analytically as shown below.

Presence of a flat reflector in the immersion medium alters the boundary conditions of the vibroacoustics problemformulated in Equation (40). Therefore the Green's function given in Equation (49) for immersion semi-infinite fluid needs to be modified accordingly. When a perfectly parallel hard wall reflector is facing the array surface at distance z_0, the fluid coupling term between i^{th} and j^{th} nodes becomes

$$Z_r^{i,j}(\omega) = \frac{j\rho_0\omega S}{2\pi}\sum_{n=0}^{\infty}\frac{e^{-jk\sqrt{r_{i,j}^2+(2nz_0)^2}}}{\sqrt{r_{i,j}^2+(2nz_0)^2}}10^{-\alpha(\omega)\sqrt{r_{i,j}^2+(2nz_0)^2}/20}. \tag{68}$$

The formulation is based on method of images to account for the hard wall boundary condition [17]. Here the summation takes the multiple reflections into account where $n = 0$ term is the direct coupling between the nodes, $n = 1$ term is the first reflection, $n = 2$ term is the second reflection, etc. The diagram for the method of images is shown in Figure 65. For broadband operation where the transmitted pulse is shorter than the time required for two way propagation, the summation can be truncated at the first reflection. In continuous wave operation, the superposition of multiple reflections must be accounted. As the amplitude of the reflections decrease with increasing order of reflections due to attenuation in the fluid medium and diffraction, the Green's function accounting for multiple reflections in Equation (68) converges. Therefore the summation in Equation (68) is evaluated up to convergence, eliminating the need for infinite summation.

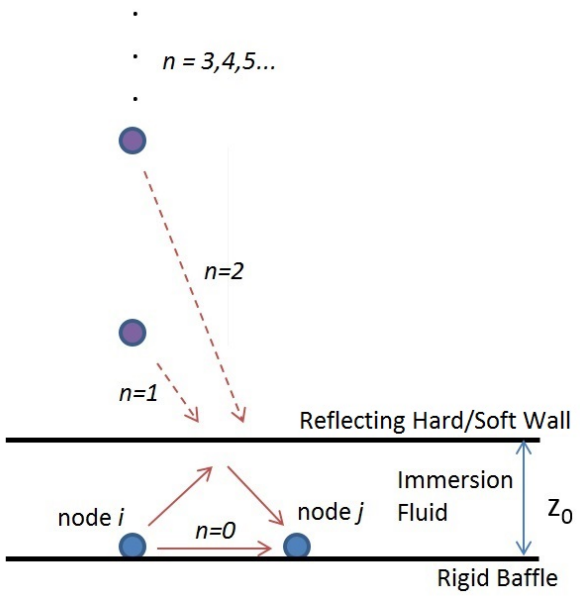

Figure 65: Geometry used for derivation of the modified Green's function via method of images

Additionally, for soft boundary condition at the reflecting surface, e.g. water-air interface, the modified Greens function becomes

$$Z_r^{i,j}(\omega) = \frac{j\rho_0\omega S}{2\pi}\sum_{n=0}^{\infty}(-1)^n \frac{e^{-jk\sqrt{r_{i,j}^2+(2nz_0)^2}}}{\sqrt{r_{i,j}^2+(2nz_0)^2}} 10^{-\alpha(\omega)\sqrt{r_{i,j}^2+(2nz_0)^2}/20}. \tag{69}$$

taking the 180° in phase change in every reflection from the soft boundary into account. The modified Green's function can be incorporated in the BEM formulation directly by substitution of Equation (68) or (69) in Equation (40) for hard or soft wall reflector respectively. The SIMULINK model in Figure 66 describes the complete system in pulse-echo operation. The switch in the model selects the transmit circuitry during the transmit operation and selects the receive circuit during the reception of the echo signal.

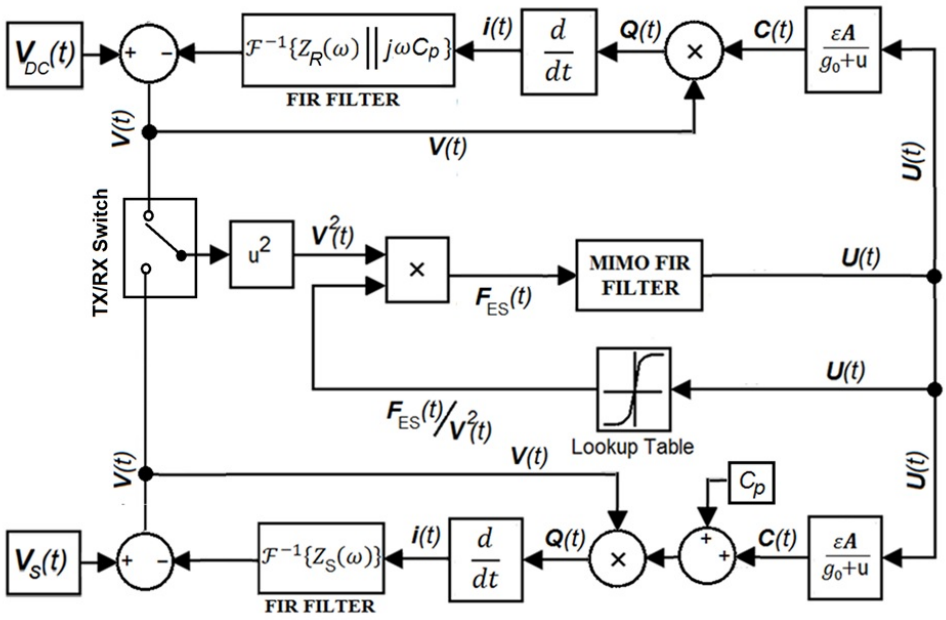

Figure 66: Large Signal SIMULINK Model for Pulse-Echo Mode

In case of a hard wall boundary which may be tilted as compared to the plane containing the CMUT array, proper geometrical modifications can be made to Equations (68) and (69). Directivity pattern can be obtained given that the distance between the transducer and the hard wall boundary is large enough. By investigating the time domain pressure fields propagating back and forth between the array and the hard wall, one can also evaluate the reflectivity of the CMUT array accurately for different electrical loading conditions.

4.2.1 Model Verification

For the pulse-echo model verification purposes, the example circular CMUT is placed 20 μm away from a parallel wall interface and the time domain the mean membrane displacement of the CMUT is calculated and compared with COMSOL simulations. It should be noted that the model is capable of simulating a plane reflector located at an arbitrary distance from the CMUT. However, 20 μm is selected in order to keep the FEA model size small, since the fluid domain between the wall and the CMUT must be meshed fine enough to accurately model the wave propagation within the immersion medium.

The CMUT is actuated with a 25 V Gaussian pulse with 8 ns standard deviation and the source impedance, which acts as the load impedance in the receive mode, is selected as 50 kΩ in the simulations. To clarify the effect of the hard wall in the calculations, the same CMUT is also simulated when it is immersed in a semi-infinite medium and when a soft wall reflector is present 20 μm away from the CMUT. Figure 67 presents the time and frequency domain mean membrane displacements for the same excitation signal, in semi-infinite medium, and for hard wall and soft wall cases. In all cases, model results show agreement with COMSOL calculations within 1 dB for most of the spectrum up to 4 times the center frequency of the device, validating the accuracy of the presented approach.

4.3 Model Application: Simulation of a Partial Dual-Ring Array

In practice transducer arrays are composed of finite number of elements and modeling of a whole array is computationally expensive, even infeasible for many cases when the number of elements in the array is large. Moreover, the overall imaging performance of a transducer is a function of the convolution of receive and transmit arrays, therefore the imaging system must be modeled and optimized as a whole, including electrical termination conditions. In this section, a 25 MHz partial dual-ring CMUT array is modeled as a case study highlighting the complex interactions of the transmit and receive terminations and dc bias levels. The modeled dual-ring array is shown in Figure 68. The array has 11 transmit (outer ring)

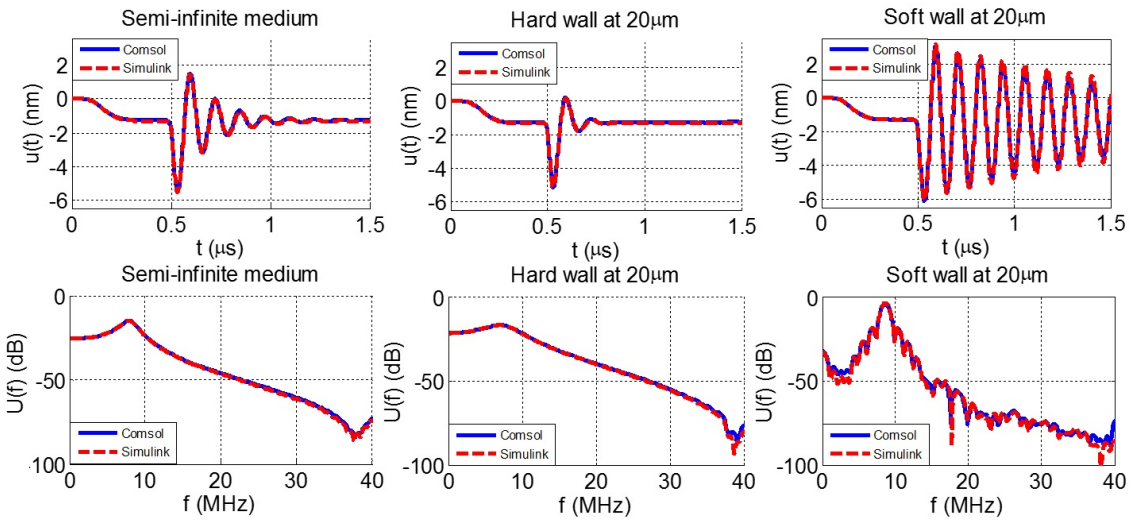

Figure 67: Mean membrane displacements and its spectra in semi-infinite fluid, in the presence of a hard wall 20 μm away from the transducer and in the presence of a soft wall 20 μm away when the CMUT is terminated with a 50 kΩ resistor

and 11 receive (inner ring) elements where each array element is composed of 4 25 μm $\times$ 25 μm membranes with 80% electrode coverage. The magnitude of the input impedance of the transimpedance amplifiers connected to the receive elements is $\sim$10 kΩ. The array is modeled in water and the pulse-echo response is calculated for the water-air interface 1 cm away from the array. The mesh size for the BEM formulation is 1.67μm. The calculation of the model parameters up to 100 MHz with a frequency resolution of 50 kHz (20 μs time response calculation) takes approximately 5 hours via parallel computing with 20 computing nodes in a high performance computing cluster each utilizing 5 processors and 256 GB physical memory in MATLAB environment. Note that the computation time is directly proportional to the number of processors and the frequency resolution required for the desired output time signal duration. After calculation of the model parameters, the time-domain SIMULINK model calculates the received signals from the water-air interface for the given drive signals for each electrode patch in the array and the electrical terminations. The simulation takes $\sim$15 minutes to calculate the array response for 20 μs simulation time with 5 ns time step for any input signal, gap thickness, transmit/receive electronics combination using a desktop computer with an Intel i5 processor running at 3 GHz and 16 GB of RAM.

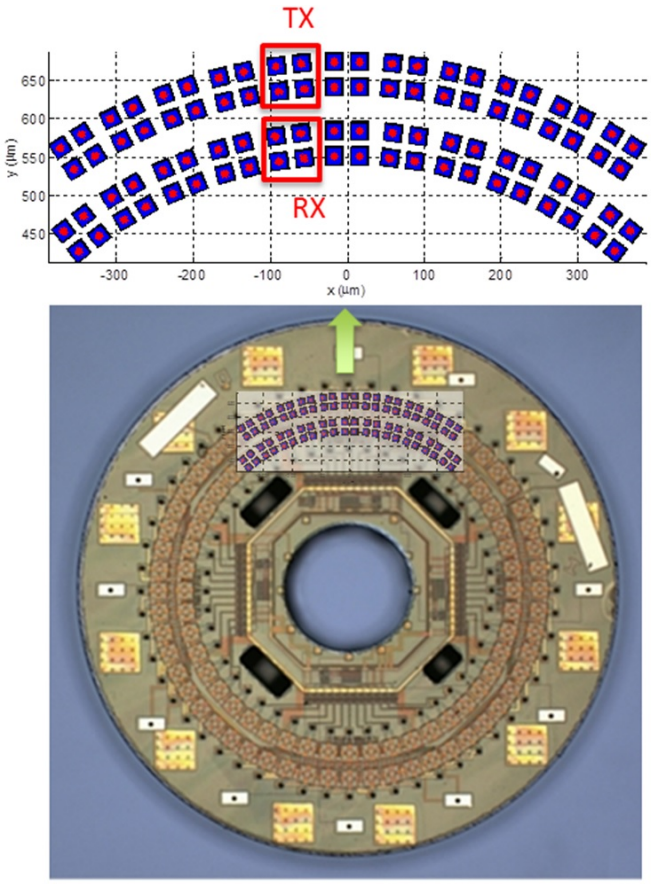

Figure 68: Modeled dual-ring array for Forward Looking IVUS

In the dual-ring array simulations dc bias applied to the transmit ring is selected as 15 V and the drive pulse amplitude is selected as 25 V. The applied signal to the transmit ring is shown in Figure 69 where the standard deviation of the Gaussian pulse is 7 ns. It should be noted that the DC bias is applied to the CMUT array using a smooth function in order to avoid additional membrane dynamics due application of the dc bias. Selected values are based on the fabricated CMUT-on-CMOS array with on-chip 25 V pulsers and 40 V dielectric breakdown voltage where the array details are presented in [105]. The collapse voltage of the CMUTs is 39 V.

The model results are first compared to experimental data for validation of the calculations. The highlighted elements in Figure 68 are used as the transmitter and the receiver in the experiment and simulations. The experimental device has on-chip pulsers and there is

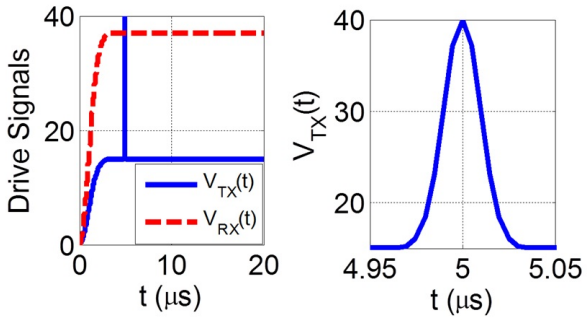

Figure 69: Drive signals applied to the receive and transmit rings for dual-ring array simulations

no access to the electrical transmit pulse. Therefore an approximate pulse given in Figure 69 is applied to the transmitting element in the simulations. Figure 70 presents the experimental and calculated received voltage outputs given the TIA gain of 300 kV/A from the water-air interface 1 cm away from the array. Considering CMUT and CMOS fabrication uncertainties, unaccounted reflections from the wire-bonds in the experiment and the unavailability of the experimental excitation pulse the results match fairly well validating the calculations.

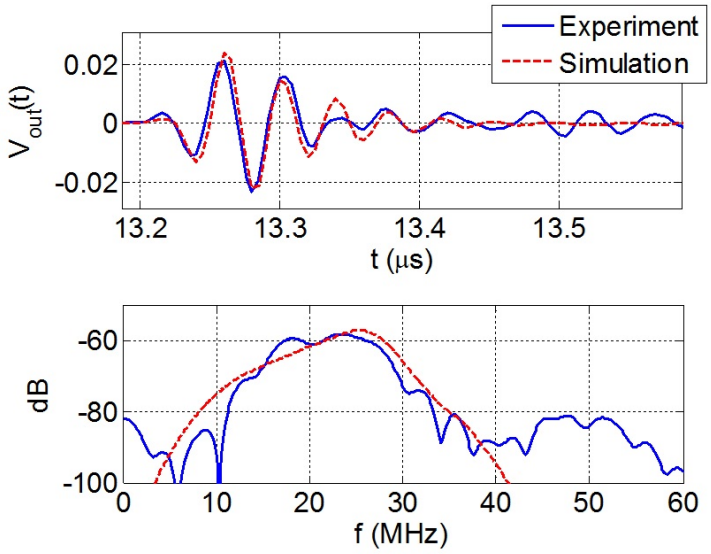

Figure 70: Experimental and simulated received signals from the water-air interface 1 cm away from the CMUT array

For an example optimization study the output current of the receive element is calculated for three cases with different receive DC bias and receive termination conditions. In the first case, the receive ring is biased to 95% of the collapse voltage (37 V) and the magnitude of the receive amplifier input impedance is 10 kΩ (solid, blue). The dc bias is applied to the receive ring using a smooth function similar to the transmit ring, where the applied signal is shown in Figure 69 as a function of time. In the second case the receive ring is biased to 77% of the collapse voltage (30 V) (dashed, red). As the third case (dashed, black), the receive ring is biased to 95% of the collapse voltage (37 V) and the electrical boundary termination is set as short circuit. The time domain output current signals are given in Figure 71 for three separate cases. The output current for each case is composed of three parts as labeled in the plot. First, current flows into CMUT from the source as charge builds up on the CMUT capacitance while the dc bias to the receive ring is being applied. Second, the receive element responds to the radiated pressure from the transmit element and outputs a signal due to the acoustic crosstalk (Figure 71(b)). And finally the receive element responds to the echo signal reflected from the water-air interface (Figure 71(c)). Figure 71(e) presents the spectra of the received echo signals for the simulated cases. Simulation results suggest that the two-way gain and bandwidth are both improved as the receive ring is biased close to collapse and for short circuit receive termination condition compared to the first case. The example case study demonstrates the potential of the modeling approach for rapid iterative optimization of CMUT arrays where FEA accuracy is achieved in a computationally efficient manner. Note that any change in these parameters would require a separate transient three-dimensional FEA of this partial array, which is practically infeasible.

4.3.1 Crosstalk Analysis

Direct analysis of acoustic crosstalk within the array can be carried out using the simulation results as the model outputs the transient dynamics of the whole simulated array elements. The dynamics of the array are investigated when the highlighted transmitter in Figure 72 is

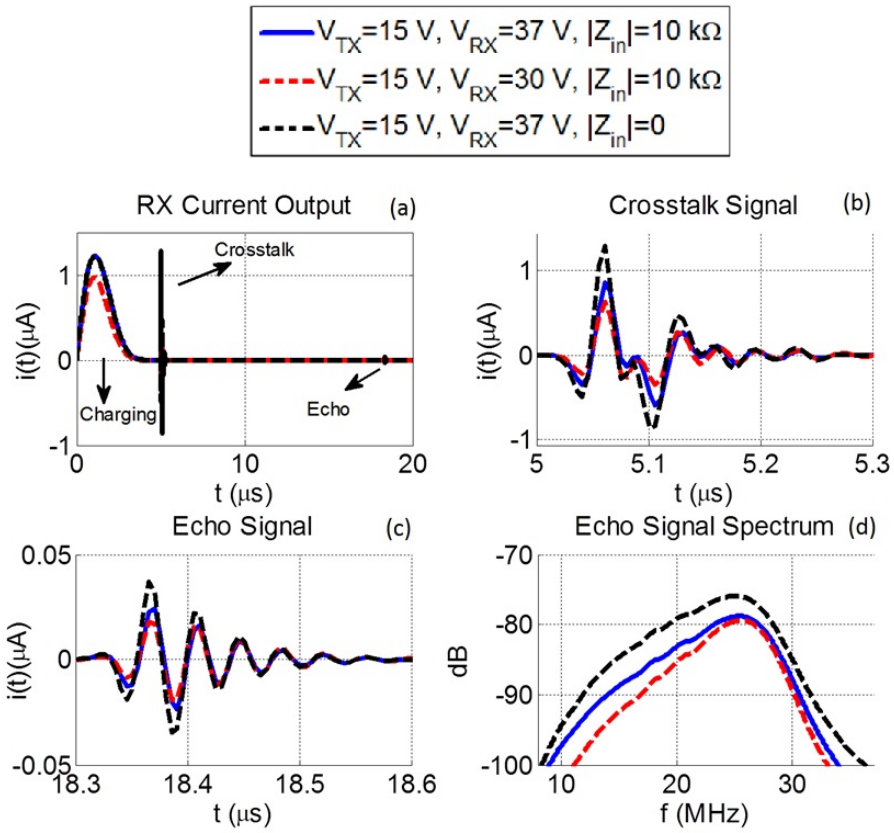

Figure 71: Time and frequency domain output currents of the receiving element when the modeled dual-ring array is simulated in pitch-catch operation utilizing the water-air interface 1 cm away from the array for different receive ring bias and electrical termination conditions

excited with the short pulse given in Figure 69 and the response of the highlighted receivers caused by acoustic crosstalk are calculated. Figure 73 presents the mean time domain displacements of the transmitting element and mean displacements of four elements in the receive ring. In the operation band of the transducer, 30 MHz, the displacement of the closest receive element to the transmitter is 25 dB below the transmitter displacement for the array under consideration. Moreover, the spectrum of the displacements alter for the receiver elements farther away the transmitter as it can be observed in the simulation results, which suggests a propagating surface wave on the array surface.

To investigate the propagating surface wave, the current outputs of the receiver elements caused by the acoustic crosstalk and the received echoes are compared. Figures 74 and 75

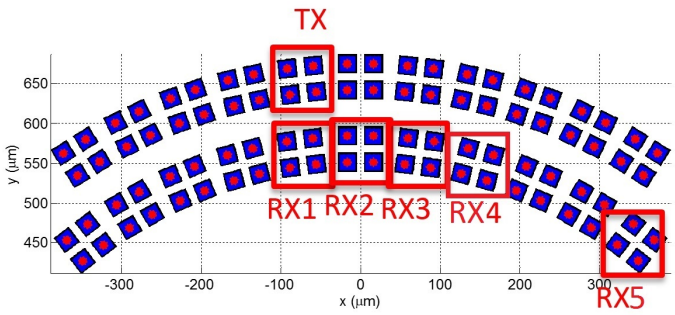

Figure 72: Modeled dual-ring array for crosstalk analysis

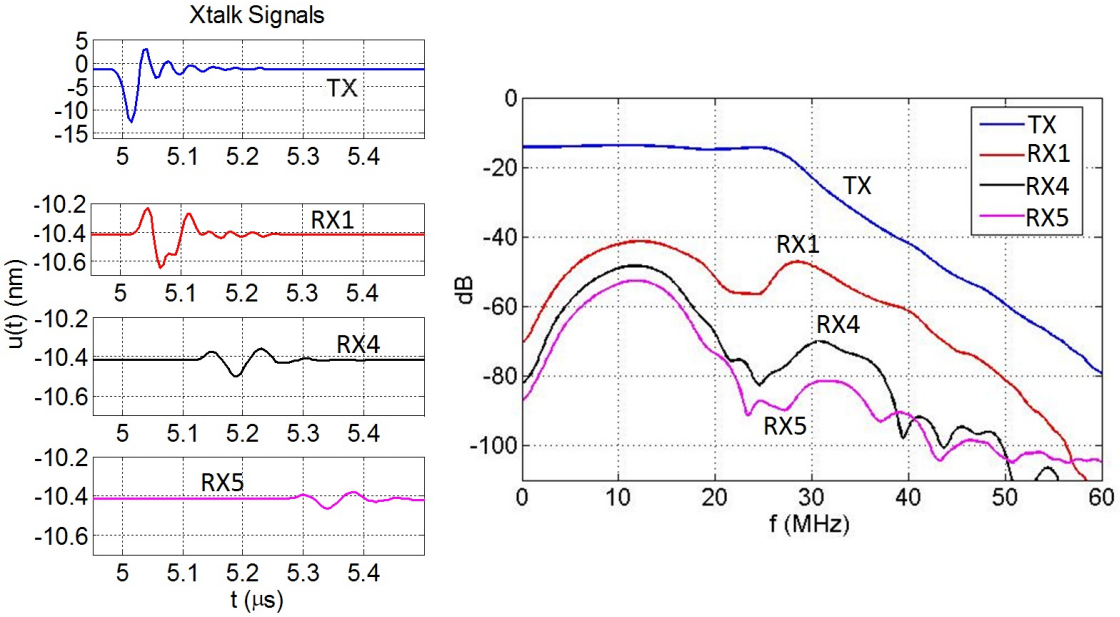

Figure 73: Time and frequency domain displacements of the transmitter and the receive elements caused by acoustic crosstalk

present the crosstalk and echo signals received by the four receivers highlighted in Figure 72. In Figure 74 it can be seen that the crosstalk signal has two frequency components, one centered at 14 MHz and the second component is at around 30 MHz. The 30 MHz component attenuates quickly as the wave propagates on the array surface compared to the 14 MHz component. The echo signals Figure 75 are same for all four receivers and centered at 25 MHz. This is expected as the the distances between the receiver elements are small compared to the distance between the elements and the water-air interface (1 cm).

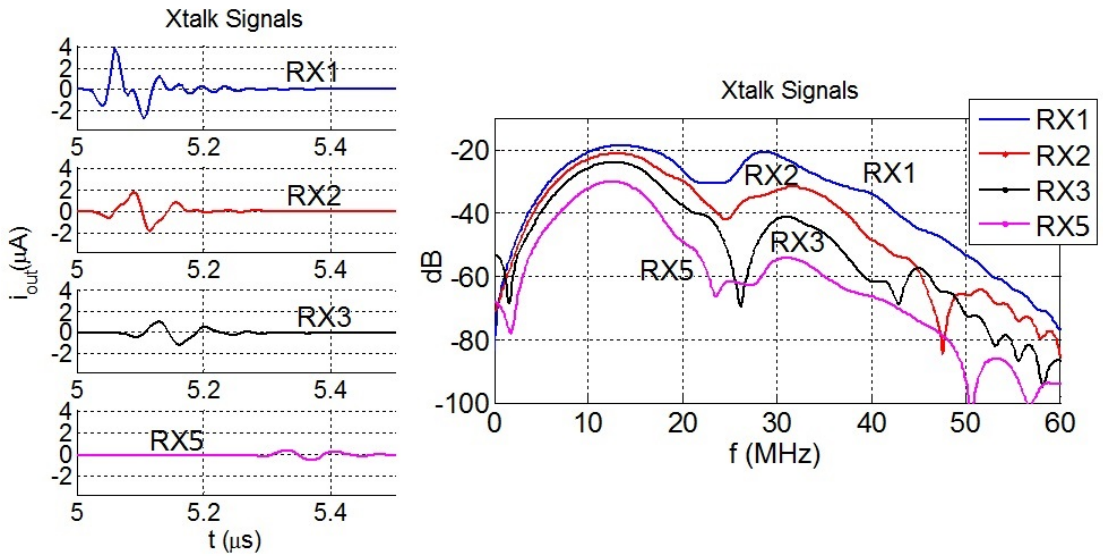

Figure 74: Time and frequency domain output currents of the the receive elements caused by acoustic crosstalk

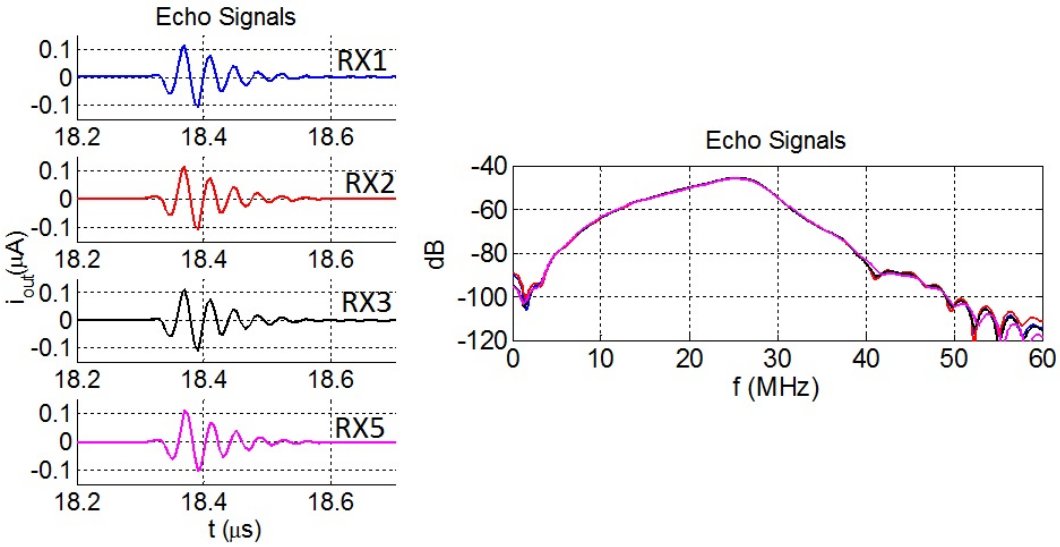

Figure 75: Time and frequency domain output currents of the the receive elements caused by the received echo from the water-air interface

4.3.2 Investigation of Dual Mode Side- and Forward-Looking Capability

The simulation results given in Section 4.3.1 suggest that for the particular array under investigation, a 14 MHz side propagating wave and a 25 MHz forward propagating wave is generated when the transmitter element is excited. This observation suggests that the

dual-ring array can be utilized for a dual side- and forward-looking imaging array where frequency selective side-looking imaging can be done at 14 MHz and the forward-looking image can be constructed at 25 MHz. Initial imaging experiments investigating the dual side- and forward-looking capability of the dual-ring array was conducted by fellow Dr. Degertekin group members Dr. Coskun Tekes and Mr. Toby Xu. The experimental setup is presented in 76 where 4 wires are placed around the CMUT array as the side-looking imaging targets and a single wire is placed in front of the array as the forward-looking imaging target.

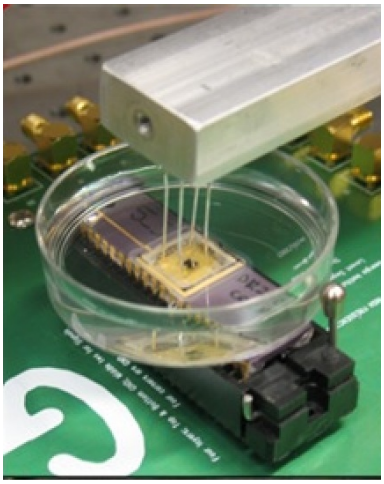

Figure 76: The experimental setup utilizing a dual-ring CMUT array for dual mode side- and forward-looking imaging capability investigation

The radio frequency (RF) received echo signals from the side and forward wires and their respective spectra are given in Figure 77. The side wire signal is centered at 11 MHz and the forward wire signal is centered at 22 MHz. The dip at 22.5 MHz in the front wire signal is due to ringing in the substrate [106], which is not considered in the simulations. The experimental RF data confirms the simulation results suggesting the possibility of dual mode side- and forward- looking imaging. Frequency selective synthetic aperture volumetric images were constructed using the RF data. For the side-looking image, the RF data is bandpass filtered centered at 11 MHz and for the forward-looking image, the

RF data is bandpass filtered centered at 22 MHz. The constructed volumetric and cross-sectional images are shown in Figure 78, demonstrating the dual-mode imaging capability of the dual-ring array and verifying the crosstalk analysis based on the simulation results discussed in Section 4.3.1.

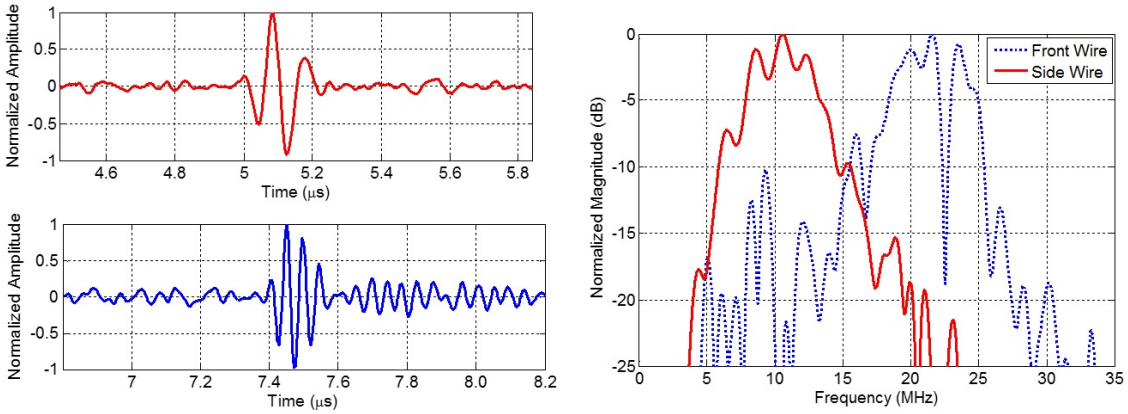

Figure 77: Time and frequency domain received signals from the forward-looking imaging target wire and the side-looking imaging wires

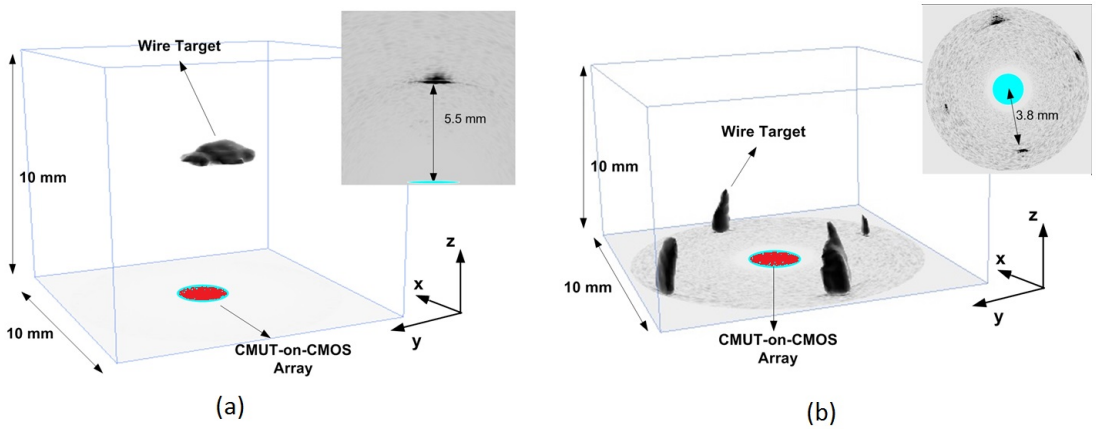

Figure 78: Frequency selective synthetic aperture volumetric images: Forward-looking image constructed at 22 MHz and side-looking image constructed at 11 MHz

CHAPTER 5

NONLINEAR IMAGING METHODS FOR CMUTS

In this chapter, a novel method based on multiple transmit firings with inter-pulse phase modulation for using CMUTs for nonlinear imaging effectively. For contrast agent imaging, it is shown that the summation of the received signals from four transmit events with $0, \pi/2, 3\pi/2, \pi$ rad phase shift respectively eliminates the contribution from both CMUT and tissue nonlinearities, resulting in nonlinear microbubble response only in the final received waveform. The method is valid in the whole non-collapsed regime where gap dependency of the electrostatic force does not need to be neglected. Additionally, it is demonstrated that for a gap feedback linearized CMUT, pulse-inversion imaging can be implemented by subharmonic excitation with no dc bias and firing two consecutive pulses with $\pi/2$ phase shift.

First, we show that the CMUT dynamics obey the power series relation in with complex coefficients for harmonic excitation using the experimentally verified large signal CMUT array model presented in Chapter 3. Next simulation results for the four pulse phase modulation and pulse inversion for linearized CMUT scenarios are given. Finally, initial experimental results using an example CMUT are presented validating the potential applicability of the proposed methods to nonlinear imaging with CMUTs.

5.1 Power Series Description of Nonlinear CMUT Behavior

To achieve transmit pressure levels comparable to piezoelectric transducers, CMUT arrays must be operated close to their physical limits. This requires large signal operation where the electrostatic nonlinearities cannot be neglected [57]. Therefore accurate prediction and understanding of nonlinear CMUT behavior is essential. As a first order analysis in vacuum neglecting fluid loading, CMUT operation is described by a lumped spring, mass and

parallel-plate capacitor model [39]

$$m_{ps}\frac{d^2x(t)}{dt^2} + k_{ps}x(t) = \frac{\varepsilon_0 A}{2}\frac{V^2(t)}{(g_0 - x(t))^2}, \tag{70}$$

where m_{ps} is the lumped membrane mass, k_{ps} is the spring constant, ε_0 is the dielectric constant, A is the capacitor area, g_0 is the parallel-plate gap at rest, $x(t)$ is the instantaneous displacement and $V(t)$ is the electrical actuation signal as a function of time. Equation (70) is nonlinear and an analytical solution does not exist. Therefore, small-signal and large-signal behavior of the nonlinear CMUT behavior is analyzed seperately in the next subsections.

5.1.1 Small-signal Behavior

If $x(t)$ is small compared to the gap, Equation (70) can be linearized as

$$m_{ps}\frac{d^2x(t)}{dt^2} + k_{ps}x(t) \approx \frac{\varepsilon_0 A}{2}\frac{V^2(t)}{g_0^2}, \tag{71}$$

where the gap dependency of electrostatic force is dropped. For harmonic excitation, $V(t) = V_{DC} + V_{AC}\cos(\omega_0 t)$, Equation (71) becomes

$$m_{ps}\frac{d^2x(t)}{dt^2} + k_{ps}x(t) \approx \frac{\varepsilon_0 A}{2g_0^2}\left(\frac{V_{AC}^2}{2} + V_{DC}^2 + 2V_{DC}V_{AC}\cos(\omega_0 t) + \frac{V_{AC}^2}{2}\cos(2\omega_0 t)\right). \tag{72}$$

Using superposition and phasor notation the solution of (72) can be described as

$$\begin{aligned} x(t) &= \Re\{\hat{x}(t)\}, \\ \hat{x}(t) &= c_0 + c_1 V_{AC} e^{j\omega_0 t} + c_2 V_{AC}^2 e^{j2\omega_0 t}. \end{aligned} \tag{73}$$

Here $\Re$ is the real part operator, $\hat{x}(t)$ is the analytic representation of $x(t)$, such that $\hat{x}(t) = x(t) + j\mathcal{H}\{x(t)\}$ where $\mathcal{H}$ is the Hilbert transform operator and c_n are the coefficients of the complex power series relating the drive signal $V_{AC}e^{j\omega_0 t}$ and the analytic output signal $\hat{x}(t)$. By comparison of Equations (72) and (73) it can be observed that for given excitation frequency ω_0, c_0 and c_2 are constant and c_1 is directly proportional to V_{DC}. Analysis of (73) yields to multiple observations which are valid for small displacements only. First, when

the CMUT is operated in small displacement regime, only the second harmonic is generated additional to the fundamental term and the second harmonic term can be neglected if $V_{AC} \ll V_{DC}$, suggesting linear device operation [39]. Another observation is linear proportionality of the fundamental term to V_{DC} for constant V_{AC}. By exploiting this observation the fundamental components amplitude can be adjusted via tuning dc bias while the second harmonic amplitude is kept constant [47]. Moreover, if $V_{DC} = 0$, the only the second harmonic term is generated. By exciting the CMUT at half the desired operation frequency with no dc bias, desired linear operation can be achieved. The power series description in (73) can be generalized to the operation of immersion CMUT since the radiated pressure, hence the fluid loading is a linear function of CMUT membrane displacement. For small signal operation, the transmitted pressure at an arbitrary point would be in the form of

$$\hat{p}(t) = a_0 + a_1 V_{AC} e^{j\omega_0 t} + a_2 V_{AC}^2 e^{j2\omega_0 t} \tag{74}$$

where the instantaneous pressure is $p(t) = \Re\{\hat{p}(t)\}$ and a_n are the complex coefficients.

5.1.2 Large-signal Behavior

To investigate if the large-signal CMUT behavior obeys a higher order power series relation between voltage input and pressure output at an arbitrary point in the immersion medium, the MATLAB/SIMULINK based nonlinear CMUT array model presented in Chapter 3 is utilized. A single CMUT element consisting of 16 square membranes in 4×4 array formation is modeled with given parameters in Table 5. The collapse voltage of the modeled CMUT is 14 V. The normalized spectrum of the radiated pressure 1 mm away from the element for 10 V dc bias and 6 V, 30 ns Hann pulse is shown in Figure 79. For harmonic analysis, the fundamental frequency is chosen as 5 MHz so the harmonics up to fourth are within the 6 dB frequency band of operation.

The modeled CMUT is driven with harmonic drive signal $V_{AC}\cos(\omega_0 t)$ and the pressure 1 mm away from the transducer is calculated as $p(t)$. The analytical representations of input signal and output pressure are then as $\hat{v}(t) = V_{AC} e^{j\omega_0 t}$ and $\hat{p}(t) = p(t) + j\mathcal{H}\{p(t)\}$. M^{th} order

Table 5: Simulated CMUT Parameters

Membrane dimensions	$35\mu\text{m} \times 35\mu\text{m} \times 1.65\mu\text{m}$
Electrode coverage	$25\mu\text{m} \times 25\mu\text{m}$
Gap	50nm
Array pitch	$45\mu\text{m}$
Electrode isolation thickness	100nm
Isolation dielectric constant	15
Membrane Density, Poisson's ratio and Young's modulus	2040kg/m^3, 0.22, 110GPa

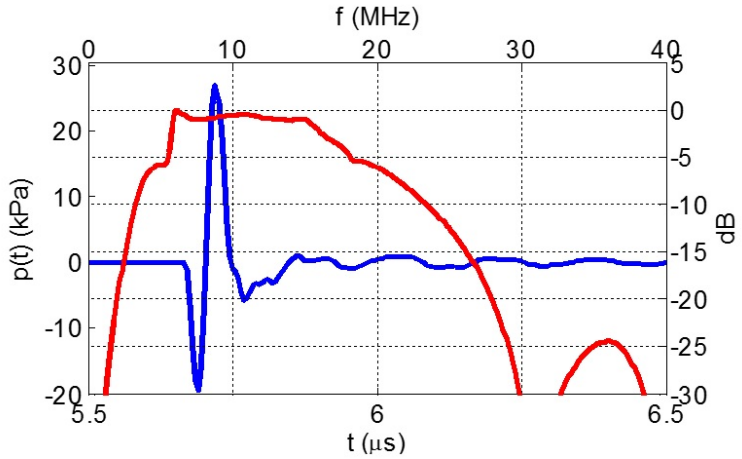

Figure 79: Impulse response and frequency response of the simulated CMUT

power series relating n^{th} sample of the input signal $\hat{v}(t)$ and the n^{th} sample of output signal $\hat{p}(t)$ is defined as

$$\hat{p}_n = a_0 + a_1\hat{v}_n + a_2\hat{v}_n^2 + a_3\hat{v}_n^3 + \ldots + a_M\hat{v}_n^M + \epsilon_n \tag{75}$$

where $a_0, a_1, \ldots, a_M$ are the complex coefficients and ϵ_n is the error term. For all samples in the waveform, Equation (75) can be represented in matrix format such that

$$\vec{\hat{p}} = \mathbf{V}\vec{a} + \vec{\epsilon} \tag{76}$$

where

$$\vec{\hat{p}} = \begin{bmatrix} \hat{p}_1 \\ \hat{p}_2 \\ \vdots \\ \hat{p}_N \end{bmatrix}, \mathbf{V} = \begin{bmatrix} 1 & \hat{v}_1 & \hat{v}_1^2 & \dots & \hat{v}_1^M \\ 1 & \hat{v}_2 & \hat{v}_2^2 & \dots & \hat{v}_2^M \\ \vdots & \vdots & \vdots & \ddots & \vdots \\ 1 & \hat{v}_N & \hat{v}_N^2 & \dots & \hat{v}_N^M \end{bmatrix}, \vec{a} = \begin{bmatrix} a_0 \\ a_1 \\ \vdots \\ a_M \end{bmatrix}, \vec{\epsilon} = \begin{bmatrix} \epsilon_1 \\ \epsilon_2 \\ \vdots \\ \epsilon_N \end{bmatrix}. \tag{77}$$

The estimated coefficient vector $\vec{a}_{est}$ that minimizes the error $\vec{\epsilon}$ is calculated by least squares such that

$$\vec{a}_{est} = (\mathbf{V}^T\mathbf{V})^{-1}\mathbf{V}^T\vec{\hat{p}}. \tag{78}$$

Finally, the pressure signal is reconstructed using the estimated power series coefficients and the input signal such that $\vec{p}_{fit} = \mathbf{V}\vec{a}_{est}$.

Two separate cases are modeled to verify that CMUT dynamics obey the postulated power series relationship. First the case is for $V_{DC}, V_{AC} \ll V_{collapse}$ where the pressure output is expected to be a second order relation in the form of Equation (74).The CMUT under investigation is simulated for V_{DC}=0.1 V, V_{AC}=0.1 V and f_0=5 MHz. The time domain pressure at 1 mm away from the CMUT is calculated and power series coefficients relating the input signal and output pressure are estimated via Equation (78) for orders $M = 1, 2, 3, 4, 5$. The simulation results are presented in Figure 80. The calculated pressure and the power series fit for $M = 5$ is given in Figure 80(a) with their respective spectra in Figure 80(b). As discussed earlier, only the second harmonic is generated as the membrane displacement is small compared to the device gap. Figure 80(c) presents the Lissajous curve where the output pressure is plotted versus the input voltage for the simulation output and the power series fit. In the plot, the arrow shows the direction of time. It should be noted that the Lissajous curve would be an ellipse for linear operation. For the merit of the accuracy of the power series fit, the normalized error is defined as

$$error = 20\log\frac{(p - p_{fit})_{rms}}{p_{rms}}. \tag{79}$$

The normalized error as a function of the power series order M is presented in 80(d). As it can be observed in the plot, the power series converges at M=2 as expected, validating the small-signal form in Equation (74).

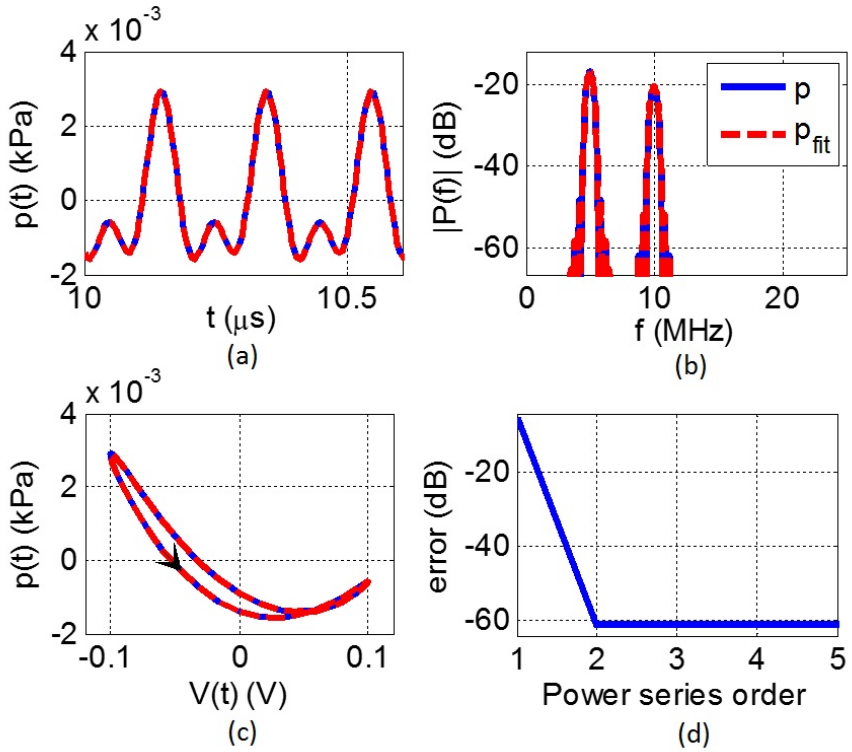

Figure 80: (a) Pressure output (solid) and the power series fit (dashed) for V_{DC}=0.1 V, V_{AC}=0.1 V (b) Spectra of the calculated pressure output and the power series fit (c) Lissajous curves for the pressure output and the power series fit (d) Fit error as a function of power series order

In the second case the CMUT is simulated with V_{DC}=7 V, V_{AC}=7 V and f_0=5 MHz. In this scenario the CMUT is driven close to collapse where maximum peak-to-peak mean membrane displacement in the array is ~18 nm and V_{DC}=7 V, V_{AC}=8 V results in membrane collapse. The simulation and power series fit results are given in Figure 81. The spectrum of the transmitted pressure in Figure 81(b) shows that higher order harmonics are also generated in addition to the second harmonic, meaning that the gap dependence of the electrostatic force acting on CMUT membrane cannot be neglected and the small-signal analysis is not valid in this operation regime. The power series converges at $M = 7$, validating that the large-signal CMUT behavior obeys the power series relationship between the input voltage signal and output pressure.

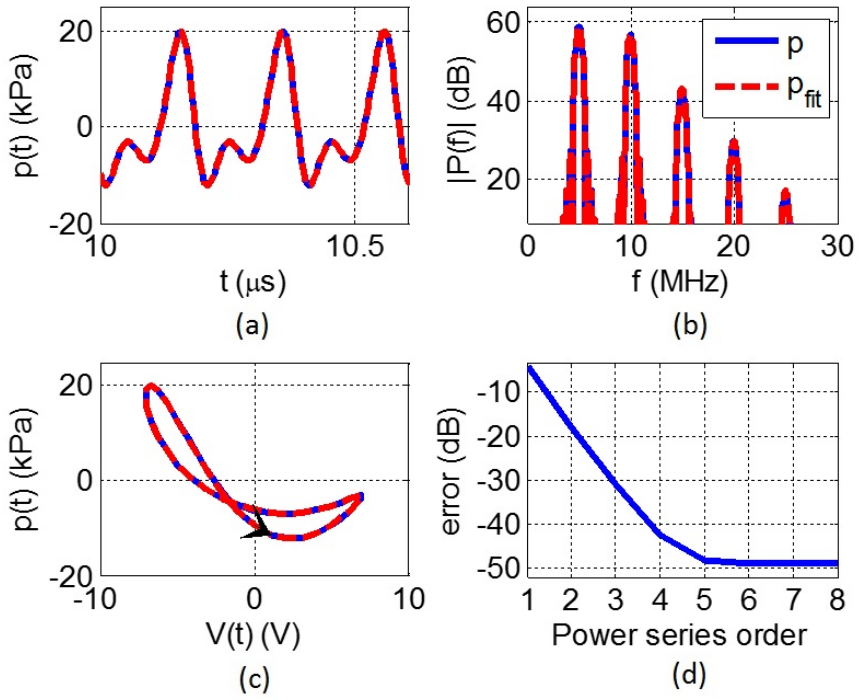

Figure 81: (a) Pressure output (solid) and the power series fit (dashed) for V_{DC}=7 V, V_{AC}=7 V, f_0=5 MHz. (b) Spectra of the calculated pressure output and the power series fit (c) Lissajous curves for the pressure output and the power series fit (d) Fit error as a function of power series order

5.2 Phase Modulation Method for Contrast Agent Imaging

The power series description relating the CMUT drive signal and the pressure output provides insight to nonlinear CMUT response to harmonic excitation. For the harmonic input signal $V_{AC}e^{j(\omega_0 t+\phi)}$ the pressure at an arbitrary point in the immersion fluid can be approximated as

$$\hat{p}(t) \approx \sum_{n=0}^{\infty} a_n V_{AC}^n e^{j(n\omega_0 t+n\phi)}. \tag{80}$$

As the CMUT is a time-invariant system, the power series coefficients a_n are functions of V_{AC}, V_{DC} and ω_0 and independent of the phase of the excitation signal, ϕ. If the phase of the drive signal is shifted by ϕ, the second harmonic shifts by 2ϕ, the third harmonic by 3ϕ, and so on.

Via Equation (80) it can be shown that by firing N consecutive pulses where the respective phase of m^{th} firing is $\phi_m = 2(m-1)\phi/N$ and adding the resulting pressure waveforms, the contribution from the CMUT can be eliminated for all harmonics except the N^{th} and harmonics of the N^{th} harmonic. For each drive signal the corresponding pressure output is described by Equation (80) such that

$$\begin{aligned}
\hat{v}_1(t) = V_{AC}e^{j(\omega_0 t)} &\rightarrow \hat{p}_1(t) \approx \sum_{n=0}^{\infty} a_n V_{AC}^n e^{j(n\omega_0 t)}, \\
\hat{v}_2(t) = V_{AC}e^{j(\omega_0 t - 2\pi/N)} &\rightarrow \hat{p}_2(t) \approx \sum_{n=0}^{\infty} a_n V_{AC}^n e^{j(n\omega_0 t - 2n\pi/N)}, \\
&\vdots \\
\hat{v}_N(t) = V_{AC}e^{j(\omega_0 t - 2(N-1)\pi/N)} &\rightarrow \hat{p}_N(t) \approx \sum_{n=0}^{\infty} a_n V_{AC}^n e^{j(n\omega_0 t - 2n(N-1)\pi/N)}.
\end{aligned} \tag{81}$$

In the presence of a linear reflector, the addition of N pressure waveforms yields to

$$\begin{aligned}
&\hat{p}_1(t) + \hat{p}_2(t) + \ldots + \hat{p}_N(t) \approx \\
&\qquad Na_N V_{AC}^N e^{j(N\omega_0 t)} + Na_{2N} V_{AC}^{2N} e^{j(2N\omega_0 t)} + Na_{3N} V_{AC}^{3N} e^{j(3N\omega_0 t)} + \ldots
\end{aligned} \tag{82}$$

where all harmonics except N^{th}, $(2N)^{th}$, $(3N)^{th}$, and so on, are eliminated. For a linear transducer only a_1 is nonzero therefore Equation (82) would be equal to zero, hence for a nonlinear microbubble reflector the result of the addition in Equation (82) would have solely the nonlinear response of the microbubbles. Within the given formulation pulse inversion is a special case of the proposed method where $N = 2$.

5.2.1 Simulations

To evaluate the presented phase modulation method the example CMUT modeled in Section 5.1.2 is simulated for a linear reflector, where the pressure 1 mm away from the CMUT is evaluated. The results of the method are compared to the bias modulation method proposed in [47]. The bias modulation method assumes that the electrostatic force acting on CMUT membranes is not dependent on the gap, resulting in the second order input output relationship given in Equation (74). As stated in Section 5.1.1, for a given excitation

frequency ω_0, a_0 and a_2 are constant and a_1 is directly proportional to V_{DC}. For constant V_{AC}, three transmitted pulses with respective dc biases of V_0, $2V_0$, $3V_0$ result in the pressure waveforms as follows:

$$\begin{aligned} V_{DC} = V_0 \rightarrow \hat{p}_1(t) &= a_0 + a_1 V_{AC} e^{j\omega_0 t} + a_2 V_{AC}^2 e^{j2\omega_0 t}, \\ V_{DC} = 2V_0 \rightarrow \hat{p}_2(t) &= a_0 + 2a_1 V_{AC} e^{j\omega_0 t} + a_2 V_{AC}^2 e^{j2\omega_0 t}, \\ V_{DC} = 3V_0 \rightarrow \hat{p}_3(t) &= a_0 + 3a_1 V_{AC} e^{j\omega_0 t} + a_2 V_{AC}^2 e^{j2\omega_0 t}. \end{aligned} \tag{83}$$

The contribution from CMUT is simply eliminated by addition, i.e. $\hat{p}_1(t)+\hat{p}_3(t)-2\hat{p}_2(t) \approx 0$.

The aforementioned bias modulation method is simulated for comparison purposes using the example CMUT under investigation for two cases, for small displacement regime and for large displacement regime. In all simulations the CMUT is driven with a 2 μs Hann windowed 5 MHz sine wave. First the CMUT is simulated with V_{AC}=0.2 V for small signal analysis and the results are given in Figure 82. Figure 82(a) presents the spectra of the transmitted waveforms for V_{DC}=0.1 V, 0.2 V, 0.3 V. As expected only the second harmonic at 10 MHz is generated, and the change in the second harmonic amplitude is less than 0.5% between the cases V_{DC1}=0.1V and V_{DC2}=0.3V. The amplitude spectrum of the sum signal $p_1(t) + p_3(t) - 2p_2(t)$ is given in Figure 82(b) where ~80 dB suppression for both the fundamental and second harmonic components is achieved. For the second case the CMUT is simulated in the large displacement region with V_{AC}=5 V. Output pressure spectra for the cases V_{DC1}=2.5 V, V_{DC2}=5 V and V_{DC3}=7.5 V are given in Figure 82(c). In this operation regime higher order harmonics are also generated in addition to the second harmonic, suggesting that the gap dependence of electrostatic force cannot be neglected and the second order relationship between the drive signal and output pressure is not valid. The second harmonic amplitude difference between the cases V_{DC1}=2.5 V and V_{DC3}=7.5 V is 43% (~3dB), showing that the second harmonic amplitude is dependent on the dc bias value. Figure 82(d) shows the amplitude spectrum of the sum signal $p_1(t) + p_3(t) - 2p_2(t)$ where ~20 dB suppression in the fundamental component and ~10 dB suppression in the second harmonic is achieved.

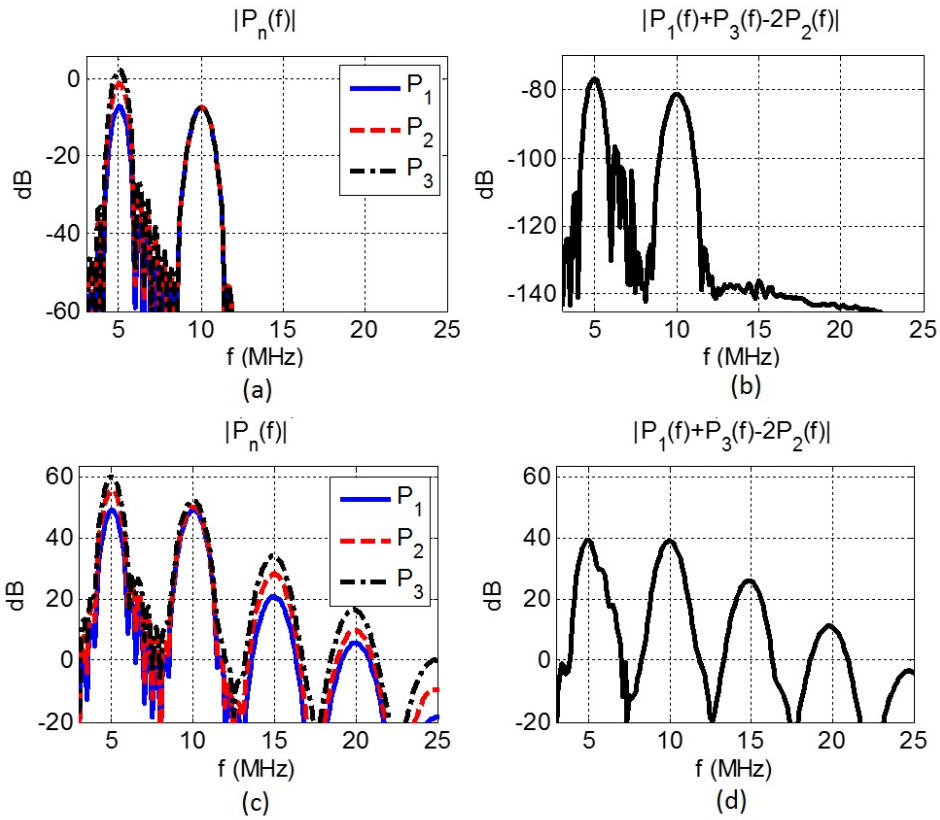

Figure 82: (a) Amplitude spectra of three bias modulated pressure outputs for small signal operation with V_{AC}=0.2 V, V_{DC1}=0.1 V, V_{DC2}=0.2 V and V_{DC3}=0.3V (b) Spectrum of $p_1(t) + p_3(t) - 2p_2(t)$ for the small signal case (c) Amplitude spectra of three bias modulated pressure outputs for large signal operation with V_{AC}=5V, V_{DC1}=2.5V, V_{DC2}=5V and V_{DC3}=7.5V (d) Spectrum of $p_1(t) + p_3(t) - 2p_2(t)$ for the large signal case

The presented phase modulation method is also simulated both in small and large displacement regimes for performance evaluation and the results are given in Figure 83. First the CMUT is simulated with V_{AC}=0.2V, V_{DC}=0.2V and the the output pressure is calculated for $N = 3$ with three transmit events having respective phases $\phi_1 = 0$, $\phi_2 = 2\pi/3$ and $\phi_3 = 4\pi/3$. Figure 83(a) shows the amplitude spectra for three transmit events and Figure 83(b) presents the amplitude spectrum of the sum signal $p_1(t) + p_2(t) + p_3(t)$ where first and second harmonic components are completely eliminated while the third harmonic component remains. For the large signal case the CMUT is driven with V_{AC}=7V and V_{DC}=7V. The amplitude spectra for three transmit events with respective phases $\phi_1 = 0$, $\phi_2 = 2\pi/3$ and $\phi_3 = 4\pi/3$ are given in Figure 83(c). The spectrum of the sum signal $p_1(t) + p_2(t) + p_3(t)$

is given in Figure 83(d) where the first and second harmonic components are completely eliminated while the amplitude of the third harmonic is raised $N = 3$ times (10 dB), obeying the formulation given in Equation (82).

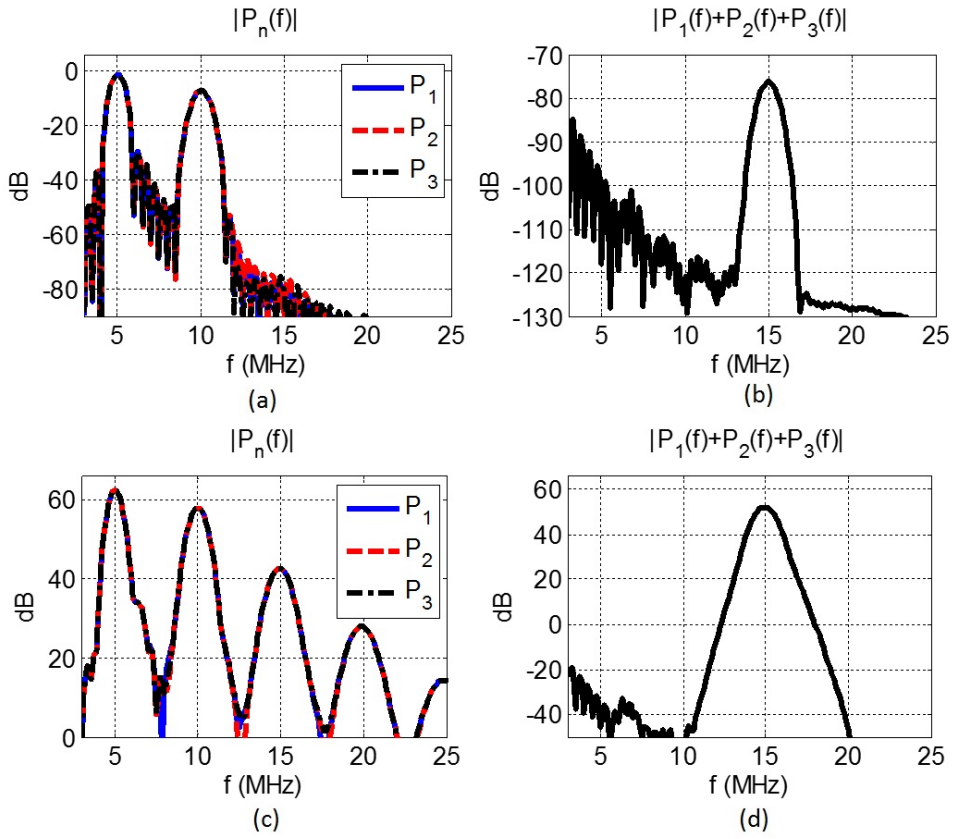

Figure 83: (a) Amplitude spectra of three phase modulated pressure outputs for small signal operation with V_{AC}=0.2V, V_{DC}=0.2V, $\phi_1 = 0$, $\phi_2 = 2\pi/3$ and $\phi_3 = 4\pi/3$ (b) Spectrum of $p_1(t)+p_2(t)+p_3(t)$ for the small signal case (c) Amplitude spectra of three phase modulated pressure outputs for large signal operation with V_{AC}=7V, V_{DC}=7V, $\phi_1 = 0$, $\phi_2 = 2\pi/3$ and $\phi_3 = 4\pi/3$ (d) Spectrum of $p_1(t) + p_2(t) + p_3(t)$ for the large signal case

The simulation results show that the presented phase modulation method completely eliminates the contribution of the CMUT in the returned echo for all harmonics except the kN^{th} harmonics where k is an integer. The approach is valid for both small signal and large signal operation in non-collapsed regime. In the presence of nonlinear contrast agent reflectors, the only components in the sum signal would be the contributions from the nonlinear contrast agent vibrations since the contrast agents response will not cancel out in the sum

signal [28]. Moreover, as the tissue obeys the power series relation, the contribution resulting from the nonlinear propagation in the tissue is also eliminated, potentially improving the agent-to-tissue ratio in the constructed nonlinear image [10, 27].

5.2.2 Experiments

For experimental verification of the phase modulation method a CMUT element composed of 400 $35\mu m \times 35\mu m$ membranes in 20×20 array formation is used to transmit and a broadband hydrophone (HGL-0200, Onda Corp., Sunnyvale, CA) is utilized to measure the transmitted pressure ~2.2 mm away from the CMUT. The collapse voltage of the CMUT is measured with a network analyzer as 40 V and the fractional bandwidth is 70% with center frequency of 11.5 MHz with the given impulse and frequency response in Figure 84.

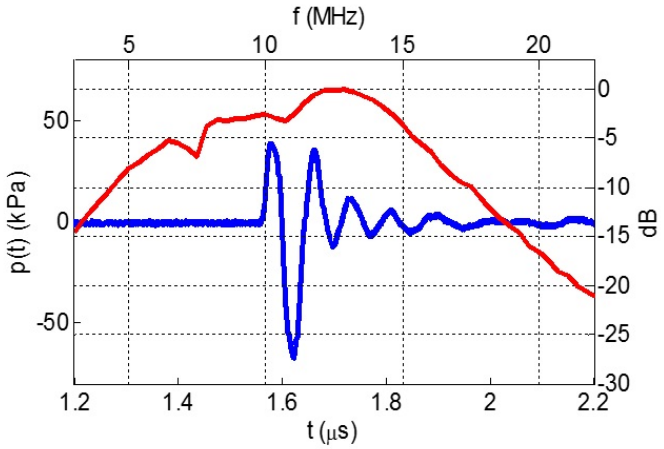

Figure 84: Impulse response and its amplitude spectrum of the CMUT used for the experiment

For the experiments, the fundamental frequency is selected as 5 MHz and the phase modulation method is implemented for $N = 4$ for elimination of the first three harmonics, where four consecutive pulses with respective phases $\phi_1 = 0$, $\phi_2 = \pi/2$, $\phi_3 = \pi$ and $\phi_4 = 3\pi/2$ is transmitted and recorded with the hydrophone. The phase modulation method is evaluated for two cases, for small signal and for large signal operation. First the CMUT is biased with V_{DC}=12 V (90% of collapse) and driven with 1.2 μs long Hann windowed 12 V

tone burst for small signal operation. The recorded transmitted pressure waveforms for four consecutive pulses are presented in Figures 85(a) and 85(b) with their respective spectra in Figure 85(c). As the electrostatic forces acting on CMUT membranes are minimally dependent on instantaneous gap in the small displacement regime, only the fundamental and second harmonic components are generated where the only nonlinearity source is the voltage square dependence. This is verified via the experimental results where the third harmonic is ~30 dB below the second harmonic level. The sum signal $p_1(t) + p_2(t) + p_3(t) + p_4(t)$ and its spectrum is given in Figure 85(d) where the first three harmonics are eliminated to the noise level as expected where there is an increase in the fourth harmonic amplitude as expected since $N = 4$. The results confirm the simulation results presented in Section 5.2.1 and validates the presented method in the small displacement regime.

For experimental evaluation in the large displacement regime, the CMUT is biased with V_{DC}=36 V (90% of collapse) and driven with 1.2 μs long Hann windowed 30 V tone burst. In this case the CMUT is driven in a regime where dynamic collapse and snapback occurs, introducing additional nonlinearities related to the pull-in phenomenon which were not covered in the simulation results. Figures 86(a) and 86(b) show the measured time domain pressure signals for four phase modulated transmit events and their respective amplitude spectra in Figure 86(c). The sum signal $p_1(t) + p_2(t) + p_3(t) + p_4(t)$ and its spectrum is given in Figure 86(d). Using the presented phase modulation method, the first, second and third harmonics are suppressed by ~45 dB, ~30 dB and ~20 dB respectively while the fourth harmonic amplitude is increased by 12 dB ($N = 4$ times) as expected. The results demonstrate the potential applicability of the method to nonlinear imaging with CMUTs operated in dynamic collapse-snapback operation regime.

5.3 Harmonic Imaging with Linearized CMUTs

The second order power series relationship between the excitation signal and the output pressure given in Equation (74) is valid for small signal operation . The same relationship

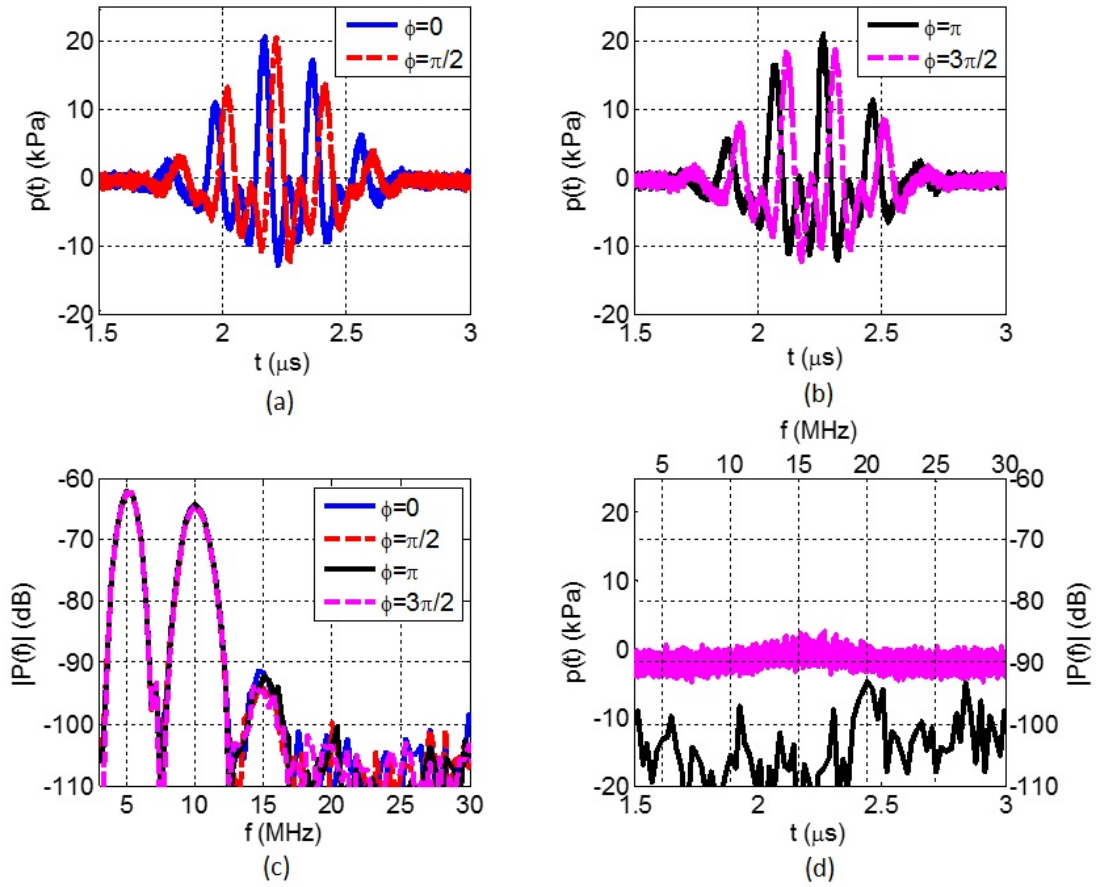

Figure 85: (a) Measured pressure signals for V_{DC}=12V, V_{AC}=12V, $\phi_1 = 0$, $\phi_1 = \pi/2$ (b) Measured pressure signals for V_{DC}=12V, V_{AC}=12V, $\phi_3 = \pi$, $\phi_4 = 3\pi/2$ (c) Spectra of the four phase modulated pressure output signals (d) The sum signal $p_1(t) + p_2(t) + p_3(t) + p_4(t)$ and its amplitude spectrum

is also valid for gap feedback linearized CMUT where gap dependence of electrostatic force is eliminated by instantaneous scaling of the drive voltage with gap as discussed in Section 2.4. If the CMUT without gap dependent electrostatic force is actuated without dc bias, i.e. V_{DC}=0 and at half the desired frequency, $\omega_0/2$, the transmitted pressure becomes

$$\hat{p}(t) = a_2 V_{AC}^2 e^{j\omega_0 t}, \tag{84}$$

where a_2 is constant for a given frequency. The modeled CMUT used in the simulations is evaluated for gap feedback linearization. The spectrum of the transmitted with pressure with and without gap feedback is given in Figure 87. In this case the gap feedback is

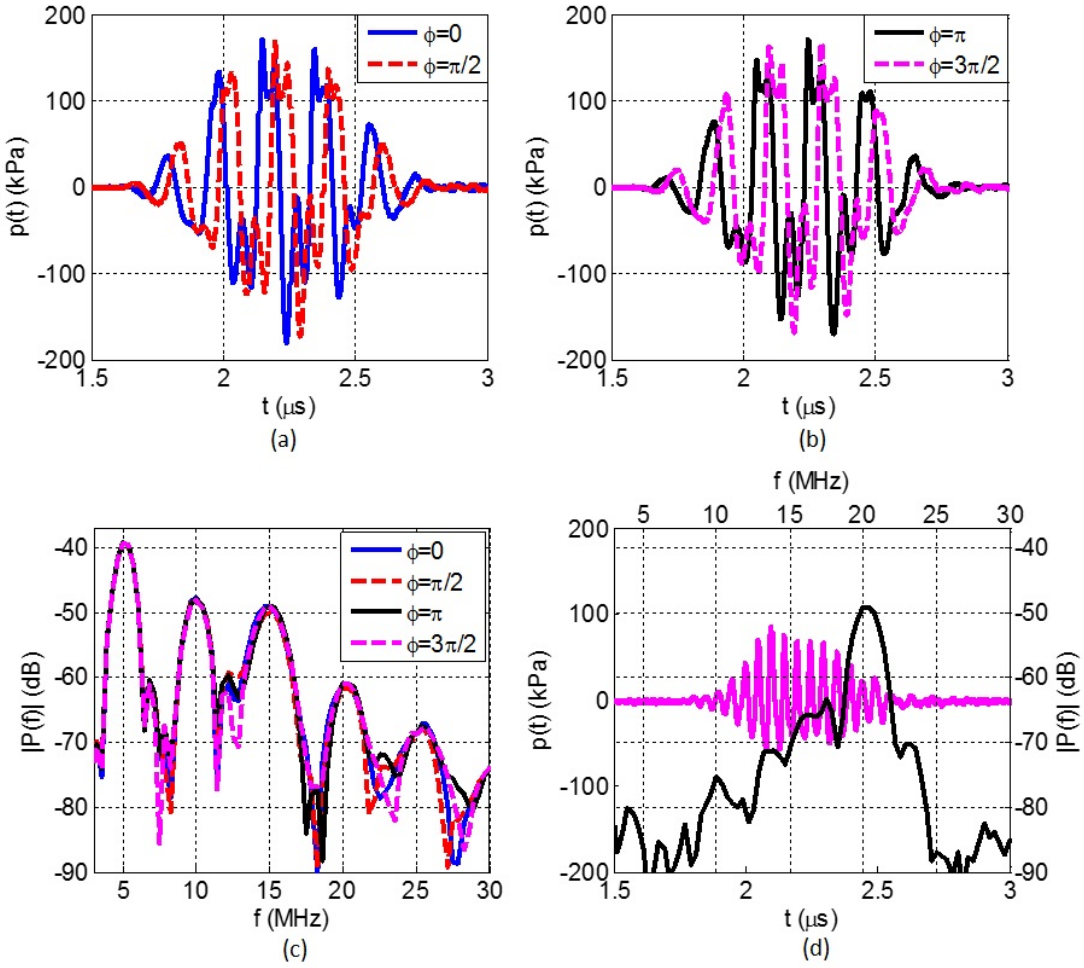

Figure 86: (a) Measured pressure signals for V_{DC}=36V, V_{AC}=30V, $\phi_1 = 0$, $\phi_1 = \pi/2$ (b) Measured pressure signals for V_{DC}=36V, V_{AC}=30V, $\phi_3 = \pi$, $\phi_4 = 3\pi/2$ (c) Spectra of the four phase modulated pressure output signals (d) The sum signal $p_1(t) + p_2(t) + p_3(t) + p_4(t)$ and its amplitude spectrum

implemented ideally, i.e. the input drive signal is scaled with the instantaneous mean gap for each membrane in the CMUT element and the feedback gain is chosen to achieve the same pressure amplitude at the fundamental frequency, ω_0=5 MHz.

The simulation results given in Figure 87 suggest that the harmonic distortion is not completely eliminated even though the gap feedback scheme is implemented ideally. This is caused by the nonlinearities associated with the curvature of the CMUT membranes, where the electrostatic force distribution within the membrane alters as the CMUT membrane goes under large displacements. The linearized CMUT is simulated for harmonic

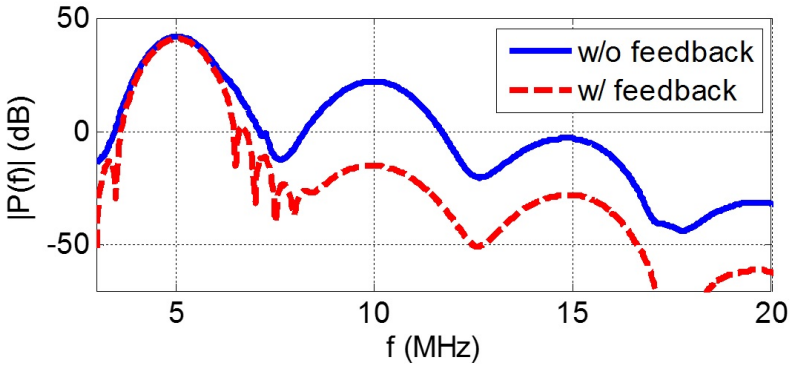

Figure 87: Spectra of the transmitted pressure with and without feedback where the same pressure amplitude is achieved at the fundamental frequency

imaging scenarios utilizing modified pulse inversion and amplitude modulation methods exploiting Equation (84) as follows.

5.3.1 Pulse Inversion and Amplitude Modulation

Pulse Inversion For pulse inversion, two consecutive pulses at half the desired frequency $\omega_0/2$ with a phase difference of $\pi/2$ result in two out-of-phase transmitted signals at the frequency ω_0 such that

$$\begin{aligned} \hat{v}_1(t) &= V_{AC} e^{j\frac{\omega_0}{2}t} \rightarrow \hat{p}_1 \approx a_2 V_{AC}^2 e^{j\omega_0 t}, \\ \hat{v}_2(t) &= V_{AC} e^{j(\frac{\omega_0}{2}t - \frac{\pi}{2})} \rightarrow \hat{p}_2 \approx a_2 V_{AC}^2 e^{j(\omega_0 t - \pi)}. \end{aligned} \tag{85}$$

In the presence of a linear reflector, simple addition of the two signals cancel each other, i.e. $\hat{p}_1(t) + \hat{p}_2(t) \approx 0$. Figure 88 presents the modified pulse inversion method where the contribution from CMUT is suppressed to ~50 dB below the fundamental component.

Amplitude Modulation A modified version of the amplitude modulation method is also applicable to the gap feedback linearized CMUT. Two amplitude scaled, in-phase consecutive pulses with drive signal amplitudes V_{AC} and AV_{AC} result in two transmitted pressure waveforms

$$\begin{aligned} \hat{v}_1(t) &= V_{AC} e^{j\frac{\omega_0}{2}t} \rightarrow \hat{p}_1 \approx a_2 V_{AC}^2 e^{j\omega_0 t}, \\ \hat{v}_2(t) &= A V_{AC} e^{j\frac{\omega_0}{2}t} \rightarrow \hat{p}_2 \approx A^2 a_2 V_{AC}^2 e^{j\omega_0 t}. \end{aligned} \tag{86}$$

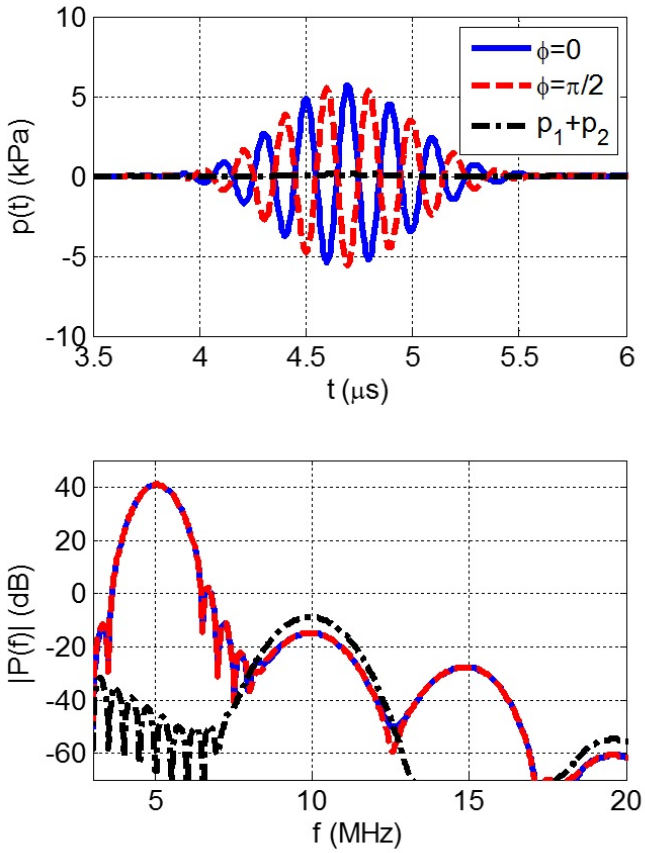

Figure 88: Two consecutive pressure outputs for two pulses with $\pi/2$ phase difference and their sum in time and frequency domains

according to Equation 84. In the presence of a linear reflector, simple subtraction of the scaled signals cancel each other, i.e. $\hat{p}_2(t) - A^2\hat{p}_1(t) \approx 0$. Figure 89 presents the modified amplitude modulation method where the contribution from CMUT is suppressed to ~45 dB below the fundamental component.

5.4 Conclusion

A phase modulation method for nonlinear imaging with CMUTs is presented. Using a large-signal CMUT model and an example simulated CMUT, it has been shown that the CMUT dynamics obey a power series description relating the input drive signal and the output pressure. This observation renders the phase modulation methods introduced to

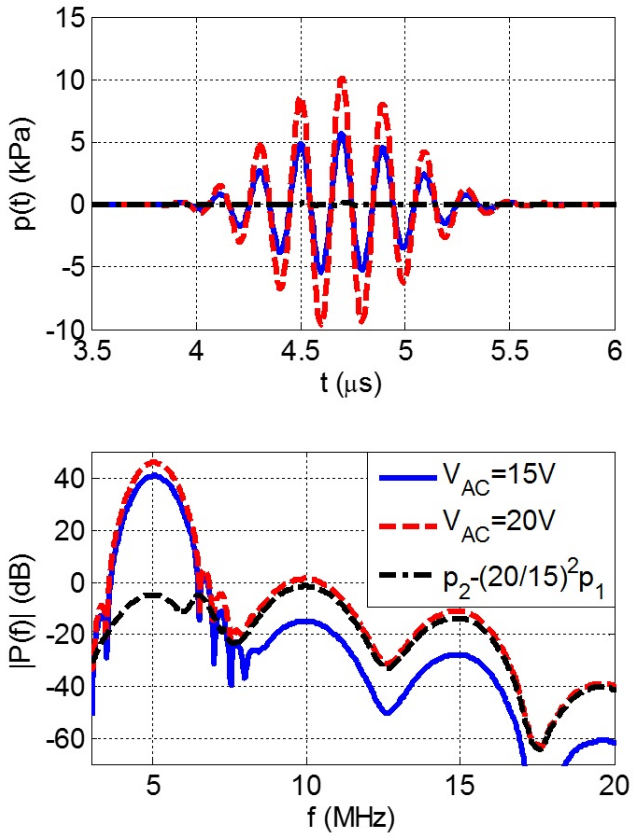

Figure 89: Two consecutive pressure outputs for two pulses with scaled amplitudes and their sum in time and frequency domains

suppress the nonlinearities associated with nonlinear wave propagation in the tissue directly applicable to CMUTs. For contrast agent imaging, a specific harmonic is suppressed by transmitting two consecutive pulses with a corresponding inter-pulse phase difference, and the two received waveforms are added. For example, two pulses with $\pi/2$ phase difference supresses the even order harmonics. This approach eliminates the desired harmonic content generated by both the nonlinear CMUT dynamics and nonlinear wave propagation within the tissue, leaving solely the nonlinear contrast agent response, potentially improving the contrast-to-tissue ratio in the constructed image. However this approach is only applicable to the cases where the desired harmonic can be extracted by filtering the sum signal, which requires narrow-band signals. For broadband signals, or for elimination of

all contribution from the CMUT and the nonlinear propagation in the tissue, an alternative phase modulation method is presented where N phase modulated signals are transmitted to eliminate all the harmonics except the N^{th} and its own harmonics. For example by transmitting 4 pulses, the first three harmonics can be cancelled out. The method has been validated for both small and large displacement regimes via simulations and experiments. The proposed method is also evaluated in the dynamic collapse-snapback operation regime with satisfactory results. Additionally it has been shown that a gap feedback linearized CMUT can be utilized for tissue harmonic imaging by two phase or amplitude modulated pulses with subharmonic excitation at the half the desired operation frequency.

CHAPTER 6

CONTRIBUTIONS AND FUTURE RESEARCH

This research aims to achieve two main goals. First objective is to develop computationally efficient, accurate modeling and design tools for capacitive micromachined ultrasonic transducers (CMUTs). Such tools would enable CMUT researches to study not well understood CMUT dynamics in terms of nonlinearities and acoustic crosstalk in array operation. Moreover, using such tools the CMUT designer can design, simulate, iteratively optimize CMUT array designs rapidly and proceed to fabrication with confidence. The second goal is to investigate and understand the nonlinear CMUT behavior and develop methods to compensate for the handicaps related to these nonlinearities. With such methods CMUTs can be effectively utilized in diagnostic imaging and therapy modalities such as harmonic imaging and HIFU where their performance is not optimal because of the nonlinear nature of these transducers. The two goals of this thesis essentially complementary since to develop an accurate CMUT model the nonlinearities must be investigated and well understood. On the other hand, the capability to model the nonlinear CMUT behavior is essential to study the nonlinear characteristics of CMUTs. The work presented in this thesis is published in [107–109].

6.1 Contributions of this research

1. A detailed analysis of the CMUT nonlinearity is performed using a first order model and it is concluded that the gap dependence of electrostatic forces is the main nonlinearity source for a CMUT rather than voltage square dependence.

2. It has been shown that the dependence of the electrostatic force distribution on displacement is another source of CMUT nonlinearity for large displacements that are required for increased transmit power. A method to accurately predict this additional nonlinearity is developed based on modal analysis of CMUT membranes. It has been

proven that nonlinear dynamics of a CMUT membrane can be captured accurately with two lumped parameters via comparison to finite element simulations.

3. Developed a nonlinear feedback linearization method for CMUTs cancelling the dominant gap dependent nonlinearities, improving the performance of CMUTs for harmonic imaging and high intensity focused ultrasound where transducer linearity is important. Furthermore, subharmonic excitation at the half of the desired frequency is introduced for the gap feedback linearized CMUT, resulting in theoretically complete suppression of harmonic distortion.

4. Developed a dual gap feedback topology that improves the gap feedback linearization performance of membrane based CMUTs utilizing dual-electrode structure

5. A MATLAB based lumped CMUT array model is developed. The experimentally verified model is capable of predicting the large-signal response of CMUT arrays with arbitrary membrane and array geometries. The model also incorporates the electrical terminations in calculations and shows FEA accuracy. By utilizing high performance computing, realistic arrays with sizes that are not feasible to simulate with FEA are simulated and experimentally verified crosstalk analysis is conducted.

6. Developed a method based on FEA to calculate the stiffness matrices of membranes with arbitrary geometries to be included in boundary element method.

7. Extended the boundary element method applied to CMUTs to receive operation and pulse-echo operation with minimal computational burden via analytical modification of Green's function via method of images

8. Proved that nonlinear CMUT behavior obeys power series relationship

9. Developed a multi-pulse phase modulation method for utilization of CMUTs in contrast agent imaging without any restriction on the membrane displacement. It has

been shown that the method also works when CMUT is driven for maximized pressure output in collapse-snapback mode. The method also optimizes the contrast agent-to-tissue ratio in the image.

10. Developed a two-pulse phase modulation method for tissue harmonic imaging with the subharmonically excited gap feedback linearized CMUT.

6.2 Future Research

1. By utilizing the developed CMUT array model, the input signals that are required for a desired pressure output can be calculated rapidly via simulation of ideal gap feedback. The feedback distorted input signal can be fed to CMUT in an open loop fashion to achieve the desired transmit behavior. The sensitivity of the calculated pre-distorted input signal to fabrication uncertainties will be investigated via simulations and experimental investigation of the gap feedback based input shaping will be conducted.

2. By interfacing the developed model with an electronics simulator such as SPICE, more complex driver and receiver electronics can be included for a complete system model. In addition, the presented model can form the core of a virtual design tool for CMUT based imaging systems when coupled with commercial software tools like COMSOL and SPICE as well as image simulators like FIELD II. An extensive graphical user interface for the developed model will also be developed for its use by the CMUT researchers.

3. As the proof of principle simulations and experiments demonstrate the potential of the proposed nonlinear imaging methods, imaging experiments would further validate the approach. Nonlinear tissue harmonic and contrast agent imaging experiments utilizing a CMUT array and the presented phase modulation methods will be conducted as future work.

4. The relationship of power series coefficients governing the large signal CMUT behavior to frequency, dc and ac signal amplitudes will be investigated for further understanding of CMUT nonlinearity.

REFERENCES

[1] K. K. Shung, M. Smith, and B. M. Tsui, *Principles of medical imaging*. Academic Press, 1992.

[2] T. Szabo, *Diagnostic Ultrasound Imaging: Inside Out*. Elsevier Academic Press, 2004.

[3] B. J. Kimura, V. Bhargava, and A. N. DeMaria, "Value and limitations of intravascular ultrasound imaging in characterizing coronary atherosclerotic plaque," *American heart journal*, vol. 130, no. 2, pp. 386–396, 1995.

[4] B. Potkin, A. Bartorelli, J. Gessert, R. Neville, Y. Almagor, W. Roberts, and M. Leon, "Coronary artery imaging with intravascular high-frequency ultrasound.," *Circulation*, vol. 81, no. 5, pp. 1575–1585, 1990.

[5] F. Tranquart, N. Grenier, V. Eder, and L. Pourcelot, "Clinical use of ultrasound tissue harmonic imaging," *Ultrasound in medicine & biology*, vol. 25, no. 6, pp. 889–894, 1999.

[6] T. S. Desser and R. B. Jeffrey, "Tissue harmonic imaging techniques: physical principles and clinical applications," in *Seminars in Ultrasound, CT and MRI*, vol. 22, pp. 1–10, Elsevier, 2001.

[7] E. Quaia, "Microbubble ultrasound contrast agents: an update," *European radiology*, vol. 17, no. 8, pp. 1995–2008, 2007.

[8] M. J. Blomley, J. C. Cooke, E. C. Unger, M. J. Monaghan, and D. O. Cosgrove, "Science, medicine, and the future: Microbubble contrast agents: a new era in ultrasound," *BMJ: British Medical Journal*, vol. 322, no. 7296, p. 1222, 2001.

[9] F. Forsberg, W. Shi, and B. Goldberg, "Subharmonic imaging of contrast agents," *Ultrasonics*, vol. 38, no. 1, pp. 93–98, 2000.

[10] M. Pasovic, M. Danilouchkine, T. Faez, P. L. Van Neer, C. Cachard, A. F. van der Steen, O. Basset, and N. de Jong, "Second harmonic inversion for ultrasound contrast harmonic imaging," *Physics in medicine and biology*, vol. 56, no. 11, p. 3163, 2011.

[11] J. W. Hunt, M. Arditi, and F. S. Foster, "Ultrasound transducers for pulse-echo medical imaging," *Biomedical Engineering, IEEE Transactions on*, no. 8, pp. 453–481, 1983.

[12] J. A. Brown, C. E. Démoré, and G. R. Lockwood, "Design and fabrication of annular arrays for high-frequency ultrasound," *Ultrasonics, Ferroelectrics and Frequency Control, IEEE Transactions on*, vol. 51, no. 8, pp. 1010–1017, 2004.

[13] E. D. Light, V. Lieu, and S. W. Smith, "New fabrication techniques for ring-array transducers for real-time 3d intravascular ultrasound," *Ultrasonic imaging*, vol. 31, no. 4, pp. 247–256, 2009.

[14] F. L. Degertekin, R. O. Guldiken, and M. Karaman, "Annular-ring cmut arrays for forward-looking ivus: transducer characterization and imaging," *Ultrasonics, Ferroelectrics and Frequency Control, IEEE Transactions on*, vol. 53, no. 2, pp. 474–482, 2006.

[15] S. Carlier, A. Sisman, and M. Karaman, "2f-2 annular cmut arrays for side looking intravascular ultrasound imaging," in *Ultrasonics Symposium, 2007. IEEE*, pp. 84–87, IEEE, 2007.

[16] D. M. Mills and L. S. Smith, "Real-time in-vivo imaging with capacitive micromachined ultrasound transducer (cmut) linear arrays," in *Ultrasonics, 2003 IEEE Symposium on*, vol. 1, pp. 568–571, IEEE, 2003.

[17] L. Kinsler, *Fundamentals of acoustics*. Wiley, 2000.

[18] G. Kino, *Acoustic waves: devices, imaging, and analog signal processing*. Prentice Hall PTR, 1987.

[19] B. Haider and R. Y. Chiao, "Higher order nonlinear ultrasonic imaging," in *Ultrasonics Symposium, 1999. Proceedings. 1999 IEEE*, vol. 2, pp. 1527–1531, IEEE, 1999.

[20] C.-C. Shen and P.-C. Li, "Pulse-inversion-based fundamental imaging for contrast detection," *Ultrasonics, Ferroelectrics and Frequency Control, IEEE Transactions on*, vol. 50, no. 9, pp. 1124–1133, 2003.

[21] R. J. Eckersley, C. T. Chin, and P. N. Burns, "Optimising phase and amplitude modulation schemes for imaging microbubble contrast agents at low acoustic power," *Ultrasound in medicine & biology*, vol. 31, no. 2, pp. 213–219, 2005.

[22] K. Spencer, J. Bednarz, P. Rafter, C. Korcarz, and R. Lang, "Use of harmonic imaging without echocardiographic contrast to improve two-dimensional image quality," *The American journal of cardiology*, vol. 82, no. 6, pp. 794–799, 1998.

[23] D. H. Simpson, C. Chien Ting, and P. N. Burns, "Pulse inversion doppler: a new method for detecting nonlinear echoes from microbubble contrast agents," *Ultrasonics, Ferroelectrics and Frequency Control, IEEE Transactions on*, vol. 46, no. 2, pp. 372–382, 1999.

[24] C. S. Chapman and J. C. Lazenby, "Ultrasound imaging system employing phase inversion subtraction to enhance the image," May 27 1997. US Patent 5,632,277.

[25] G. A. Brock-Fisher, M. D. Poland, and P. G. Rafter, "Means for increasing sensitivity in non-linear ultrasound imaging systems," Nov. 26 1996. US Patent 5,577,505.

[26] P. Phillips, "Contrast pulse sequences (cps): imaging nonlinear microbubbles," in *Ultrasonics Symposium, 2001 IEEE*, vol. 2, pp. 1739–1745, IEEE, 2001.

[27] P. J. Frinking, A. Bouakaz, J. Kirkhorn, F. J. Ten Cate, and N. De Jong, "Ultrasound contrast imaging: current and new potential methods," *Ultrasound in medicine & biology*, vol. 26, no. 6, pp. 965–975, 2000.

[28] K. Morgan, M. Averkiou, and K. Ferrara, "The effect of the phase of transmission on contrast agent echoes," *Ultrasonics, Ferroelectrics and Frequency Control, IEEE Transactions on*, vol. 45, no. 4, pp. 872–875, 1998.

[29] N. de Jong, P. J. Frinking, A. Bouakaz, and F. J. Ten Cate, "Detection procedures of ultrasound contrast agents," *Ultrasonics*, vol. 38, no. 1, pp. 87–92, 2000.

[30] P. Shankar, P. D. Krishna, and V. Newhouse, "Advantages of subharmonic over second harmonic backscatter for contrast-to-tissue echo enhancement," *Ultrasound in medicine & biology*, vol. 24, no. 3, pp. 395–399, 1998.

[31] F. Hunt, *Electroacoustics: the analysis of transduction, and its historical background*. Harvard University Press, 1954.

[32] D. T. Yeh, O. Oralkan, I. O. Wygant, M. O'Donnell, and B. T. Khuri-Yakub, "3-d ultrasound imaging using a forward-looking cmut ring array for intravascular/intracardiac applications," *Ultrasonics, Ferroelectrics and Frequency Control, IEEE Transactions on*, vol. 53, no. 6, pp. 1202–1211, 2006.

[33] M. I. Haller and B. T. Khuri-Yakub, "A surface micromachined electrostatic ultrasonic air transducer," *Ultrasonics, Ferroelectrics and Frequency Control, IEEE Transactions on*, vol. 43, no. 1, pp. 1–6, 1996.

[34] H. Yongli, A. S. Ergun, E. Haeggstrom, M. H. Badi, and B. T. Khuri-Yakub, "Fabricating capacitive micromachined ultrasonic transducers with wafer-bonding technology," *Microelectromechanical Systems, Journal of*, vol. 12, no. 2, pp. 128–137, 2003.

[35] A. M. Cetin and B. Bayram, "Diamond-based capacitive micromachined ultrasonic transducers in immersion," *Ultrasonics, Ferroelectrics and Frequency Control, IEEE Transactions on*, vol. 60, no. 2, pp. 414–420, 2013.

[36] S. Machida, "Mems technology using back-end of line processes in cmos lsi," in *Interconnect Technology Conference (IITC), 2010 International*, pp. 1–3.

[37] J. Zahorian, M. Hochman, T. Xu, S. Satir, G. Gurun, M. Karaman, and F. L. Degertekin, "Monolithic cmut-on-cmos integration for intravascular ultrasound applications," *Ultrasonics, Ferroelectrics and Frequency Control, IEEE Transactions on*, vol. 58, no. 12, pp. 2659–2667, 2011.

[38] D. M. Mills and L. S. Smith, "Real-time in-vivo imaging with capacitive micromachined ultrasound transducer (cmut) linear arrays," in *Ultrasonics, 2003 IEEE Symposium on*, vol. 1, pp. 568–571 Vol.1.

[39] I. Ladabaum, J. Xuecheng, H. T. Soh, A. Atalar, and B. t. Khuri-Yakub, "Surface micromachined capacitive ultrasonic transducers," *Ultrasonics, Ferroelectrics and Frequency Control, IEEE Transactions on*, vol. 45, no. 3, pp. 678–690, 1998.

[40] S. Zhou, P. Reynolds, and J. Hossack, "Precompensated excitation waveforms to suppress harmonic generation in mems electrostatic transducers," *Ultrasonics, Ferroelectrics and Frequency Control, IEEE Transactions on*, vol. 51, no. 11, pp. 1564–1574, 2004.

[41] J. D. Fraser, "Bias charge regulator for capacitive micromachined ultrasonic transducers," Dec. 11 2001. US Patent 6,328,696.

[42] A. Novell, M. Legros, N. Felix, and A. Bouakaz, "Exploitation of capacitive micromachined transducers for nonlinear ultrasound imaging," *Ultrasonics, Ferroelectrics and Frequency Control, IEEE Transactions on*, vol. 56, no. 12, pp. 2733–2743, 2009.

[43] S. Menigot, D. Certon, D. Gross, and J.-M. Girault, "Automatic optimal input command for linearization of cmut output by a temporal target," *Ultrasonics, Ferroelectrics, and Frequency Control, IEEE Transactions on*, vol. 61, pp. 1742–1753, Oct 2014.

[44] M. Legros, A. Novell, A. Bouakaz, G. Ferin, R. Dufait, and D. Certon, "Tissue harmonic imaging with cmuts," in *Proc. IEEE International Ultrasonics Symposium*, pp. 2249–2252, 2011.

[45] A. Novell, J.-M. Escoffre, and A. Bouakaz, "Second harmonic and subharmonic for non-linear wideband contrast imaging using a capacitive micromachined ultrasonic transducer array," *Ultrasound in medicine & biology*, vol. 39, no. 8, pp. 1500–1512, 2013.

[46] K. Chen, *A Column-Row-Parallel ASIC architecture for 3D wearable/portable medical ultrasonic imaging*. PhD thesis, Massachusetts Institute of Technology, 2014.

[47] A. Novell, M. Legros, J.-M. Grégoire, P. A. Dayton, and A. Bouakaz, "Evaluation of bias voltage modulation sequence for nonlinear contrast agent imaging using a capacitive micromachined ultrasonic transducer array," *Physics in medicine and biology*, vol. 59, no. 17, p. 4879, 2014.

[48] T. G. Fisher, T. J. Hall, S. Panda, M. S. Richards, P. E. Barbone, J. Jiang, J. Resnick, and S. Barnes, "Volumetric elasticity imaging with a 2-d cmut array," *Ultrasound in medicine & biology*, vol. 36, no. 6, pp. 978–990, 2010.

[49] D. N. Stephens, M. ODonnell, K. Thomenius, A. Dentinger, D. Wildes, P. Chen, K. K. Shung, J. Cannata, P. Khuri-Yakub, O. Oralkan, *et al.*, "Experimental studies with a 9f forward-looking intracardiac imaging and ablation catheter," *Journal of Ultrasound in Medicine*, vol. 28, no. 2, pp. 207–215, 2009.

[50] A. S. Savoia, G. Caliano, and M. Pappalardo, "A cmut probe for medical ultrasonography: from microfabrication to system integration," *Ultrasonics, Ferroelectrics and Frequency Control, IEEE Transactions on*, vol. 59, no. 6, pp. 1127–1138, 2012.

[51] D. Certon, N. Senegond, D. Gross, M. Legros, A. Boulmé, B. Roman, F. Teston, and G. Férin, "Dual mode cmuts fabricated with lpcvd sacrificial release process," in *Ultrasonics Symposium (IUS), 2011 IEEE International*, pp. 604–607, IEEE, 2011.

[52] C. Daft, S. Calmes, D. da Graca, K. Patel, P. Wagner, and I. Ladabaum, "Microfabricated ultrasonic transducers monolithically integrated with high voltage electronics," in *Ultrasonics Symposium, 2004 IEEE*, vol. 1, pp. 493–496, IEEE, 2004.

[53] A. Nikoozadeh and P. T. Khuri-Yakub, "Cmut with substrate-embedded springs for non-flexural plate movement," in *Ultrasonics Symposium (IUS), 2010 IEEE*, pp. 1510–1513.

[54] Hitachi-Medical-Corp., *Hitachi Mappie CMUT Ultrasound Probe*. Available : http://www.hitachi-medical.co.jp/tech/medix/pdf/vol51/P31-34.pdf, 2009.

[55] B. C. Lee, A. Nikoozadeh, K.-K. Park, and B. Khuri-Yakub, "Understanding cmuts with substrate-embedded springs," in *Ultrasonics Symposium (IUS), 2011 IEEE International*, pp. 1008–1011, IEEE, 2011.

[56] G. Gurun, M. Hochman, P. Hasler, and F. L. Degertekin, "Thermal-mechanical-noise-based cmut characterization and sensing," *Ultrasonics, Ferroelectrics and Frequency Control, IEEE Transactions on*, vol. 59, no. 6, pp. 1267–1275, 2012.

[57] A. Lohfink and P. C. Eccardt, "Linear and nonlinear equivalent circuit modeling of cmuts," *Ultrasonics, Ferroelectrics and Frequency Control, IEEE Transactions on*, vol. 52, no. 12, pp. 2163–2172, 2005.

[58] H. Kagan Oguz, S. Olcum, M. N. Senlik, V. Tas, A. Atalar, and H. Koymen, "Nonlinear modeling of an immersed transmitting capacitive micromachined ultrasonic transducer for harmonic balance analysis," *Ultrasonics, Ferroelectrics and Frequency Control, IEEE Transactions on*, vol. 57, no. 2, pp. 438–447, 2010.

[59] W. Mason, *Electromechanical transducers and wave filters*. D. Van Nostrand Co., 1948.

[60] S. Senturia, *Microsystem Design*. Springer, 2000.

[61] N. A. Hall, R. O. Guldiken, J. McLean, and F. L. Degertekin, "Modeling and design of cmuts using higher order vibration modes [capacitive micromachined ultrasonic transducers]," in *Ultrasonics Symposium, 2004 IEEE*, vol. 1, pp. 260–263 Vol.1.

[62] I. O. Wygant, M. Kupnik, and B. T. Khuri-Yakub, "Analytically calculating membrane displacement and the equivalent circuit model of a circular cmut cell," in *Ultrasonics Symposium, 2008. IUS 2008. IEEE*, pp. 2111–2114.

[63] H. Koymen, A. Atalar, E. Aydogdu, C. Kocabas, H. K. Oguz, S. Olcum, A. Ozgurluk, and A. Unlugedik, "An improved lumped element nonlinear circuit model for a circular cmut cell," *Ultrasonics, Ferroelectrics and Frequency Control, IEEE Transactions on*, vol. 59, no. 8, pp. 1791–1799, 2012.

[64] A. Lohfink, P. C. Eccardt, W. Benecke, and H. Meixner, "Derivation of a 1d cmut model from fem results for linear and nonlinear equivalent circuit simulation," in *Ultrasonics, 2003 IEEE Symposium on*, vol. 1, pp. 465–468 Vol.1.

[65] A. Bozkurt, "A lumped-circuit model for the radiation impedance of a circular piston in a rigid baffle," *Ultrasonics, Ferroelectrics and Frequency Control, IEEE Transactions on*, vol. 55, no. 9, pp. 2046–2052, 2008.

[66] R. O. Guldiken, J. Zahorian, F. Yamaner, and F. Degertekin, "Dual-electrode cmut with non-uniform membranes for high electromechanical coupling coefficient and high bandwidth operation," *Ultrasonics, Ferroelectrics and Frequency Control, IEEE Transactions on*, vol. 56, no. 6, pp. 1270–1276, 2009.

[67] M. N. Senlik, S. Olcum, and A. Atalar, "Improved performance of cmut with nonuniform membranes," in *Ultrasonics Symposium, 2005 IEEE*, vol. 1, pp. 597–600.

[68] G. G. Yaralioglu, S. A. Ergun, and B. T. Khuri-Yakub, "Finite-element analysis of capacitive micromachined ultrasonic transducers," *Ultrasonics, Ferroelectrics and Frequency Control, IEEE Transactions on*, vol. 52, no. 12, pp. 2185–2198, 2005.

[69] B. Bayram, G. G. Yaralioglu, A. S. Ergun, M. Oralkan, and B. T. Khuri-Yakub, "Dynamic fem analysis of multiple cmut cells in immersion [capacitive micromachined ultrasonic transducers]," in *Ultrasonics Symposium, 2004 IEEE*, vol. 1, pp. 252–255 Vol.1.

[70] C. Meynier, F. Teston, and D. Certon, "A multiscale model for array of capacitive micromachined ultrasonic transducers," *The Journal of the Acoustical Society of America*, vol. 128, no. 5, pp. 2549–2561, 2010.

[71] S. Timoshenko, *THEORY OF PLATES AND SHELLS 2E*. 1959.

[72] F. Fahy and P. Gardonio, *Sound and Structural Vibration: Radiation, Transmission and Response*. Elsevier Science, 2007.

[73] N. Senegond, F. Teston, F. Patat, and D. Certon, "Non-linear dynamic response of cmuts population: modeling and characterization," in *Ultrasonics Symposium (IUS), 2009 IEEE International*, pp. 426–429.

[74] A. Lohfink and P. C. Eccardt, "Investigation of nonlinear cmut behavior," in *Ultrasonics Symposium, 2005 IEEE*, vol. 1, pp. 585–588.

[75] A. Bozkurt, I. Ladabaum, A. Atalar, and B. T. Khuri-Yakub, "Theory and analysis of electrode size optimization for capacitive microfabricated ultrasonic transducers," *Ultrasonics, Ferroelectrics and Frequency Control, IEEE Transactions on*, vol. 46, no. 6, pp. 1364–1374, 1999.

[76] R. O. Guldiken, J. McLean, and F. L. Degertekin, "CMUTS with dual electrode structure for improved transmit and receive performance," *Ultrasonics, Ferroelectrics and Frequency Control, IEEE Transactions on*, vol. 53, no. 2, pp. 483–491, 2006.

[77] R. Guldiken, J. Zahorian, M. Balantekin, F. L. Degertekin, C. Tekes, A. Sisman, and M. Karaman, "5g-5 dual-annular-ring cmut array for forwardlooking ivus imaging," in *Ultrasonics Symposium, 2006. IEEE*, pp. 698–701.

[78] J. Zahorian, M. Hochman, S. Satir, and F. L. Degertekin, "Bias optimization of dual ring cmut arrays for forward looking ivus applications," in *Ultrasonics Symposium (IUS), 2010 IEEE*, pp. 447–450.

[79] R. O. Guldiken, M. Balantekin, J. Zahorian, and F. Degertekin, "Characterization of dual-electrode cmuts: demonstration of improved receive performance and pulse echo operation with dynamic membrane shaping," *Ultrasonics, Ferroelectrics and Frequency Control, IEEE Transactions on*, vol. 55, no. 10, pp. 2336–2344, 2008.

[80] H. Yongli, E. O. Haeggstrom, Z. Xuefeng, A. S. Ergun, and B. T. Khuri-Yakub, "Optimized membrane configuration improves cmut performance," in *Ultrasonics Symposium, 2004 IEEE*, vol. 1, pp. 505–508 Vol.1.

[81] J. G. Knight and F. L. Degertekin, "Capacitive micromachined ultrasonic transducers for forward looking intravascular imaging arrays," in *Ultrasonics Symposium, 2002. Proceedings. 2002 IEEE*, vol. 2, pp. 1079–1082 vol.2.

[82] H. Yongli, Z. Xuefeng, E. Hggstrom, A. Ergun, C. Ching-Hsiang, and B. Khuri-Yakub, "Capacitive micromachined ultrasonic transducers with piston-shaped membranes: fabrication and experimental characterization," *Ultrasonics, Ferroelectrics and Frequency Control, IEEE Transactions on*, vol. 56, no. 1, pp. 136–145, 2009.

[83] B. Bayram, O. Oralkan, A. S. Ergun, E. Haeggstrom, G. G. Yaralioglu, and B. T. Khuri-Yakub, "Capacitive micromachined ultrasonic transducer design for high power transmission," *Ultrasonics, Ferroelectrics and Frequency Control, IEEE Transactions on*, vol. 52, no. 2, pp. 326–339, 2005.

[84] H. Yongli, E. Haeggstrom, B. Bayram, Z. Xuefeng, A. S. Ergun, C. Ching-Hsiang, and B. T. Khuri-Yakub, "Comparison of conventional and collapsed region operation of capacitive micromachined ultrasonic transducers," *Ultrasonics, Ferroelectrics and Frequency Control, IEEE Transactions on*, vol. 53, no. 10, pp. 1918–1933, 2006.

[85] S. Olcum, F. Y. Yamaner, A. Bozkurt, and A. Atalar, "Deep-collapse operation of capacitive micromachined ultrasonic transducers," *Ultrasonics, Ferroelectrics and Frequency Control, IEEE Transactions on*, vol. 58, no. 11, pp. 2475–2483, 2011.

[86] F. Y. Yamaner, S. Olcum, H. K. Oguz, A. Bozkurt, H. Koymen, and A. Atalar, "High-power cmuts: design and experimental verification," *Ultrasonics, Ferroelectrics and Frequency Control, IEEE Transactions on*, vol. 59, no. 6, pp. 1276–1284, 2012.

[87] P. B. Chu and K. S. J. Pister, "Analysis of closed-loop control of parallel-plate electrostatic microgrippers," in *Robotics and Automation, 1994. Proceedings., 1994 IEEE International Conference on*, pp. 820–825 vol.1.

[88] J. I. Seeger and B. E. Boser, "Charge control of parallel-plate, electrostatic actuators and the tip-in instability," *Microelectromechanical Systems, Journal of*, vol. 12, no. 5, pp. 656–671, 2003.

[89] J. I. Seeger and S. B. Crary, "Stabilization of electrostatically actuated mechanical devices," in *Solid State Sensors and Actuators, 1997. TRANSDUCERS '97 Chicago., 1997 International Conference on*, vol. 2, pp. 1133–1136 vol.2.

[90] J. M. Kyynarainen, A. S. Oja, and H. Seppa, "Increasing the dynamic range of a micromechanical moving-plate capacitor," *Analog Integr. Circuits Signal Process.*, vol. 29, no. 1-2, pp. 61–70, 2001.

[91] E. S. Hung and S. D. Senturia, "Extending the travel range of analog-tuned electrostatic actuators," *Microelectromechanical Systems, Journal of*, vol. 8, no. 4, pp. 497–505, 1999.

[92] J. Reddy, *An Introduction to the Finite Element Method*. McGraw-Hill Education, 2005.

[93] M. Hochman, "Investigation of acoustic crosstalk effects in cmut arrays," Master's thesis, Georgia Institute of Technology, 2011.

[94] J. Zahorian and F. L. Degertekin, "Modeling and characterization of thin film coatings for high frequency cmut annular arrays," in *Ultrasonics Symposium (IUS), 2011 IEEE International*, pp. 596–599.

[95] J. Ginsberg, *Mechanical and Structural Vibrations: Theory and Applications*. Wiley, 2001.

[96] R. N. Bracewell and R. Bracewell, *The Fourier transform and its applications*, vol. 31999. McGraw-Hill New York, 1986.

[97] A. Oppenheim, R. Schafer, and J. Buck, *Discrete-time signal processing*. Prentice Hall, 1999.

[98] The MathWorks Inc., Simulating dynamic systems [Online] Available:http://www.mathworks.com/help/simulink/ug/simulating-dynamic-systems.html#f7-19688.

[99] A. D. Pierce *et al.*, *Acoustics: an introduction to its physical principles and applications*. McGraw-Hill New York, 1981.

[100] J. Knight, J. McLean, and F. L. Degertekin, "Low temperature fabrication of immersion capacitive micromachined ultrasonic transducers on silicon and dielectric substrates," *Ultrasonics, Ferroelectrics and Frequency Control, IEEE Transactions on*, vol. 51, no. 10, pp. 1324–1333, 2004.

[101] P. He, "Acoustic parameter estimation based on attenuation and dispersion measurements," in *Engineering in Medicine and Biology Society, 1998. Proceedings of the 20th Annual International Conference of the IEEE*, vol. 2, pp. 775–778, IEEE, 1998.

[102] S. Olcum, M. N. Senlik, and A. Atalar, "Optimization of the gain-bandwidth product of capacitive micromachined ultrasonic transducers," *Ultrasonics, Ferroelectrics and Frequency Control, IEEE Transactions on*, vol. 52, no. 12, pp. 2211–2219, 2005.

[103] E. L. Carstensen, "Self-reciprocity calibration of electroacoustic transducers," *The Journal of the Acoustical Society of America*, vol. 19, no. 6, pp. 961–965, 1947.

[104] R. Courant, K. Friedrichs, and H. Lewy, "On the partial difference equations of mathematical physics," *IBM journal of Research and Development*, vol. 11, no. 2, pp. 215–234, 1967.

[105] G. Gurun, C. Tekes, J. Zahorian, T. Xu, S. Satir, M. Karaman, J. Hasler, and F. L. Degertekin, "Single-chip cmut-on-cmos front-end system for real-time volumetric ivus and ice imaging.," *IEEE transactions on ultrasonics, ferroelectrics, and frequency control*, vol. 61, no. 2, pp. 239–250, 2014.

[106] I. Ladabaum, P. Wagner, C. Zanelli, J. Mould, P. Reynolds, and G. Wojcik, "Silicon substrate ringing in microfabricated ultrasonic transducers," in *Ultrasonics Symposium, 2000 IEEE*, vol. 1, pp. 943–946, IEEE, 2000.

[107] S. Satir and F. Degertekin, "Harmonic reduction in capacitive micromachined ultrasonic transducers by gap feedback linearization," *Ultrasonics, Ferroelectrics and Frequency Control, IEEE Transactions on*, vol. 59, no. 1, pp. 50–59, 2012.

[108] S. Satir, J. Zahorian, and F. L. Degertekin, "A large signal model for cmut arrays with arbitrary membrane geometries operating in non-collapsed mode," *IEEE transactions on ultrasonics, ferroelectrics, and frequency control*, vol. 60, no. 11, p. 2426, 2013.

[109] S. Satir and F. L. Degertekin, "A computationally efficient nonlinear system model for cmut arrays," in *Ultrasonics Symposium (IUS), 2014 IEEE International*, pp. 313–316, IEEE, 2014.